BRIDGING THE GAP BETWEEN QUANTUM MECHANICS AND EXPERIMENTS WITH ATOMISTIC MATERIALS SIMULATIONS USING MACHINE LEARNING

A Dissertation
Presented to
The Academic Faculty

By

James E. Chapman Jr

In Partial Fulfillment
of the Requirements for the Degree
Doctor of Philosophy in the
School of Materials Science and Engineering

Georgia Institute of Technology

August 2020

BRIDGING THE GAP BETWEEN QUANTUM MECHANICS AND EXPERIMENTS WITH ATOMISTIC MATERIALS SIMULATIONS USING MACHINE LEARNING

Approved by:

Dr. Rampi Ramprasad, Advisor
School of Materials Science and Engineering
Georgia Institute of Technology

Dr. Seung Soon Jang
School of Materials Science and Engineering
Georgia Institute of Technology

Dr. Chaitanya Deo
School of Materials Science and Engineering
Georgia Institute of Technology

Dr. Andrew Medford
School of Chemical and Biomolecular Engineering
Georgia Institute of Technology

Dr. Le Song
School of Computational Science and Engineering
Georgia Institute of Technology

Date Approved: June 2, 2020

If I have seen further, it is by standing on the shoulders of giants

Sir Issac Newton

To my wife Heather, and my parents

Acknowledgments

To my parents. You instilled a level of discipline in me that I will always be grateful for. Without your intelligence and humor to bounce off of, I don't know if I would have made it this far.

To my wife Heather. Your unconditional support throughout the last 5 years is something words cannot describe. Through the ups and downs, the good times and bad times, and the sometimes thousands of miles apart, we've made it. I know this hasn't been easy, but we've made it through, and now it's time to start a new chapter in our lives.

To my undergraduate advisors. Without your guidance, I most certainly would not have finished a PhD. You helped mold me from a naive young kid, into a blossoming scientist, and for that I will forever be grateful.

To my graduate advisor, Dr. Ramprasad. I am thankful for your guidance in helping me become the researcher I am today. I have learned so much from you, not only about research, but also about life. You taught me that research is an endeavor that must be planned from beginning to end before you start. While the end result may change during the course of one's research, without a plan you will be lost. I will also forever be indebted to you for not giving up on me, for without your patience and support I would not be where I am today.

To my committee members, Dr. Seung Soon Jang, Dr. Chaitanya Deo, Dr. Andrew Medford, and Dr. Le Song. Thank you for your guidance, as each of your expertise and feedback has helped shape this work into what it is today.

To my previous group members, Venkatesh Botu, Arun Kumar Mannodi Kanakkithodi, and Rohit Batra. I am grateful for the numerous conversations over the years, and the guidance you have all given me, be it professional or personal.

To my current group members. Grad school is a marathon, and without all of the conversations we've had, who knows where we would all be.

To the National Science Foundation, Office of Naval Research, Department of Energy, and Department of Defense for funding the work presented in this thesis, as well as computational support from XSEDE, and PACE.

TABLE OF CONTENTS

LIST OF TABLES

LIST OF FIGURES

SUMMARY

As the exploration of materials trends further towards the atomic scale, understanding the dynamic processes that occur at such domains becomes increasingly important. These processes include the nucleation of voids, the coarsening of grains, as well as the growth and melting of surfaces and particles. As these processes are all governed by individual atomic-level interactions, any strategy that aims to probe these regimes, be it experimental or computational, must be capable of accurately capturing the evolution of atomic-level processes. Over the past century, computational techniques have been instrumental in the study of materials at these time and length scales, and have been widely used to explain a multitude of atomistic processes. However, even with the successes of modern computational methods, they are hindered by either the computational cost associated with a particular method (quantum mechanics), limiting the time and lengths scales that can be studied, or by a given model's accuracy (semi-empirical), restricting the types of phenomena that can be simulated.

In this thesis, data-driven (machine learning (ML)) methods are utilized to bridge the gap between these two limitations, by combining the accuracy of quantum mechanics with the efficiency of semi-empirical methods. In this thesis, ML models for potential energy, atomic forces, and the total stress tensor are independently constructed for each materials system using generated density functional theory data as their reference. Atomic/nano-scale phenomena, for three elemental systems (Al, Pt, and Li), such as the diffusion of defects on surfaces and within bulk environments, the temperature dependence of lattice, mechanical, the growth of surfaces and grains in large-scale systems containing hundreds-of-thousands of atoms, and the structural properties of liquids and complex defect environments are predicted, using atomistic simulations, to show the breadth of the capabilities of the ML models in bridging the gap between the quantum world and the observable one. The work presented in this thesis highlights the ability of machine learning methods to

accurately simulate both small and large-scale phenomena, connecting simulations with experiments, at the accuracy of quantum mechanics.

CHAPTER 1
INTRODUCTION

1.1 From atoms to materials

Since the dawn of civilization, or perhaps even before, mankind has observed the universe and asked the question "Why?". This question obviously takes on many forms: *Why does the sun rise and set? Why do some objects float on water, and other sink? Why do offspring grow to look like their parents?* Over the last several thousand years, we as a species have found answers to questions that our forefathers could only have dreamed of understanding. But as we've learned over time, the universe does not offer its secrets willingly. Every fact, every observation, every new piece of knowledge that has ever been added to humanity's wealth of information has come by meticulously building upon previous knowledge, regardless of its complexity, or simplicity. To quote Sir Issac Newton's popularized latin expression, "If I have seen further it is by standing on the shoulders of giants". The work presented in this thesis is no exception, with the discoveries and creations of hundreds of scientists and engineers serving as the foundation to my work. While the work presented in this thesis aims to answer questions about the study of materials at the atomic level, perhaps this work will seem no more fundamental to a scientist a thousands years from now, as the question about the sun rising seems to me today.

For many millennia, humanity has used materials in every aspect of life: tools to grow and harvest food, weapons to defend or conquer, and engines to travel within, and outside of, our planet. However, with ever-increasing complexity in the challenges we face, comes the need for more complex materials to solve those challenges [1, 2, 3, 4, 5, 6]. Therefore, one can often no longer rely on simply observing macroscopic behavior to solve these problems, but is required to probe increasingly smaller time and length scales to construct

better materials [7, 8, 9, 10, 11, 12, 13, 14, 15].

As the investigation of materials trends further towards the atomic scale, understanding how these materials change over time at these domains becomes crucial. Many dynamic processes such as the nucleation of voids, coarsening of grains, growth and/or melting of surfaces, and the transformation from one to phase to another, are all governed by individual atoms interacting with one-another [16, 17, 18]. However, accurately capturing the intricate nature of these interactions is often a daunting challenge, owing to the complexity of the interactions themselves, as well as the time and length scales required to observe them [19]. Therefore, any strategy that aims to probe the atomic regime, be it experimental or computational, must be capable of accurately capturing the evolution of individual atomic processes. But a further question remains: how does one connect these atomic-level processes with the observations of macro-scale phenomena, as there is often a disparity of many orders of magnitude in both time and size between the macro and micro world [20, 21, 22].

To illustrate this connection I will discuss how individual atomic-level adatom diffusion profiles can be used to understand how surfaces grow. One can imagine that a single adatom, on an arbitrary surface of a material, can take many paths to diffuse between some point A and another point B [23]. The number of pathways the adatom can take will not only depend on the physical structure of the surface (is it a clean surface, or are there other defects present), but also conditions such as the temperature of the system, external pressure, presence of external field, etc. Even if one can discover a subset of all the unique physical paths the adatom can take, the question of how likely is each to occur arises. Now one must know both the physical pathway as well as the kinetics of the reaction. But how does temperature and disorder affect each profile? Even if one could probe the surface experimentally and observe such length-scales, capturing the various diffusion processes in action is nearly impossible due to the time-scales in which they occur [24, 25, 26, 27, 28]. However, if one could observe each mechanism in real-time, a picture would form where

one could predict exactly where atoms will travel, eventually resulting in the growth of the surface. Therefore, one needs tools to probe these domains, and connect what transpires there with what we observe as the end result.

1.2 Role of computational methods

Over the past century, computational methodologies have become instrumental in studying materials at these time and length scales, and have been widely used to explain a multitude of atomistic processes [29, 30, 31, 32, 33]. Historically, the vast majority of computational studies have employed quantum mechanics (QM), via direct and indirect methods [34, 35, 36, 37]. Such tools are generally referred to as *ab initio* or first principles methods. While QM by itself is too cumbersome to study materials directly, advances in the mid 1960s brought QM to the forefront of computational studies through a theory called density functional theory (DFT) [38, 39]. At its heart, DFT transforms the many-electron Schrodinger equation to the single-electron Kohn-Sham equation. Such a transformation provided the community with a practical capability to reliably calculate the energy of a configuration of atoms. Even then, it would take until the mid 1990s for DFT to become a common, and accepted, tool in the physical science and engineering communities [40, 41, 42, 43, 44]. Today, DFT has proven to be one of the most useful tools for the study of atomistic phenomena, owing to its unparalleled accuracy and transferability to practically any chemical system.

However, while reliably predicting the energy of a configuration of atoms is an important piece of the puzzle, it is not enough to connect the atomic world with the observable one. To this end, two computational frameworks, independent of DFT, had to be introduced. These paradigms can be qualitatively described as: (1) the ability to minimize the energy of a configuration of atoms to discover a lowest-energy structure [45, 46, 47, 48, 49, 50, 51, 52], and (2) the ability to study the dynamic evolution of materials by allowing them to exchange properties such as energy, temperature, and pressure with an external system

[53, 54, 55, 56, 57, 58]. Finally, to connect the output of these frameworks, one must also rely on statistical mechanics to map the microscopic world with the macroscopic one [59, 60, 61]. The combination of these mathematical frameworks with DFT provides access to observable properties such as temperature, pressure, energy, elastic constants, mechanical properties, heat capacity, etc [62, 63]. It is this combination that has allowed scientists and engineers to probe the atomic world in search of answers to fundamental questions about materials.

However, while the success of this combination cannot be understated, it suffers from a serious drawback [64, 65, 66]. QM methods, while able to provide access to properties at an extremely high level of fidelity, are computationally cumbersome, and severely restrict both the time and length scales that can be studied. For instance, the explicit dynamical evolution of a single point defect in a bulk elemental metal, with timescales larger than a few picoseconds, and length scales beyond a few angstrom, is still a daunting task for QM methods. More complex phenomena such as grain coarsening, melting, and surface growth are simply not possible to study. Therefore, QM methods, such as DFT, cannot be practically utilized to explain important portions of the atomistic world..

In an attempt to fill the void left by QM/DFT, researchers have developed a plethora of clever schemes to accelerate/approximate behavior of materials at the atomic-level. These methods can be grouped into two broad classes: (1) methods that aim to reduce the cost of calculating the energy and forces on a configuration of atoms, and (2) methods that coarsen simulations, either by redefining time or by eliminating degrees of freedom in the system. The first class of methods include schemes such as cluster expansion [67, 68, 69, 70], tight-binding DFT [71, 72], classical/semi-empirical force fields [73, 74, 75, 76], reactive force fields [77], and the machine learning (ML) models constructed in this thesis. The second class of methodologies includes schemes such as Monte Carlo methods [78], meta-dynamics [79, 80, 81], accelerated molecular dynamics [82, 83], hyper-dynamics [84], and coarse-grained molecular dynamics [85, 86, 87].

However, even with these advances, the end result is still not satisfactory. While the first class has opened the door to the atomistic study of materials at length and time scales far beyond that of DFT, they have come at the cost of accuracy and transferability [88, 89]. Models are parameterized for specific problems, and generally fail when encountering enironments that they were not fit to. The second class has allowed for the study of even larger systems, over longer time-scales, such as the folding of proteins [90, 91, 92], but requires *a priori* knowledge about the critical features encountered during the evolution of a system; a task that is generally difficult or impossible [93]. Therefore, current atomistic simulations are still hindered by the many deficiencies of the methodologies discussed so far.

1.3 Machine learning as a bridge between computations and experiments

The challenges and deficiencies discussed in the previous section have prompted a new way of thinking, in which the immense amount of data being generated is used to augment and/or create models [94, 95]. Such methods have been employed by many fields over the last half-century to aid in a variety of aspects in our daily life such as recommendation and search engines [96, 97, 98], image recognition [99, 100, 101], and self-driving cars [102, 103, 104]. However, the use of data-driven methods within the physical science communities took until the mid 2000s to gain ground [105, 106]. The following decade saw the creation of a multitude of models, all aimed at exploring the capabilities of such models, and their usefulness at solving the community's list of long-standing problems [107, 108, 109].

Such methods have generally be employed to aid in one of two ways: (1) to comb through and discover hidden relationships and/or rules among the data, and (2) build predictive models by using the data to learn mappings between and input and an output. ML methods have indeed made significant progress within these two categories in the materials science community [105, 110, 111, 112, 113, 114]. Determination of phase diagrams

[115, 116], construction of force fields and potential energy surfaces [117, 118, 119], acceleration of structure search algorithms [120, 121], determination of hidden relationships between complex sets of data [122, 123, 124], are all examples of ML's success within this domain. Of particular importance to the work presented in this thesis is the progress made in the realm of force field/potential energy surface construction to aid in the study of the dynamic evolution of atomistic pheoneoma.

Many such ML schemes have been developed recently, as seen in Table 1.1. Neural Network Potentials[125, 126, 127] (NNP), High-Dimensional Neural Network Potentials [117, 128] (HDNNP), Cluster-based Neural Networks [129], the Atomic Energy Network (Aenet) [130], and Permutation Invariant Polynomial Neural Networks (PIP-NN) [131] have employed single layer, and deep neural networks to learn the underlying potential energy surfaces (PES), by passing a set of symmetry functions through the neural network and learning the atomic energies, and sometimes the atomic forces as well. Gaussian Approximation Potentials [119] (GAP), Spectral Neighborhood Analysis Potentials [132] (SNAP), Moment Tensor Potentials [133] (MTP), N-body Kernel Gaussian Processes [134], the Bag of Bonds [135] (BOB) approach, and a ML prescription proposed by Theil et al [136], all employ linear or non-linear regression methods to directly learn atomic energies for a structure of atoms, and sum these energies to predict the total potential energy.

Other ML methodologies were developed to learn the forces directly. The AGNI scheme [118, 137], along with the Machine Learning for Quantum Mechanical Properties [138] (MLQMP) methodology used a set of atom-centered symmetry functions, optimized through KRR, to predict the various force components individually. Vectorial Gaussian Processes [139] (VGP) employed a multivariate Gaussian distribution with a vector-valued mean function and matrix-valued kernel function, to learn the force vector directly. However, both methods suffered from energy conservation issues, again, due to error propagation when integrating the atomic forces to obtain the potential energy. In an attempt to solve this issue, Gradient Domain Machine Learning [140] (GDML) directly obtains a conser-

Table 1.1: Various ML scheme aimed at calculating atomistic properties such as potential energy or atomic forces.

ML Scheme	Property Learned
Neural Network Potentials	Potential Energy
High Dimensional Neural Network Potentials	Potential Energy
Cluster-based Neural Networks	Potential Energy
Permutation Invariant Polynomial Neural Networks	Potential Energy
Moment Tensor Potentials	Potential Energy
N-body Kernel Gaussian Processes	Potential Energy
Theil et al prescription	Potential Energy
Gaussian Approximation Potentials	Potential Energy
Spectral Neighborhood Analysis Potentials	Potential Energy
Bag Of Bonds	Potential Energy
Adaptive Generalizable Neighborhood Informed	Forces
Gradient Domain Machine Learning	Forces
Vectorial Gaussian Processes	Forces
Machine Learning Quantum Mechanical Properties	Forces

vative vector field estimate of the forces, ensuring that energy will be conserved; though other properties such as stresses are not guaranteed to avoid this issue.

In this thesis I demonstrate the capability of ML for the construction of models that learn properties such as the potential energy, atomic forces, and stress tensor, directly, to understand the dynamic evolution of processes such as crystal growth and grain coarsening. Using a set of local geometric descriptors, combined with a robust set of reference DFT data, ML models were created and validated over several proof-of-concept systems, including adatom diffusion on the several low-index aluminum surfaces, the migration of a single vacancy in bulk platinum, and the prediction of a multitude of grain boundary and surface energies in platinum. Long time and length scale simulations were used to study phenomena far outside the reach of DFT, such as growth of the Al (110) surface, the dynamic evolution of mechanical properties and the coarsening of grains in platinum, and the successful prediction of accurate crystal structures via the dynamic quenching of lithium.

Such a set of predicted phenomena at time and length scales far beyond those of QM methods, provides yet another layer of validation that the methods presented in this thesis are not only a viable theoretical tool, but can, and should, be used to push the boundaries of nano-scale materials research, and aid in bridging the gap between atomic-level phenomena and macroscopic observations.

1.4 Thesis outline

Below is an outline describing the subsequent chapters that compose this thesis.

In Chapter 2, I provide a detailed explanation of the theoretical frameworks used in this work: density functional theory, the AGNI machine learning platform, molecular dynamics, and finally structure optimization methods. While many of the methods discussed in this chapter are well documented within the literature, the work presented in this thesis may be viewed by researches spanning many fields, and therefore I have provided a detailed explanation of all methods used.

Chapter 3 contains a series of works on aluminum surfaces, spanning several time and length-scales. I demonstrate the use of ML models for the prediction of atomic forces and potential energy, for the calculation of minimum energy profiles of a multitude of defect diffusion mechanisms on the Al (111),(110), and (100) surfaces. I then predict the melting temperature of these surfaces, as well as that of several Al (111)-(100) Wulff clusters, ranging from 1nm to 10nm. Finally, I showcase the ML model's use in the epitaxial growth of the Al (110) surface, and match the resulting observations, qualitatively, with experiments.

Chapter 4 also contains a series of sections corresponding to the study of defect behavior of several time and length scales in platinum. Unlike chapter 3, ML models for atomic forces, potential energy, and the total stress tensor are employed. I start by discussing the construction of these models for the study of bulk phenomena. Using these models, I illustrate their capability in the prediction of bulk properties such as the vibrational density of states, elastic and mechanical properties, both at $T = 0$K and $T > 0$K. I then discuss how

the models can be iteratively improved to target new application domains. I display the improved model's accuracy in predicting thermodynamic properties, such as surface and grain boundary energies, adatom/dimer adsorption and binding energies, and the vacancy formation energy of a single vacancy within the grain boundary plane, for a multitude of surfaces and grain boundaries. I then demonstrate the ML model's use in predicting the kinetic profiles of adatom and vacancy diffusion on low-index surfaced and within/away-from grain boundary planes respectively. Lastly, the ML models are used to accurately predict the temperature threshold for grain growth, simulated via NPT molecular dynamics simulations.

In Chapter 5, I provide a case-study in which new ML algorithms must be employed to accurately capture the underlying physics of liquid lithium. A neural network force model is used to simulate the local atomic structure of liquid phases of lithium at pressures spanning several orders of magnitude. I demonstrate that the neural network model outperforms the kernel ridge regression model when it comes to accurately predicting the correct atomic neighbor distributions for several liquid phases. Kernel ridge regression models for the energy and stress tensor are also created, and used to simulate the quenching of liquid phases, at specific pressures, to predict the corresponding crystal phase. I finalize this chapter with a discussion regarding the move to neural network models for all predicted properties.

In Chapter 6, I provide a broad outlook on the promises and challenges of using ML for the prediction of atomistic properties, and their use in simulating atomic/nano-scale phenomena.

Lastly, an appendix containing the preliminary work for the prediction of energy, force, and stresses of several other material systems is included.

CHAPTER 2

METHODOLOGIES

2.1 Density functional theory

2.1.1 General overview

Quantum mechanics (QM) provides an exact description of the interaction of matter at the atomic level [141]. This prescription begins by postulating that the total energy of a system of atoms can be formulated as a wave equation, formally known as the Schrodinger equation. The Schrodinger equation takes on many forms, but for the purpose of the work presented in this thesis, a particular set of approximations are employed. The first approximation, generally used in the realm of materials science problems, is the Born-Oppenheimer approximation [142]. This approximation states that, as the nuclei of an atom move substantially slower than that of its electrons, then one can effectively treat the nuclei as fixed particles. This treatment allows the Schrodinger equation to effectively rely only on the motion of the electrons, even though a nuclear-electron interaction term will still be included.

In this work, how states evolve over time is not entirely relevant, and therefore, the second approximation is the use of the time-independent Schrodinger equation [143]. With these two approximations, the Schrodinger equation can be represented as:

$$\left[\frac{\hbar^2}{2m}\sum_{i=1}^{N}\nabla_i^2+\sum_{i=1}^{N}V(r_i)+\sum_{i=1}^{N}\sum_{j=1}U(r_i,r_j)\right]\Psi_e(r_1,...,r_N)=E_e\Psi_e(r_1,...,r_N) \tag{2.1}$$

The terms in the bracket, from left to right, denote the kinetic energy, nuclear-electron interaction energy, and electron-electron interaction energy. As the nuclei are not treated

explicitly, but rather approximately, one need only to solve the Schrodinger equation using the electron wavefunctions, denoted by Ψ_e. The solutions to the above eigenvalue problem, E_e, are the spectrum of electronic energy values, with the lowest energy value representing the ground state energy of the electrons. The total energy of the system can then be represented as:

$$E_{total} = E_e + E_{nuclei} \tag{2.2}$$

As E_{nuclei} is treated approximately through the Born-Oppenheimer approximation, it is E_e that must ultimately be solved to study atomic-level interactions. However, upon further inspection, one will find that computing E_e for any system containing more than a single electron is non-trivial, as Ψ_e is a function of 3N variables (x, y, and z positions of every electron in the system). Therefore, an alternative route must be taken to practically compute the total energy of a system of atoms.

Density functional theory (DFT) provides a framework that reformulates equation 2.1 as a single-electron problem, making computations of many-electron systems practical [38, 39]. A visual representation of this reformulation can be found in Figure 2.1. DFT relies on two fundamental theorems proposed by Hohenburg and Kohn [38]: (1) The ground state energy from the Schrodinger equation is a unique functional of the electron density, and (2) The electron density that minimizes the energy of this functional is the exact electron density that corresponds to the solution set of the Schrodinger equation. However, even with such knowledge, a practical method for solving this functional representation would have to wait until Kohn and Sham would propose the Kohn-Sham equation, providing a prescription in which the many-electron system, in the presence of fixed nuclei, could be mapped to a fictitious system containing non-interacting point particles in the presence of an effective external potential [39]. This formalism, referred to as the Kohn-Sham equation,

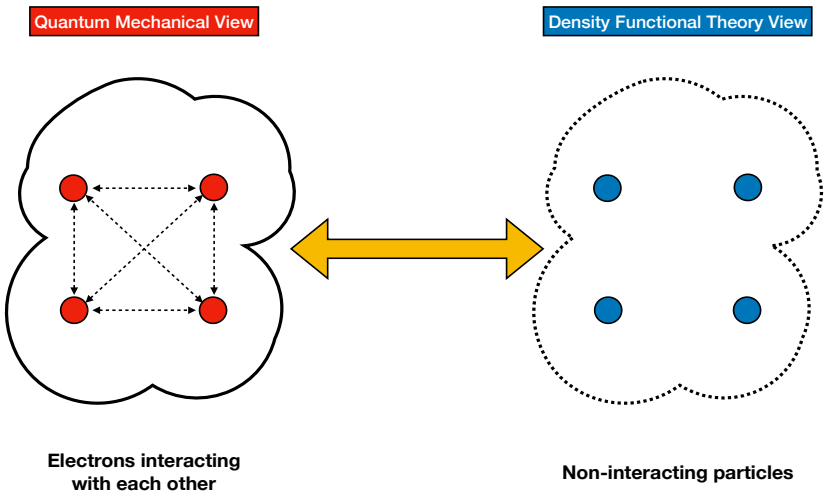

Figure 2.1: Generalized representation of how electrons are treated in quantum mechanics (left) and DFT (right). The yellow arrow represents the mapping DFT establishes between the two pictures, allowing for the ground state solution of the non-interacting systems to yield an exact solution to the interacting system.

is generally represented as:

$$\left[\frac{\hbar^2}{2m}\sum_{i=1}^{N}\nabla_i^2 + Vr + V_H(r) + V_{XC}(r)\right]\phi_i(r) = \varepsilon_i\phi_i(r) \tag{2.3}$$

Here the terms in the bracket, form left to right, represent the kinetic energy of an electron, the interaction potential of an electron surrounded by the corresponding nuclei, the interaction potential of an electron surrounded by the corresponding electrons, and the exchange-correlation potential. Equation 2.3 requires several approximations, as exact forms for $V_H(r)$ and $V_{XC}(r)$ are not universally known, and will be discussed in more detail in later sections. However, the reduction of a many-electron problem to a single-electron one is worth the substitution of known quantities for approximate ones. With the reduction in computational cost, properties such as elastic constants, vibrational frequencies, and equilibrium geometries can be calculated with unprecedented accuracy, as they rely only on the total energy [40, 41, 42, 43, 44].

For the purpose of this work, two other properties, aside from the total energy, are of critical importance: the atomic forces and the total stress tensor. Both the atomic forces, and the total stress tensor can be represented as the derivative of the total energy of the system, but with respect to the nuclei positions and spatial strain respectively [141].

$$F_i = -\frac{\partial E_{total}}{\partial R_i} \tag{2.4}$$

$$\sigma_{\alpha\beta} = \frac{1}{\Omega}\frac{\partial E_{total}}{\partial \varepsilon_{\alpha\beta}} \tag{2.5}$$

While this relationship provides a prescription for the calculation of forces and stresses, it is again, non-trivial, as an exact derivative of the total energy is not known. Finite-difference methods [144] can be used to provide access to both quantities, though such a process is often cumbersome. In the case of atomic forces, however, an alternative to finite-difference methods is available. The Hellmann-Feynman theorem [145] establishes a simple formalism that provides computationally cheap access to the atomic forces. The Hellmann-Feynman theorem is as follows:

$$F_i = -\frac{\partial \langle \Upsilon_i^* | H | \Upsilon_i \rangle}{\partial R_i} = -\langle \Upsilon_i^* | \frac{H}{R_i} | \Upsilon_i \rangle - E\frac{\partial \langle \Upsilon_i^* | \Upsilon_i \rangle}{\partial R_i} \tag{2.6}$$

Here H, Υ_i and R_i are the Hamiltonian, wavefunctions and positions of the nuclei respectively. As $E\frac{\partial \langle \Upsilon_i^* | \Upsilon_i \rangle}{\partial R_i} = 0$, since the wavefunctions are normalized to 1, the force acting on each atom is only dependent on the wavefunctions of the nuclei, and the nuclei Hamiltonian, which contains the electrostatic interaction between nuclei, and the interaction between the nuclei and electron charge density.

2.1.2 Plane-wave basis sets

The first question that should arise during the above prescription is, how does one actually determine the wavefunctions needed to calculate these atomic properties? While there are

many approaches one can take to answer this question, each with its own pros and cons, in this work a basis set of plane-wave functions are chosen to represent all wavefunctions [146]. This basis set takes on the general form of:

$$\psi_{i,k}(r) = \sum_{G}^{|G|<G_{max}} c_{ik,G} e^{i(k+G)r} \tag{2.7}$$

Where G represents discrete grid points within the space the basis set lives within, and $c_{ik,G}$ represents Fourier coefficients, as equation 2.7 represents a Fourier expansion of $\psi_{i,k}(r)$. The main advantages of using plane-wave basis sets over other approaches are [147]: (1) Can use extremely efficient Fast Fourier Transform (FFT) methods to quickly transform wavefunctions between real space and G-space representations, (2) $O(N^2)$ scaling allows for calculations to be made containing hundreds (or more) atoms, (3) Forces and stresses are simple to evaluate, as the derivatives of such functions are simple to derive analytically, and (4) such functions are not atom-centered, but rather live on user-defined grid points, in which the atom positions do not entirely dictate the wavefunction, as well as allowing the user to systematically control the accuracy of their wavefunction representation by controlling the density of the grid.

However, all good things have a down-side; by using plane-wave basis sets one must make three large sacrifices [147]: (1) Generally one needs to employ many hundreds (perhaps more) basis coefficients, which makes storing the Hamiltonian matrix practically impossible, (2) the vacuum regions are just as expensive to calculate as regions containing atoms, as the grid must be specified over the entire space, and not just where atoms exist, and (3) core electron regions become prohibitively expensive to calculate due to the nodal structure of the function within this region, thereby requiring pseudopotentials be employed to approximate the interaction between the electrons and an atom's nucleus.

2.1.3 PAW potentials

Projector augmented-wave (PAW) potentials [148, 149] are employed in this work to represent the interaction between the electrons and an atom's nucleus. The PAW method arises from the problem of wavefunction oscillations near the nucleus, which leads to the requirement of an extremely fine grid to accurately describe the wavefunctions in this region. The PAW method maps these oscillating wavefunctions to smooth functions in a new space. Such a mapping can be represented as:

$$|\Psi_n\rangle = |\widetilde{\Psi}_n\rangle + \sum_i (|\phi_i\rangle - |\widetilde{\phi}_i\rangle) \langle \widetilde{p}_i | \widetilde{\Psi_n}\rangle \tag{2.8}$$

Where Ψ_n is the true, all-electron (AE) wavefunction, and $\widetilde{\phi_i}$ is the corresponding wavefunction in the new space. n represents the index of a given wavfunction within the set containing all wavefunctions within a band. ϕ_i, and $\widetilde{p}_i$ represent the true partial wavefunction, and corresponding partial wavefunction in the new space, at atomic site i. The projector functions, p_i, must satisfy the the requirement of $\langle \widetilde{p}_i | \widetilde{\phi_{ij}} \rangle = \delta_j$. The total charge density is then broken into several components, represented as:

$$n(r) = \widetilde{n}(r) + n^1(r) - \widetilde{n}^1(r) \tag{2.9}$$

such that:

$$\widetilde{n}(r) = \sum_n f_n \langle \widetilde{\Psi}_n | r \rangle \langle r | \widetilde{\Psi}_n \rangle \tag{2.10}$$

$$n^1(r) = \sum_{i,j} \rho_{ij} \langle \phi_i | r \rangle \langle r | \phi_j \rangle \tag{2.11}$$

$$\widetilde{n}^1(r) = \sum_{i,j} \rho_{ij} \langle \widetilde{\phi}_i | r \rangle \langle r | \widetilde{\phi}_j \rangle \tag{2.12}$$

Here, ρ_{ij} are the occupancies of each augmentation channel (i, j), and are calculated using only the wavefunctions which live in the new space, $\rho_{ij} = \sum_n f_n \langle \widetilde{\Psi}_n | \widetilde{p}_i \rangle \langle \widetilde{p}_j | \widetilde{\Psi}_n \rangle$. The f_n coefficients represent the orbital occupation numbers. Upon closer inspection, one will note that n^1 contains the contribution of the true core states, and $\widetilde{n}^1$ and $\widetilde{n}$ contain the contribution of the mapped core states. Because of the way charge density is broken into separate contributions, the total energy must also be rewritten accordingly, and can be represented as:

$$E_{total} = \widetilde{E} + E^1 - \widetilde{E}^1 \tag{2.13}$$

As we are still within the Kohn-Sham framework, each energy term above will follow equation 2.3, with the appropriate substitutions for wavefunctions and charge density representations. The PAW method ultimately provides a scheme to capture the same information as the true wavefunctions outside of the core region, as well as obtain a reliable and computationally efficient wavefunction representation within the core region.

2.1.4 PBE exchange-correlation functional

Another important approximation made during a DFT calculation is the treatment of the exchange-correlation contribution to the total energy. Similarly to the treatment of electron-nucleus interaction, there are many available prescriptions for the exchange-correlation contribution. In this work, the Perdew-Burke-Ernzerhof (PBE) functional [150, 151] is employed for all DFT calculations. The PBE functional belongs to a class of functionals called generalized gradient apparoximation functionals, which take both the electron density and the density gradient into consideration when approximating the exchange-correlation contribution.

Another important distinction with the PBE method is its treatment of the charge density. Previously, the exchange-correlation contribution to the total energy was defined as $V_{XC}[n(r)]$, with $n(r)$ being the total charge density. However, this picture neglects any

contribution from the electron spin, and therefore will incorrectly capture the exchange-correlation effects. Therefore, PBE employs what is referred to as spin-density functional, represented as $V_{XC}[n_{up}(r), n_{down}(r)]$, in which the total charge density is defined as $n(r) = n_{up}(r) + n_{down}(r)$. The PBE exchange-correlation energy contribution is therefore calculated as:

$$E_{XC}^{PBE} = \int n(r)\varepsilon_{XC}^{PBE}(r_s(r), s(r), \zeta(r))dr \tag{2.14}$$

where $\zeta = \frac{n_{up} - n_{down}}{n}$, and represents the spin polarization term. r_s represents the Wigner-Seitz radius, which is defined as $r_s = (\frac{4}{3}\pi n)^{\frac{-1}{3}}$. $s(r)$ represents the gradient of the charge density and is expressed as $s(r) = \frac{|\nabla n(r)|}{2(3\pi^2)^{\frac{1}{3}} n(r)^{\frac{4}{3}}}$. The term, $\varepsilon_{XC}^{PBE}(r_s(r), s(r), \zeta(r))$ represents the PBE functional form.

2.2 Machine learning

2.2.1 General overview

While the QM framework described in the previous section is transferable and accurate to any material system, it suffers from a set of drawbacks discussed in detail throughout Chapter 1. Therefore, many methods have been developed over the last half-century in an attempt to solve these fundamental limitation of QM methods [64, 65, 66]. Attempts to approximate the mapping of structure to energy through empirical means [73, 74], or through physical approximations [75, 76], as well as methods that discover a portion of the underlying potential energy surface [152, 153, 154, 155, 156, 157] have proved successful in many regards. However, even these methodologies have severe limitations in terms of difficulty in construction of the models themselves, or in their lack of transferability to new configurations [88, 89].

ML methodologies have emerged over the last decade within the materials science, physics, and chemistry communities as a viable alternative to these classical/semi-empirical

methods for simulations involving large time ($> ns$) and length ($> nm$) scales [105, 110, 111, 112, 113, 114]. A detailed listing of all ML schemes used for these fields can be found in Chapter 1. These ML methodologies, however, all suffer a serious drawback; the models are generally fit to predict a single property, e,g,. potential energy, while properties such as forces, stresses, etc, are obtained either through numerical means, or via analytical derivatives of the ML algorithm. This poses a major problem, as errors in the model's primary output will be propagated down to any of the subsequently derived properties [140, 158, 159, 160, 161, 162, 163] (though some methods such as GDML impose constraints in an attempt to control error propagation).

An example of this can be seen in the prediction of forces from two ML methods: (1) GAP, and (2) AGNI, for the case of crystalline carbon [164, 165]. When employing GAP to predict the atomic forces on crystalline carbon, which are calculated as the derivative of the potential energy, an RMSE of 0.1 eV/$\mathring{A}$ is obtained. However, when using AGNI, which learns the forces directly, an RMSE of 0.08 eV/$\mathring{A}$ is achieved. Therefore, it is reasonable to assume that learning each property with its own ML model, rather than as a numerically derived quantity, can improve the performance of its predictions.

2.2.2 The AGNI machine learning platform

The AGNI platform, developed in this work, consists of several key steps: (1) The generation of a diverse set of reference data with certain target applications in mind, (2) Numerically encoding local/structural geometric information (fingerprinting), (3) Training a ML model given some subset of the reference data, (4) Employing the final ML models in an external MD engine, capable of simulating the dynamic, time-evolution of atomistic processes [166]. Figure 2.2 provides a visual representation of these steps. Steps 2-4 are discussed in detail in the following sections, while step 1 will be discussed at the beginning of each subsequent chapter, as the generation of reference data changes slightly depending on the problem being studied.

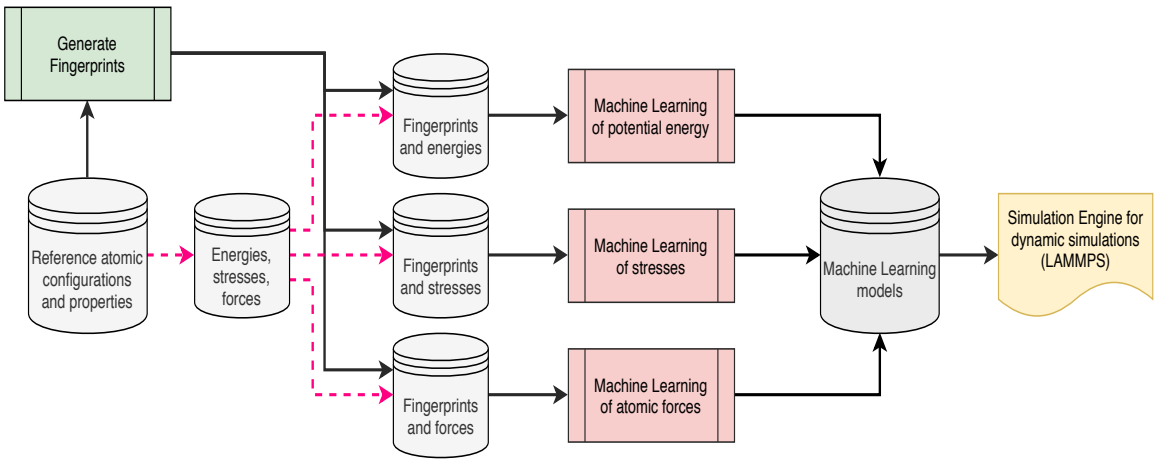

Figure 2.2: Generalized workflow for the AGNI machine learning platform. Black lines indicate the flow of fingerprints, while pink lines indicate the flow of raw DFT data.

2.2.3 From atoms to numerical features

Fingerprinting for Atomic Forces

The fingerprint used to learn the atomic forces can be broken into two schemes. The first method, denoted by $\mathbf{v}^1$, is an atom-centered approach, used to encode local structural information around an atom, within some cutoff, and map it directly to the force. Its functional form is given given by [118, 137, 167, 165]:

$$\mathbf{v}^1_{i,\alpha;k} = \sum_{j \neq i} \frac{r^\alpha_{ij}}{r_{ij}} exp\left(-\frac{r^2_{ij}}{\eta^2_k}\right) f_{cut}(r_{ij}) \tag{2.15}$$

Here, r_i and r_j are the Cartesian coordinates of atoms i and j, $r_{ij} = |\mathbf{r}_j - \mathbf{r}_i|$, r^α_{ij} is the projection of $\mathbf{r}_j$ - $\mathbf{r}_i$ onto any arbitrary direction α. The summation runs over the neighbor list set $\{j\}$ of atom i. The damping function $f_{cut}(r_{ij}) = \frac{1}{2}[cos(\frac{\pi r_{ij}}{R_{cut}}) + 1]$, which accounts for a smooth degradation in an atom's contribution to the atomic force exerted on atom i, has a cut-off radius R_{cut} chosen to be 8 Å. There is an adjustable parameter, $\{\eta_k\}$, which is obtained through a separate optimization process.

The second approach, denoted by $\mathbf{v}^2$, removes the atom-centered restriction, and places symmetry functions at various distances away from an atom. This approach allows one to

fine-tune which symmetry functions capture to most relevant information about an atom's local geometry. Its functional form is given given by [165, 168]:

$$\mathbf{v}^2_{i,\alpha;k} = \sum_{j \neq i} \frac{r^{\alpha}_{ij}}{r_{ij}} exp\left(-\frac{(r_{ij} - a_k)^2}{w^2}\right) f_{cut}(r_{ij}) \tag{2.16}$$

Here a_k represents the center of a specific symmetry function, at a distance a_k away from atom i, whose width is controlled by the tuning parameter w. All other variables in equation 2.16 are the same as in equation 2.15.

Fingerprinting for Potential Energy

In a similar fashion to the force fingerprints, a hierarchical representation of an atom's local structural environment is employed to encode local geometric information that maps directly to the total potential energy. This hierarchy aims to capture different aspects of the atomic neighborhood with features resembling scalar, vector, and tensor quantities defined by [169, 170, 166, 171]:

$$S_{i;k} = c_k \sum_{j \neq i} exp\left[-\frac{1}{2}\left(\frac{r_{ij}}{\sigma_k}\right)^2\right] f_{cut}(r_{ij}) \tag{2.17}$$

$$V_{i,\alpha;k} = c_k \sum_{j \neq i} \frac{r^{\alpha}_{ij}}{r_{ij}} exp\left[-\frac{1}{2}\left(\frac{r_{ij}}{\sigma_k}\right)^2\right] f_{cut}(r_{ij}) \tag{2.18}$$

$$T_{i,\{\alpha,\beta\};k} = c_k \sum_{j \neq i} \frac{r^{\alpha}_{ij} r^{\beta}_{ij}}{r^2_{ij}} exp\left[-\frac{1}{2}\left(\frac{r_{ij}}{\sigma_k}\right)^2\right] f_{cut}(r_{ij}) \tag{2.19}$$

Here, r_i and r_j are the Cartesian coordinates of atoms i and j, $r_{ij} = |\mathbf{r}_j$ - $\mathbf{r}_i|$. α and β represent any of the three x, y, or z directions. The damping function $f_{cut}(r_{ij}) = \frac{1}{2}[cos(\frac{\pi r_{ij}}{R_{cut}}) + 1]$, which accounts for a smooth degradation towards zero, has a cut-off radius R_{cut} chosen to be 8 Å. c_k is a normalization constant given by $\left(\frac{1}{\sigma_k\sqrt{2\pi}}\right)^3$. The pre-factors $\frac{r^{\alpha}_{ij}}{r_{ij}}$ and $\frac{r^{\alpha}_{ij} r^{\beta}_{ij}}{r^2_{ij}}$, which create unique vector and tensor components respectively, help to capture

angular information about the local atomic environment by computing all possible dipoles between atomic neighbors, and their interactions in different directions. However, this processes renders these two components directionally-dependent, in contrast to the scalar quantity. Therefore, we must employ rotationally-invariant forms of these quantities in order to map them to a rotationally-invariant property such as potential energy. The invariant form of the vector component is defined as:

$$\mathbf{V}_{i,k} = \sqrt{(V_{i,x;k})^2 + (V_{i,y;k})^2 + (V_{i,z;k})^2} \tag{2.20}$$

and the invariant forms of the tensorial component are:

$$\begin{aligned} \mathbf{T}'_{i,k} = T_{i,\{x,x\},k}T_{i,\{y,y\},k} + T_{i,\{x,x\},k}T_{i,\{z,z\},k} + T_{i,\{y,y\},k}T_{i,\{z,z\},k} \\ - \left(T_{i,\{x,y\},k}\right)^2 - \left(T_{i,\{x,z\},k}\right)^2 - \left(T_{i,\{y,z\},k}\right)^2 \end{aligned} \tag{2.21}$$

and

$$\mathbf{T}''_{i,k} = det\left(T_{i,\{\alpha,\beta\},k}\right) \tag{2.22}$$

Since our objective is to map the locally-derived fingerprint components directly to the global potential energy, rather than atomic energies as explored in previous works, we must map our local fingerprints to a single structural fingerprint defined by:

$$G_k = \left\{ M^n\left(\sum_{i=1}^{N} S_{i,k}\right), M^n\left(\sum_{i=1}^{N} \mathbf{V}_{i,k}\right), M^n\left(\sum_{i=1}^{N} \mathbf{T}_{i,k}\right) \right\} \tag{2.23}$$

Here the function $M^n(X)$ represents the n^{th} moment of the rotationally invariant fingerprint components. For this work only the first ($n = 1$) moment is considered, and can be interpreted as the average atomic environment of the system. It should also be noted that our final fingerprint G_k is indeed rotationally invariant, as all constituent components are

rotationally invariant, and therefore is suitable for learning the total potential energy.

Fingerprinting for the Stress Tensor

If one considers the functional form of the tensorial atomic fingerprints, $T_{i,\{\alpha,\beta\};k}$, it becomes apparent that each individual (α,β) pair can map directly to each component of the stress tensor. The functional form used is identical to that used in equation 4, however, the atomic fingerprints are not mapped to an invariant form, as the stress tensor is not rotationally invariant. The final mapping between the atomic fingerprints and the stress tensor is defined as [166]:

$$M^n \begin{pmatrix} T_{\{x,x\};k} & T_{\{x,y\};k} & T_{\{x,z\};k} \\ T_{\{y,x\};k} & T_{\{y,y\};k} & T_{\{y,z\};k} \\ T_{\{z,x\};k} & T_{\{z,y\};k} & T_{\{z,z\};k} \end{pmatrix} \mapsto \begin{pmatrix} \sigma_{xx} & \sigma_{xy} & \sigma_{xz} \\ \sigma_{yx} & \sigma_{yy} & \sigma_{yz} \\ \sigma_{zx} & \sigma_{zy} & \sigma_{zz} \end{pmatrix} \tag{2.24}$$

Here the first moment of the atomic fingerprint tensor is taken, resulting in a single fingerprint tensor for each structure. Similar to the energy scheme, the first moment of the atomic stress tensor is equivalent to taking the average value of each atomic tensorial fingerprint. Finally, every component of the averaged fingerprint tensor is mapped directly to the corresponding component of the stress tensor.

2.2.4 Sampling a Diverse Training Set

A plethora of unique sampling methods have been developed that attempt to create a diverse subset from the given reference information. Recently, several machine learning force fields have employed a technique referred to as grid sampling to develop models capable of accurately handling numerous distinct atomic environments [167, 172, 165, 166]. In this work, we have chosen to adopt this methodology as well. Grid sampling can be broken into 3 stages: (1) projecting the reference data onto a new two-dimensional (2D) space whose basis is composed of the two largest-variance principal components (determined via

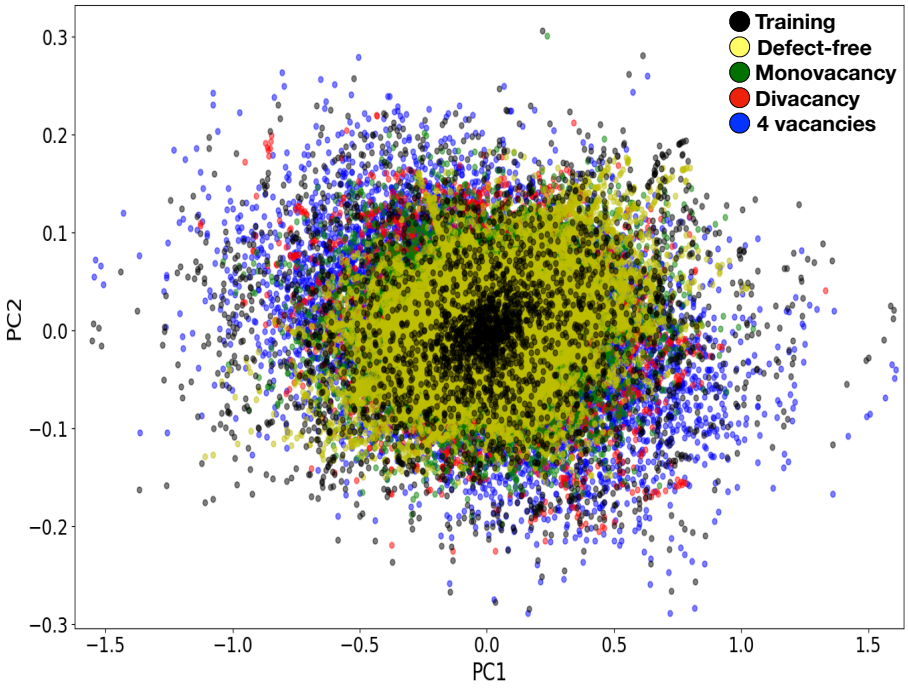

Figure 2.3: Principle component analysis decomposition for the case of the ML-force model. Colors indicate the type of defect present in the atomic configuration. The training points of the final ML-force model are shown in black. A visual inspection clearly shows that the training set spans the entire configuration space.

a principal component analysis [173] (PCA)), (2) defining a 2D grid that spans the subset of this space where the reference data lies, and (3) performing a uniformly-distributed random selection within the cells of this 2D manifold. As previous work has shown, PCA can be used to distinguish unique atomic environments, and hence, by performing this sampling scheme, one can intuitively expect that it will capture the diversity of the reference data. Figure 2.3 shows the clustering of reference data in the PCA space (when using the 2 most dominant PCA components) for the case of the ML-force model. The model's training points (shown in black), can be seen to span the entire training set, allowing for all environments to be robustly represented.

2.2.5 Kernel ridge regression

After the final fingerprint forms have been chosen, and a subset of our reference data has been selected, Kernel Ridge Regression [174] (KRR) can be used to create three indepen-

dent ML models for atomic forces, potential energy, and the stress tensor. This learning scheme employs a similarity-based non-linear kernel to establish a mapping between the reference fingerprints and the desired property using a functional form defined by [118, 137, 167, 172, 165, 166]:

$$P_X = \sum_Y \alpha_Y \exp\left[-\frac{1}{2}\left(\frac{d_{XY}}{\sigma}\right)^2\right] \tag{2.25}$$

Here the summation runs over the number of reference environments, with Y being each fingerprint within a given model's training set. P represents the desired property (total potential energy, stress tensor components, or atomic forces), where X is the fingerprint of the new structure. d_{XY} represents the euclidean distance between fingerprints X and Y in the hyperspace they are defined on, specified by a length scale σ. During the model's training phase, the regression weights α_Y and the length scale σ are determined by optimizing a regularized objective function through a 5-fold cross validation process.

2.2.6 Neural networks

In this work, artificial neural networks [175] (NN) are also used to predict the atomic forces. The primary benefit of employing NN over KRR is the size of the model's training set. With KRR, there is a rough maximum of 5,000-10,000 training points, in which training set sizes greater than this range not only become extremely expensive to calculate, but become difficult to iteratively improve [174]. NN do not have either problem; the size of the model's training set plays no role in the time required to make a new prediction, and, increasing the amount of training data can be augmented by a change in the NN architecture. While there is no reason one could not use NN to create models for both the potential energy and stress tensor, such models are not considered in this work, with only the atomic force model detailed in Chapter 5 being predicted by NN.

There are two main controls one has when constructing/training a NN model [175]: (1) The NN architecture, and (2) the activation functions used at each neuron. The NN

architecture used in this work employs an input layer equal to the number of fingerprint components, two hidden layers with the number of neurons equal to the number of fingerprint components, and a single output that maps to a particular force component. The network also uses the *tanh* activation function, due to its symmetry about $x = 0$, making it ideal for mapping the fingerprint components to a given force component. When training the NN models, a minimum of 50% of a given set of reference data was used in the model's training set, reaching numbers that are practically impossible with KRR models. A minimum of 250 epochs were used to ensure convergence in the model's predictions. In all cases, the Adam optimization algorithm [176] was used to obtain the final NN model. The final mathematical form of the NN is expressed in matrix form as:

$$\vec{u}^{(1)}(i) = \vec{V}_i * \hat{w}^{(0,1)} \tag{2.26}$$

$$\vec{u}^{(n)}(i) = \vec{f}(\vec{u}^{(n-1)}(i)) * \hat{w}^{(n-1,n)} \ni n > 1 \tag{2.27}$$

Here, $\vec{u}^{(n)}$ represents a given set of neurons for a particular layer n, with $n = 1$ representing the input layer. $\vec{V}_i$ represents the fingerprint vector used for a particular atom i. $w^{(n-1,n)}$ is the weight matrix of size $(M_{n-1}$ x $M_n)$, where M_n is the number of neurons is a given layer n. As mentioned previously, $\vec{f} = \frac{e^x - e^{-x}}{e^x + e^{-x}}$. The final layer is also represented as $f_i = \sum_m^{M_{last}} u_m^{last}(i)$.

2.2.7 LAMMPS-AGNI pair style

Once the ML-AGNI platform has been designed to go from data to ML model, integration into a MD engine is still required to study the time-dependent, dynamic behavior of materials. The Large-scale Atomic/Molecular Massively Parallel Simulator (LAMMPS) package [177] was chosen as the MD engine due to its scalability to HPC systems and memory cost. Lammps is also designed to work with both periodic and non-periodic systems, and comes

with a plethora of physical and statistical tools to study atomic-level properties.

The general LAMMPS workflow, seen in Figure 2.4, is as follows, and explained in further detail throughout this section: (1) All ML models, which are stored as text files and contain all relevant information required to make a prediction, are read into LAMMPS on the MPI thread of rank 0, and all relevant parameters are distributed to any other threads, (2) Atomic fingerprinting is performed over all MPI threads, as LAMMPS stores the atoms, and their corresponding neighbor lists on each MPI rank, and is finally reduced on MPI rank 0 for the structural energy and stress fingerprints (3) Force predictions are performed on each MPI thread, (4) Energy and stress calculations are then performed on the MPI thread of rank 0, and (5) Forces, stresses, and energy are then distributed to the appropriate LAMMPS internal classes to perform other actions, such as verlet integration to obtain new ionic positions. Currently the LAMMPS interface can handle all fingerprint types discussed earlier, and supports KRR, Gaussian Process Regression (GPR), and Neural Network (NN) calculations for atomic forces, along with KRR, and GPR predictions of energy and stresses.

Step 1, which consists of reading the various ML model files into LAMMPS, requires no further explanation. Step 2 involves atomic fingerprinting for all property mappings. This fingerprinting step, which requires only a given atom and its corresponding neighbor list, is performed over all MPI threads. Each thread, which contains a subset of all atoms, with each atom's corresponding global neighbor list, will fingerprint all atoms assigned to that thread. This domain decomposition allows for the complex, and time-consuming atomic fingerprinting process to be broken up into subsets, and reduce computational time. However, the potential energy and stress tensor mappings require a single global fingerprint for a given structure, and therefore cannot be performed on each MPI thread. While the atomic fingerprints that serve as the foundation for each structural fingerprint are still calculated over all MPI threads, each structural fingerprint must then be constructed on a single MPI thread. MPI offers simple function calls for doing this, and the final structural

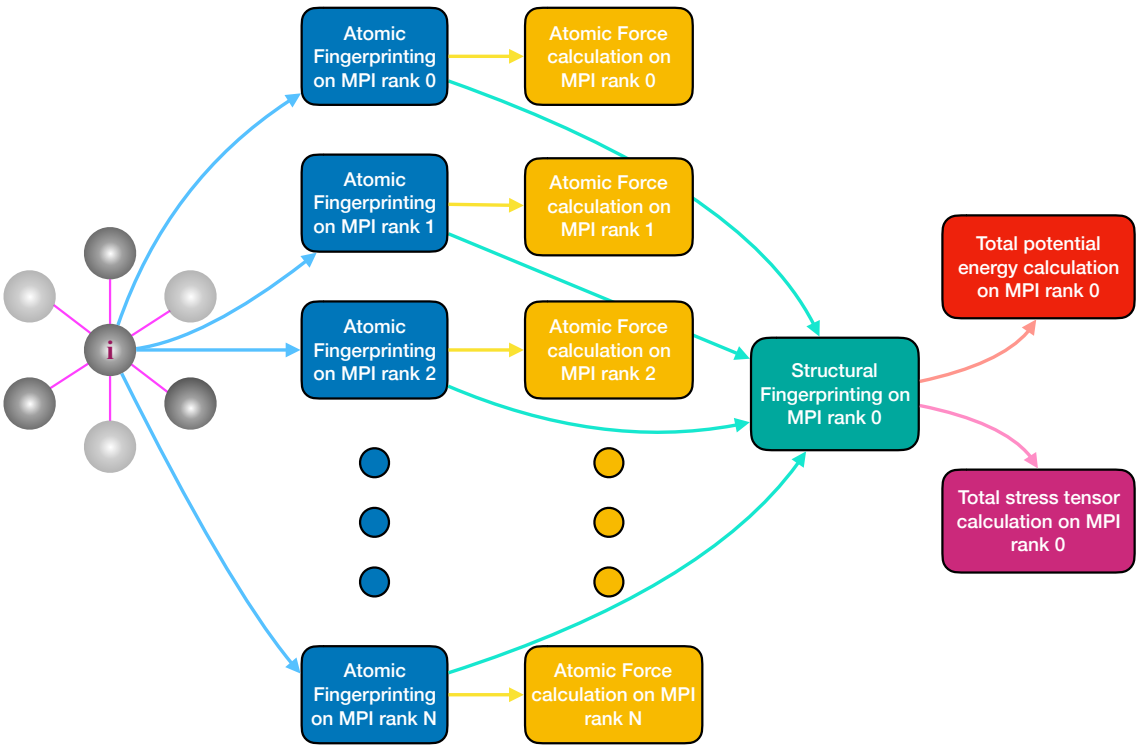

Figure 2.4: Schematic of the general workflow during a LAMMPS simulation, moving from a new atomic configuration, to the prediction of a particular property. Atomic fingerprinting and force predictions are done in parallel, whereas structural fingerprinting, as well as energy and stress tensor calculations are only performed on a single MPI rank. Arrows are colored based on the flow towards the next step in the process.

fingerprint is constructed on MPI rank 0.

Step 3 involves the ML prediction of the atomic forces. As each atom is assigned to a particular MPI rank, each force calculation is performed on that rank. Recall from step 2, each atom's atomic fingerprint will be calculated on the rank that the atom is assigned, as the atom's global neighbor list can be called from any MPI rank. Therefore, each force calculation can be performed using the atomic fingerprint generated on the atom's MPI rank. Step 4 involves the prediction of the total potential energy and total stress tensor. Again, as mentioned in step 2, these properties involve a single fingerprint being mapped to a single property value. As each fingerprint, which is a single, structural fingerprint, is stored on MPI rank 0, the prediction for the total potential energy and total stress tensor is performed on MPI rank 0 as well. Step 5, which involves passing the pair style information to other LAMMPS classes is performed outside of the pair style, by internal LAMMPS function calls, and requires no input/modification from the user. This process has been benchmarked for several bulk structures of elemental Pt, containing 4, 32, and 256 atoms, with the ML-AGNI models, several EAM potentials, and DFT. The ML-AGNI scheme is approximately 40 times slower than the EAM predictions, but roughly 5 orders-of-magnitude faster than DFT. Therefore, calculations on systems containing more than a million atoms, for simulation times greater than a nanosecond, are easily attainable with the ML-AGNI scheme, something far beyond the reaches of DFT.

2.3 Molecular dynamics

2.3.1 General overview

Molecular dynamics [53, 54, 55, 56, 57, 58] (MD) is a framework in which the time-dependent evolution of atomistic phenomena can be studied. At its most fundamental, MD is simply solving Newton's equations of motion (otherwise known as Newton's second

law), which is described by the following mathematical relation:

$$F_i = m_i a_i \tag{2.28}$$

Where F_i, m_i, and a_i are the force, mass, and acceleration respectively, of a particle i. A slightly more sophisticated way of expressing this equation is:

$$-\frac{dV}{dr_i} = m_i \frac{d^2 r_i}{dt^2} \tag{2.29}$$

Where V represents the potential energy of the system, and t represents time. If one were to integrate this equation twice, expressions for both the velocity and acceleration can be obtained. Therefore, to calculate the trajectory of a particle, one need only its position, initial velocity and acceleration. This implies that the equations of motion are deterministic, in that, the conditions at $t = k$ determines the conditions at $t = k + 1$. However, the acceleration and velocity is calculated as a function of the potential energy gradient, which is a function of $3N$ atomic coordinates, making an analytic derivative practically impossible to calculate. Therefore, the solutions to equation 2.29 must be found numerically.

While there are numerous methods for approximating these solutions, this work will focus on one of them, the velocity-verlet algorithm [178]. This algorithm calculates both the velocity and positions using the same value of time, and is represented as:

$$\vec{x}(t + \triangle t) = \vec{x}(t) + \vec{v}(t)\triangle t + \frac{1}{2}\vec{a}(t)\triangle t^2 \tag{2.30}$$

and

$$\vec{v}(t + \triangle t) = \vec{v}(t) + \frac{\vec{a}(t) + \vec{a}(t + \triangle t)}{2}\triangle t \tag{2.31}$$

It is important to note though, that in this algorithm $\vec{a}(t + \triangle t)$ depends only on $\vec{x}(t + \triangle t)$. Therefore, one can either calculate position first, and then velocity, or employ a

"half-timestep" scheme, in which the velocity is calculated first, as $\vec{v}(t+\frac{1}{2}\triangle t)$, using the previous timesteps' acceleration $a(t)$. $\vec{v}(t+\frac{1}{2}\triangle t)$ would then be used to solve for $\vec{x}(t+\triangle t)$, and so on. The velocity-verlet algorithm is used for all MD simulations performed in this work.

While the previous paragraphs discuss the theoretical framework in which particle trajectories are determined, there has been no mention of how these atomic-level properties are converted into macroscopic observables. While it may seem like the tools mentioned above are enough to extract this information, one must realize just how many atoms are present in a macroscopic material system. For example, 1 cm^3 of Al contains 10^{22} atoms, which is practically impossible to simulate due to the computational expense it would carry. Therefore, we must rely on mathematical laws that can connect the microscopic world with the macroscopic one.

The mathematical framework that allows us to connect these two domains is that of statistical mechanics [59, 60, 61] (SM). In SM, the evolution of microscopic systems can be thought of as a set of states, each one representing a point along the system's trajectory. These states are then averaged in an attempt to map directly to the observed behavior of the corresponding macroscopic system. This averaging is calculated as [58]:

$$\langle A \rangle_{ensemble} = \int \int A(r,p)P(r,p)drdp \tag{2.32}$$

Here r and p describe the phase space that the microstates exist within, and represent the positions and momentum of a configuration of atoms. $A(r,p)$ is the value of the property that is being sought after, while $P(r,p)$ represents the probability of such a property existing at a particular point in the phase space. While $A(r,p)$ is obviously dependent upon the property being calculated, $P(r,p)$ can be defined universally as [58]:

$$P(r,p) = \frac{1}{Z}\exp(-\frac{E(r,p)}{k_B T}) \tag{2.33}$$

with Z being defined as the microstate's partition function [58]:

$$Z = \int \int \exp(-\frac{E(r,p)}{k_B T}) dr dp \tag{2.34}$$

Where $E(r,p)$ is the total energy of the system at a given point in the phase space, T is the system's temperature, and k_B is the Boltzmann constant. The determination of Z is the primary bottleneck in extracting reliable information from microscopic trajectories. In theory, one must integrate Z over the entire phase space, which for most systems is exhaustively vast. Therefore, in practice, one would be required to perform MD simulations for near infinite time-scales, a feat the is practically impossible. Therefore, one must employ the Ergodic hypothesis to extract any useful information. This hypothesis states that an ensemble average is equivalent to a time average for a given property, and can be represented as [179]:

$$\langle A \rangle_{ensemble} = \langle A \rangle_{time} = \lim_{\tau \to \infty} \frac{1}{\tau} \int_0^{\tau} A(r(t), p(t)) dt \tag{2.35}$$

Therefore, rather than relying on the complete phase space, one can extract information, to a degree of accuracy specified by τ, as the time average of the phase space captured by the MD trajectory. It is important to note that, without such a mathematical representation, reliable information would be practically impossible to obtain from MD simulations due to the potential size of the phase space.

However, the framework discussed thus far pertains only to the microcanonical ensemble (NVE), as the mathematics here assume isolated systems, and offer no control over how properties such as temperature and pressure can affect a given microstate. That being said, even with these missing pieces, the same general issues regarding phase space exploration will remain, regardless of the ensemble framework chosen. While the framework mentioned above is not used in this work explicitly, it provides the reader with a foundation in which further modifications to it be can understood more easily. Such modifications are

discussed in the following sections.

2.3.2 Canonical ensemble (NVT)

The canonical ensemble [180] (NVT) differs from the NVE ensemble in that it represents all possible microstates of a system connected, in equilibrium, to an eternal thermal reservoir. The simulated system can exchange energy with the reservoir, allowing for the various system states to differ in total energy. Here, unlike NVE in which the total energy drives the probability distribution, temperature has the most influence over the probability distribution of the microstates. The NVT probability distribution is defined as [180]:

$$P = \frac{1}{Z}\exp(-\frac{F-E)}{k_B T}) \tag{2.36}$$

with the partition function, Z defined as:

$$Z = \int\int \exp(-\frac{F-E}{k_B T})drdp \tag{2.37}$$

Here, the introduction of the Helmholtz free energy F, which is a function of the number of particles N, the volume V, and the temperature T, to distinguish each microstate in the phase space. While F will remain constant throughout a trajectory, each trajectory's probability distribution will depend on the chosen set of (N,V,T).

However, one must employ a separate algorithm that can simulate the canonical ensemble, described above, during an MD simulation. In this work, the Nose-Hoover thermostat is used to approximate the canonical ensemble. The Nose-Hoover thermostat [181] redefines a state's Hamiltonian, $\mathscr{H}$, by introducing new degrees of freedom:

$$\mathscr{H} = \sum_i \frac{p_i^2}{2m_i s^2} + U(r) + \frac{p_s^2}{2Q} + gk_B T \ln s \tag{2.38}$$

Where $U(r)$ is the potential energy, defined as a function of coordinates r. s represents a new degree of freedom, introduced into the system due to its contact with the external

reservoir. p_s is defined as the conjugate momentum of s. p_i represents the "virtual" momentum, which is defined in terms of the real momentum as $p_i = p_i^{real} s$. Q is often referred to as the Nose mass, and serves as the "mass" for the motion of s, though it is not a real mass. g represents, roughly, the number of degrees of freedom the system contains, though in practice is chosen based on the canonical distribution at equilibrium. Finally, T is the user-defined temperature.

2.3.3 Isobaric-isothermal ensemble (NPT)

The isobaric-isothermal ensemble [182] (NPT) adds another layer of control over that of the canonical ensemble, in that the system of interest is in contact with not only a heat reservoir, but also a barostat. While the system and the heat bath still exchange energy, as in NVT, the system and the barostat also exchange volume. Therefore, at equilibrium, the total energy and volume will fluctuate about a converged value. The NPT probability distribution is defined as [182]:

$$P = \frac{1}{Z} \exp(-\frac{E + pV)}{k_B T}) \tag{2.39}$$

with the partition function, Z defined as [182]:

$$Z = \int \int \exp(-\frac{E + pV}{k_B T}) dr dp \tag{2.40}$$

Here the introduction of pV allows for each microstate to be distinguished by both the volume and the pressure of the system. As with F in the canonical ensemble, for a given volume, p remains fixed throughout a trajectory, while each trajectory's probability distribution will depend on a chosen set of (N, P, T).

Again, analogous to NVT, one must employ a separate algorithm that can actually simulate the isobaric-isothermal ensemble during an MD simulation. In this work, the Nose-Hoover thermostat is used to represent the thermal bath, while the Nose-Hoover barostat

[56] is chosen to act as the NPT barostat. The redefined, Nose-Hoover isobaric-isothermal Hamiltonian, $\mathscr{H}$, is defined as:

$$\mathscr{H} = \sum_i \frac{p_i^2}{2V^{\frac{2}{3}} m_i s^2} + U(V^{\frac{1}{3}} r) + \frac{p_s^2}{2Q} + g k_B T \ln s + \frac{p_V^2}{2W} + P_{ex} V \tag{2.41}$$

Here, the "virtual" variables are related to the real variables via a coordinate scaling factor of $V^{\frac{1}{3}}$; $q_i^{real} = V^{\frac{1}{3}} q_i$, and $p_i^{real} s = p_i V^{\frac{-1}{3}}$. p_V represents the conjugate momentum of V. W is analogous to Q in the Nose-Hoover thermostat, but here represents the "mass" for the volume change. Finally, P_{ex} is the user-defined external pressure.

2.4 Structure optimization

2.4.1 General overview

Structure optimization, also known as energy minimization, geometry optimization, etc, is a general mathematical framework that simulates the search for the structure corresponding to the global energy minimum along the system's potential energy surface [45, 46, 47, 48, 49, 50, 51, 52]. Many algorithms exist to aid in this search, but they all follow a general set of rules defined by [45]:

$$\frac{\partial E}{\partial \vec{r}} = \vec{0} \tag{2.42}$$

and

$$\left(\frac{\partial^2 E}{\partial r_i \partial r_j} \right)_{ij} = \mathbf{H}_{ij} = B^T M B > 0 \ni b > 0 \forall b \in B \tag{2.43}$$

Equation 2.42 states that the forces acting on all atoms must be equal to zero. In practice, this is impossible due to how floating point operations are performed in computational settings, and therefore are generally considered zero when the value converges on the order

of floating-point accuracy. Equation 2.43 states that the second derivative matrix of the energy, otherwise known as the system's Hessian, must contain all positive eigenvalues (be a positive-definite matrix). If these two conditions have been satisfied, then the converged geometry has reached a minimum. The challenge becomes, can one find an algorithm that can converge quickly, and not become trapped in local minima along the potential energy surface. The following sections describe in detail the optimization algorithms used in this work to find relaxed structures.

2.4.2 Conjugate gradient algorithm

The conjugate gradient [183] (CG) algorithm is a common optimization scheme that aims to find a numerical solution to a given system of linear equations (SLE). In particular, the CG algorithm is ideal for situations in which the SLE is a symmetric, positive-definite matrix, making it ideal for an energy minimization. The SLE can be defined as:

$$Ax = b \tag{2.44}$$

Where A is the symmetric positive-definite matrix, b is a matrix defined over all real numbers, and x is the solution to the SLE. The CG method assumes that a set of vectors $P = \{p_1, p_2, ..., p_n\}$ exists and is mutually conjugate with respect to A. One can then define a solution to this SLE as:

$$x^* = \sum_{i=1}^{n} \alpha_i p_i \tag{2.45}$$

Equation 2.45 can be manipulated to ultimately arrive at the expression:

$$p_j^T A x^* = \sum_{i=1}^{n} \alpha_i p_j^T A p_i \tag{2.46}$$

Upon closer inspection, one can see that $p_j^T A p_i$ is simply the inner product $\langle p_j, p_i \rangle$, which by definition results in $\langle p_j, p_i \rangle = 0 \forall i \neq j$, as the set P must be orthogonal to the

inner product of its elements. This definition eliminates the summation, and allows for the simple rearrangement of terms to solve for α_i:

$$\alpha_i = \frac{\langle p_i, b \rangle}{\langle p_i, p_i \rangle} \tag{2.47}$$

Therefore, one need only solve for α_i, and find a set of conjugate vectors P, and the SLE will always have a solution. While the CG method is a powerful minimization tool, it does suffer one major drawback; in general, the CG method requires n steps to reach convergence, where n is defined as the size of the matrix A. As an atomistic system may yield a n that is very large, it becomes extremely expensive to perform an optimization on these configurations. That being said, the CG method is used in this work for all unconstrained geometry optimizations.

2.4.3 Nudged elastic band algorithm

Unlike the unconstrained optimization of a single structure, discussed previously, one may find themselves needing to optimize multiple structures, together, along a pathway in the configuration space. Such an optimization falls into the broad class of constrained optimizations algorithms, and is very useful in finding the minimum energy pathway (MEP) for a reaction and/or diffusion mechanism. In this work, the nudged elastic band (NEB) algorithm [184, 185], along with the climbing image formalism [186], is used to discover such MEPs.

The NEB method follows a simple premise, in that the total force acting on an image along the reaction pathway can be broken into two components: (1) the true force, perpendicular to the band, and (2) a spring force, parallel to the band, serving to couple each image to the adjacent images. This can be represented as:

$$F_i = F_i^{spring}\big|_{\parallel} - F_i\big|_{\perp} \tag{2.48}$$

Where the true force is given by:

$$F_i|_{\perp} = F_i - F_i\hat{\tau}_i \tag{2.49}$$

Here $\hat{\tau}_i$ is defined as the local tangent at image i. In this work, $\hat{\tau}_i$ is calculated using the prescription outlined in [184, 185]. The spring force is then defined as:

$$F_i^{spring}|_{\parallel} = k(|R_{i+1} - R_i| - |R_i - R_{i-1}|)\hat{\tau}_i \tag{2.50}$$

Here k is represents a spring constant, and can be tuned by the user. With these constraints in place, an second optimization algorithm is used to move the images, with updated positions calculated using equation 2.48. The drawback to this definition of force is that there is no strict requirement regarding the transition state, as all images along the pathway are considered equal during the optimization. The climbing image formalism [186] helps to guide the band towards a saddle point by changing how the force is predicted on the image with the highest energy, after several iterations of the base NEB method described above. This new force calculation can be represented as:

$$F_{i_{max}} = F_{i_{max}} + 2F_{i_{max}}|_{\parallel} \tag{2.51}$$

Equation 2.51 effectively removes the spring force acting on the maximum energy image, allowing the image to climb up the PES along the band, and down the PES perpendicular to it. Such an constraint allows the maximum energy image to relax to a saddle point more effectively than the base NEB method defined in equation 2.48. As the other images along the band will eventually converge to the MEP, the reaction pathway around the converged saddle point will provide a robust approximation of the true set of images along the MEP.

CHAPTER 3
CAPTURING MULTI-SCALE SURFACE PHENOMENA IN ALUMINUM WITH MACHINE LEARNING

3.1 Introduction

As the fabrication of materials approaches the atomic-scale, an interest in layer by layer growth methods (such as molecular-beam epitaxy or atomic layer deposition), in electronics, catalysis, and/or biomedical applications, has risen sharply over the last few decades [187, 188]. Therefore, understanding how individual atomic-level process aid in the observation of macroscopic phenomena is of critical importance. Aluminum and Al-alloys are vital materials for such applications for many reasons e.g., electrical conductivity, recyclability to its original state, respectable corrosion resistance, etc [189, 190, 191, 192, 193]. Therefore, understanding how Al is fabricated, as well as how it breaks down, are crucial pieces of information for these applications, as their dependability directly depends on answers to these phenomena.

To this end, I have employed DFT and ML-AGNI force and energy models to study a multitude of surface properties of Al. Many of the DFT calculations present in this chapter are the first of their kind, and not only serve as reference data to both train and validate the ML-AGNI models, but also serve to understand the physics of the atomic-level processes being studied. In this chapter I focus on the following properties: (1) the minimum energy profiles of a plethora of adatom/vacancy diffusion pathways on the Al (111), (110), and (100) surfaces, (2) accurately predicting the melting temperature of the Al (111), (110), and (100) surfaces, as well as the size-dependant melting temperature of several (111)-(100) Wulff nano-particles, (3) the growth of 2D islands on the Al (111) surface, and (4) the epitaxial growth via atomic layer deposition on the Al (110) surface.

Table 3.1: The final fingerprint forms utilized to learn energy or atomic forces. For the property type, the subscripts i and I represent a per-atom or per-structure quantity respectively, and the superscripts α,β represent two possible Cartesian directions.

Property Type	# σ_k	σ_k Range (Å)	Final Fingerprint Form
Forces (F_i^α)	8	(1.0, 8.0)	$\mathbf{v}^1$
Energy (E_I)	20	(1.5, 8.0)	$\left\{ M^n\left(\sum_{i=1}^N S_{i,k}\right), M^n\left(\sum_{i=1}^N V_{i,k}\right), M^n\left(\sum_{i=1}^N T_{i,k}\right) \right\}$

3.2 Computational details

3.2.1 Machine learning model details

The ML-AGNI force and energy models used in this chapter were not created as part of this thesis, but were created using the AGNI platform [137, 169]. The force model employs the $\mathbf{v}^1$ fingerprinting scheme, along with KRR to map the features to the atomic forces. The energy model employs all three scalar, vector, and tensor components, along with KRR to map them to the total potential energy. Table 3.1 shows the final fingerprint forms for both mappings. Both models have previously been used to study a multitude of bulk and surface phenomena [137, 169]. However, they have still been relatively limited in the overall scope of the simulations used to validate them.

3.2.2 Nudged elastic band calculation details

For all defect diffusion mechanisms studied in this chapter, the energy barriers calculated were studied using DFT, EAM, and ML-AGNI to allow for a systematic and consistent comparison. The DFT calculations were performed on a 4-layer slab containing 101 atoms, plus any adatoms. The bottom layer remained fixed, giving the impression of a bulk-like region. All DFT calculations were done using the Vienna Ab Initio Simulation Package (VASP) [194, 195]. The PBE functional [196] was used to calculate the electronic exchange-correlation interaction. PAW potentials and plane-wave basis functions up to a kinetic energy cutoff of 500 eV were used [197]. All projection operators (involved in

the calculation of the non-local part of the PAW pseudopotentials) were evaluated in the reciprocal space to ensure further precision. The NEB routine [184, 185], along with the climbing image method [186] in the Transition State Tools package, was used with DFT energy calculations to predict the lowest energy pathway for each mechanism. Ionic relaxations were considered converged at an energy difference of 10^{-2} eV, and the electronic convergence was terminated at an energy difference of 10^{-5} eV.

EAM and ML-AGNI calculations were performed using a 5-layer slab of Al (100) containing 126 atoms, plus any adatoms. The bottom 2 layers remained fixed, making this structurally identical to the DFT slab. As mentioned earlier, three EAM potentials were considered (created by Voter, Liu, and Mishin) [198, 199, 200], henceforth referred to as EAM-V, EAM-L, EAM-M. EAM-V was chosen as it was used previously to predict the barrier heights of all Al (100) mechanisms considered in this work[201, 202]. EAM-M was chosen due to its popularity and ability to reproduce several mechanical and thermal properties of Al [200, 203, 204], but lack of study with regards to the surface behavior. Similarly, EAM-L was chosen owing to its success in reproducing complex behavior in good agreement with DFT [198, 199, 200].

All EAM and ML-AGNI NEB calculations were performed using LAMMPS [177]. Potential energy barriers were calculated using the NEB routine in tandem with the climbing image formalism. Owing to relatively low computational cost, a stricter convergence criteria of 10^{-5} eV/Å for forces and 10^{-8} eV for energy were used.

For all levels of theory, NEB calculated barrier heights were calculated with respect to the global barrier height, regardless of the number of local minima along a given reaction pathway. Such a definition stems from the assumption that the intermediate states can be assumed to be at steady state. From this assumption it can be shown that the largest barrier will dominate the overall reaction rate [205, 206].

3.2.3 Molecular dynamics details

All MD simulations were performed in the canonical ensemble using LAMMPS. The melting temperatures of the (111), (110), and (100) surfaces were calculated using a 2x2x20 supercell, in which neither the top, nor the bottom, of the slab was fixed. These sizes allow for thermal effects to dissipate between surface regions, to avoid having such oscillations effect the melting point. The melting temperature of the (111)-(100) Wulff clusters was also calculated using a clusters ranging from 1nm to 10nm in diameter.

To study the dynamic process of island growth on the Al (111) surface, a 35x30 $Å^2$ asymmetric surface model was constructed, with 5 dynamic layers and a bottom layer fixed in-place. The adatoms were then randomly distributed on the surface, and the concentration of adatoms, described by a coverage θ, was given as the ratio of adatoms on the surface to the maximum number of available three-fold sites. All dynamic simulations were performed in the canonical ensemble, with a timestep of 0.5 fs, and encompassed a simulation time of 2.5 ns.

To study the epitaxial growth of the Al (110) surface, MD simulations were performed, using an initial system size of 224,872 atoms, at 300K for 25ns, with deposition occurring for the first 10ns, and equilibration of the deposited atoms occurring over the final 15ns. Deposited atoms were randomly spawned from a region approximately 20 Åabove the surface, and given random initial velocities, though their velocity component, in the direction normal to the surface, ensured that the atom migrated towards the surface, and not away from it. Atoms were deposited at a rate of 1 $\frac{ML}{ns}$, which corresponds to approximately 1 new atom being spawned in the "spawn region" every 100 fs. This deposition rate ensures that atoms will not interact with each other prior to reaching the surface. While this restriction may leave out important physics, the ML-AGNI models cannot simulate gas-phase interactions, and therefore such a limitation is necessary.

Table 3.2: Melting temperatures of various aluminum surfaces as computed/predicted using experiments, ML-AGNI and EAM-V, EAM-L, and EAM-M, for the nine mechanisms considered in this work. Experimental values/ranges are also shown.

Surface	Exp. (K)	ML-AGNI (K)	EAM-V (K)	EAM-L (K)	EAM-M (K)
(111)	∼950 [209]	∼950	∼700	∼1000	∼1100
(110)	∼650-750 [209]	∼650	∼600	∼750	∼950
(100)	∼950 [209]	∼850	∼700	∼1000	∼1000

3.3 Predicting the melting temperature of Al surfaces and nanoparticles

The melting behavior of aluminum surfaces varies greatly, as the difference in packing densities leads to a a wide range of melting temperatures [207, 208]. Experimental observations indicate that, between the low-index (111), (110), and (100) surfaces, a difference in melting temperature of nearly 300K exists [209]. The (111) and (100) surface exhibit melting at the bulk melting temperature of between 900K and 950K. However, due to the packing density, the (110) surface has a melting temperature of between 600K and 800K [210]. This disparity becomes more complex when one moves from a slab to a nanoparticle, with small particles showing melting temperatures around 400K lower than that of the bulk melting temperature, and vary drastically as a function of their size [208, 211].

The melting temperature of the Al (111), (110), and (100) surfaces was calculated using three EAM potentials, and our ML-AGNI models. Figure 3.3 provides a histogram of the melting temperature values. Figure 3.1 shows, in the top row, the potential energy as a function of time at different temperatures for each case considered. The bottom row corresponds to the Lindemann index, calculated for all cases considered. From the EAM potential's perspective, there is no consensus among the potentials. EAM-V underestimates all melting temperatures, sometimes by several hundred degrees Kelvin, while EAM-M generally over-estimates all melting temperatures, though is often closer to the experimentally observed melting temperature [209]. EAM-L seems to be the robust EAM potential, when predicting the melting temperature of clean Al surfaces, showing excellent agreement with respect to experiments. The ML-AGNI models predict a melting temperature of approxi-

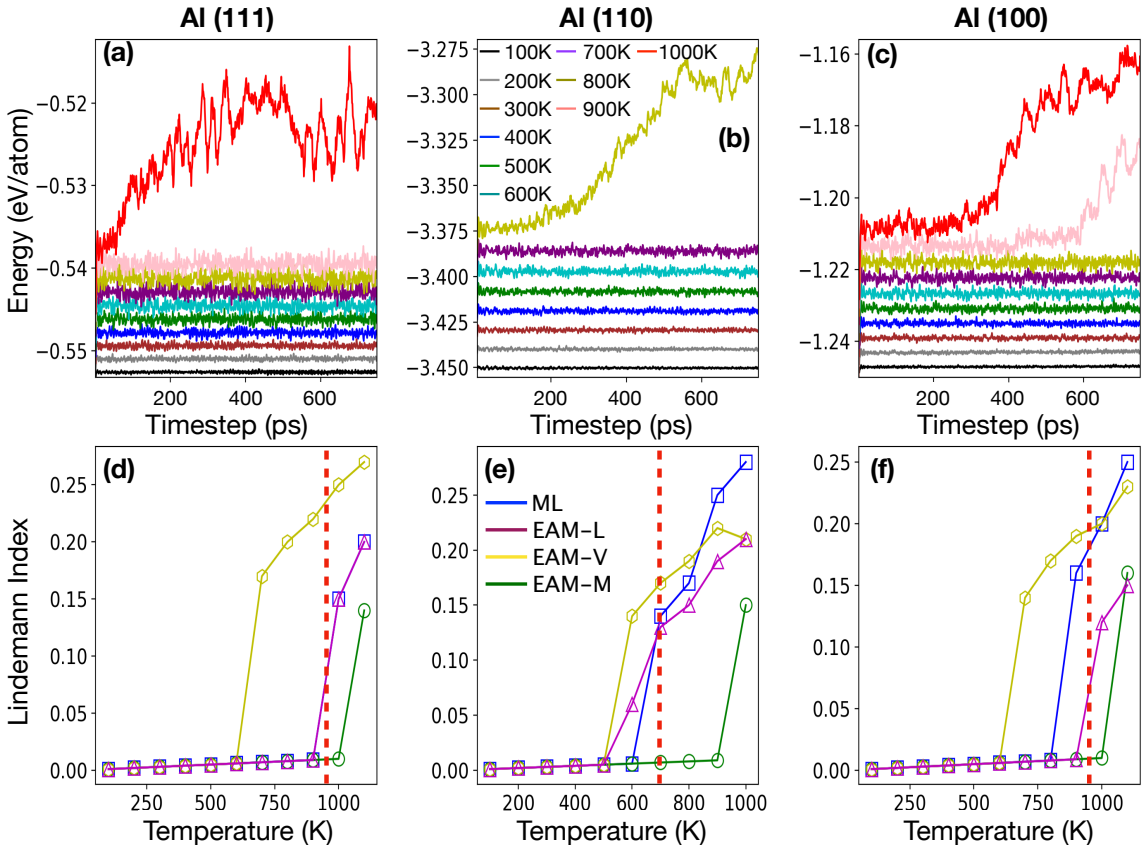

Figure 3.1: (Top) Potential energy, as a function of timestep during an MD simulation, for (a) Al (111) surface, (b) Al (110) surface, (c) Al (100) surface. Colors correspond to a particular temperature, and are the same throughout all top-row plots. (Bottom) Lindemann index, used to study the structural order of each system, calculated for the (d) Al (111) surface, (e) Al (110) surface, (f) Al (100) surface. Vertical red, dotted lines correspond to the experimentally predicted melting temperature.

mately 950K, 850K, and 750K for the (111), (100),and (110) surfaces respectively. These results are in good overall agreement with experiments [209], and are only out-performed, on the whole, by EAM-L.

The melting temperature of several Al nanoparticles was also considered in this work. It has been observed experimentally that the melting temperature of Al nanoparticles changes dramatically as a function of nanoparticle size, with particles 1nm in diameter showing a melting temperature nearly 400K less than that of a 10nm particle, which has a melting temperature close to that of bulk Al [212, 213]. To this end, MD simulations were performed, using all three EAM potentials and our ML-AGNI models. Figure 3.2 details the

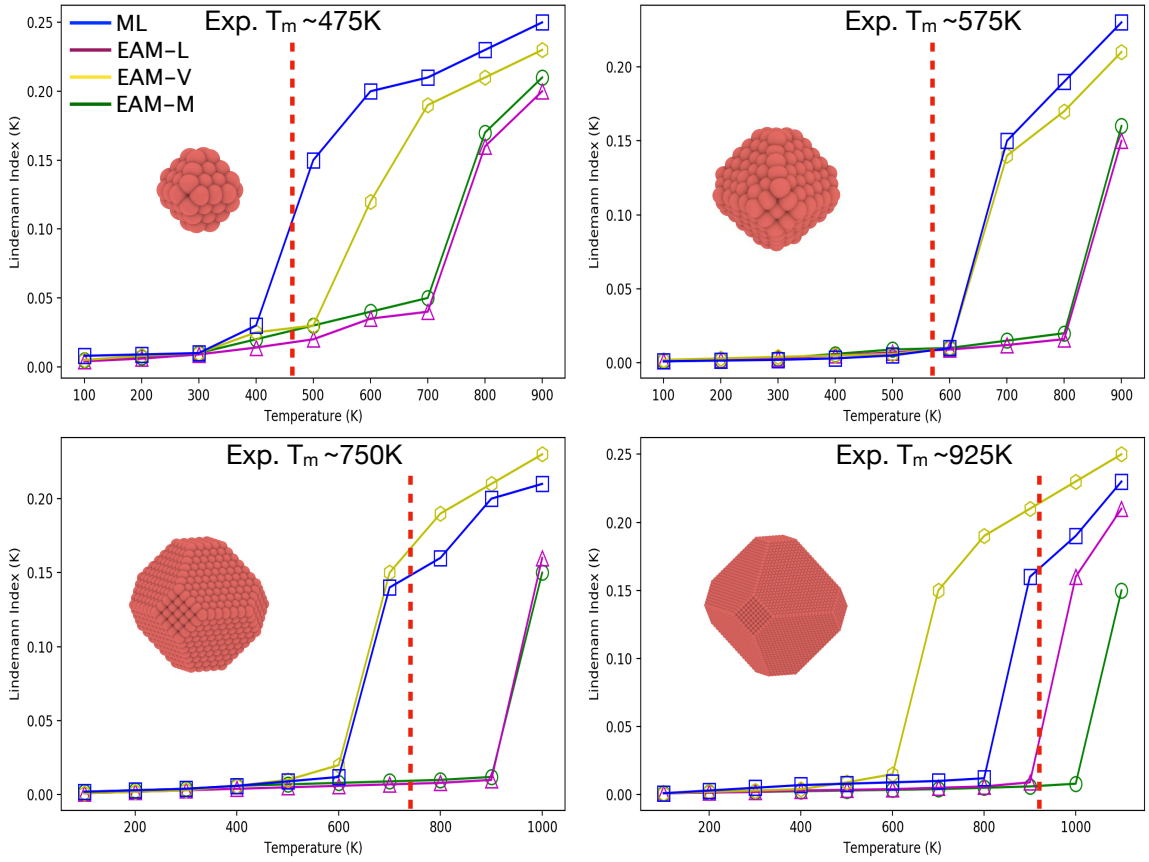

Figure 3.2: Lindemann index, used to study the structural order of each system, calculated for the (a) Al 1nm particle, (b) 2nm particle, (c) 4nm particle, and (d) 10nm particle. Vertical red, dotted lines correspond to the experimentally predicted melting temperature.

calculated Lindemann index for four nanoparticles, all of different sizes, while Figure 3.3 provides a histogram of the melting temperature values.

As was the case with the clean surfaces, there is no consensus amongst the EAM potentials, with dramatic differences in the melting temperatures being observed. Interestingly, the same trend exists, with EAM-M overestimating the melting temperature, and EAM-V generally underestimating (expect for the 1nm case in which it slight overestimates the melting temperature). While EAM-V performs well for small particles, it performs poorly for larger ones, with the opposite being true for EAM-M and EAM-L. Therefore, there is no single EAM potential one can use to accurately capture the trend correctly, with respect to experiments.

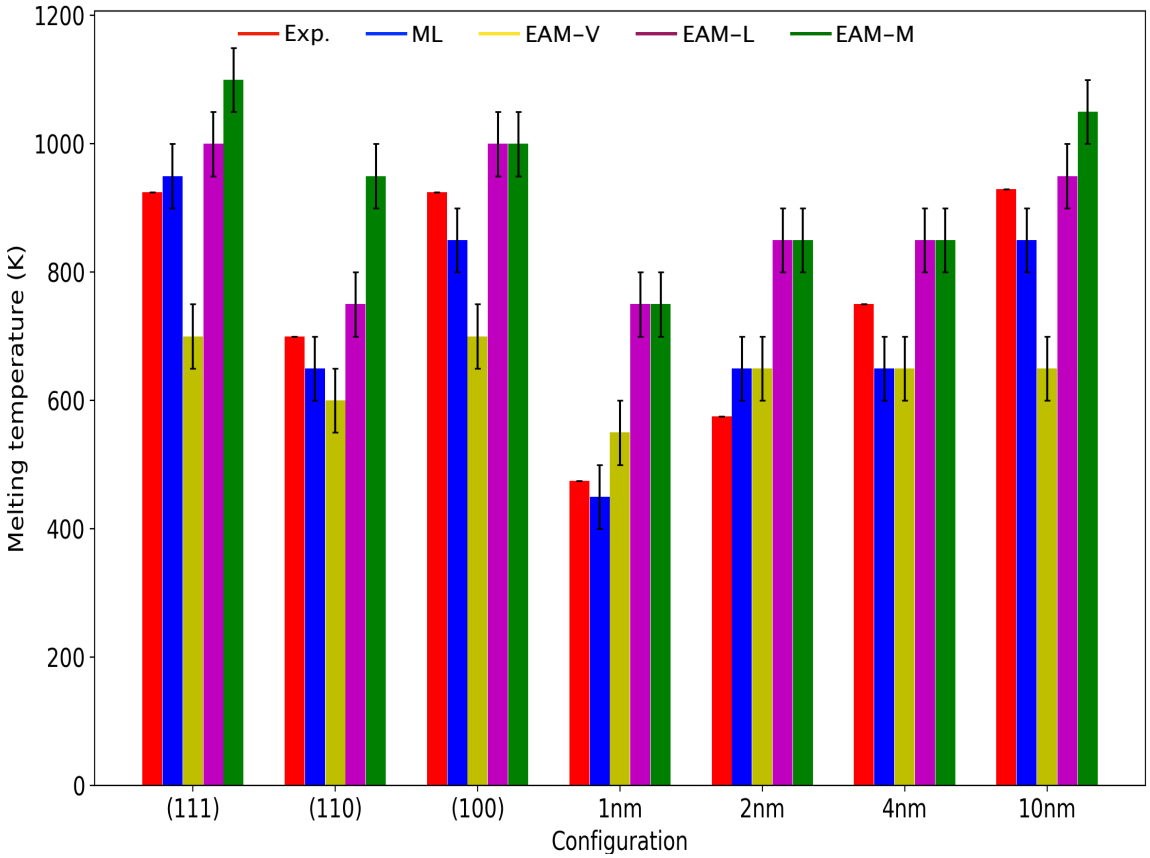

Figure 3.3: Melting temperatures for all configurations studied in this work. Colors correspond to the prediction method. Error bars correspond to the assumed error in a given calculation (experimental results are given as zero error, as the error is unknown, whereas the MD simulation error is given as 50K, as this is the error assumed given the Lindemann index calculations.)

3.4 Capturing the kinetics of defect diffusion on the Al (111), (110), and (100) surfaces

Accurate surface dynamics of materials has become crucial due to its relevance in technologically relevant applications, such as catalysis [214], thin films [215], crystal growth [216] and functional nano-materials [217]. Although experiments based on field-ion microscopy (FIM) and scanning tunneling microscopy can be used to elucidate surface diffusion mechanisms and rates [218, 219], the information available from these instruments is often limited in spatial and temporal resolution [220]. Computational methods based on

density functional theory (DFT), on the other hand, allow us to estimate the energy barriers and reaction rates associated with plausible diffusion mechanisms. Typically, numerical approaches such as the NEB method are used in conjunction with DFT to discover how energy pathways and transition state structures [166, 221, 222, 223].

3.4.1 Adatom diffusion on the Al (111) and Al (110) surfaces

Adatom diffusion on the Al (111) surface is an important surface science phenomena to understanding as the Al (111) surface will exist more frequently in nature due to it being the lowest energy surface [224]. However, because the surface is a close-packed surface, the number of unique adatom diffusion mechanisms that can occur is limited due to the energy required to move substrate atoms. The Al (110) surface, while occurring with less frequency than the Al (111) surface, is still an important surface when it comes to adatom diffusion due to the low packing density between rows, allowing for several competing adatom diffusion pathways [225].

The physical nature of adatom diffusion on the Al (111) surface paints a very simplistic picture, as only a hop to an adjacent site occurs with any real frequency. That being said, the exchange of the adatom with a substrate atom, pushing the substrate atom up above the surface layer, is also considered. The physical nature of adatom diffusion on the Al (110) surface is more complex [225], with the reduction in packing density allowing for more potential mechanisms to occur. However, in this work, only two mechanisms are considered: (1) a hop along a row, from one four-fold site to the next, and (2) the exchange between rows, in which an adatom replaces the position of a substrate atom, pushing this atom into the next row to serve as a new adatom.

The potential energy barriers for these mechanisms were studied with three EAM potentials and our ML-AGNI models. All potential energy barriers calculated in this subsection can be found in Table 3.3. For the simple (111) hop, all potentials show good agreement with both DFT and the experimental results [226, 227], with values ranging from 0.03 to

Table 3.3: Potential energy barrier for several adatom diffusion mechanisms on the Al (111) and Al (110) surfaces. all barriers are given in eV.

Property	Exp	DFT	ML	EAM-V	EAM-M	EAM-L
(111)						
$E_{a,hop}$	0.04	0.05	0.03	0.06	0.03	0.03
$E_{a,exc}$	-	0.72	1.09	0.74	1.05	1.02
(110)						
$E_{a,hop}$	0.43	0.47	0.33	0.19	0.36	0.30
$E_{a,exc}$	0.43	0.53	0.52	0.13	0.25	0.27

0.06 eV. However, for the case of exchange on the (111) surface, some disagreement exists. EAM-M, EAM-L, and our ML-AGNI models predict a barrier of around 1eV, while EAM-V and DFT predict a barrier of roughly 0.72. That being said, the take-away from this is that all potentials predict that the exchange on the (111) surface is significantly higher in energy than that of the simple hop.

For the Al (110) surface, a slightly more complex picture exists. For both the exchange and the hop, our calculated DFT results are in good agreement with experimentally observed values. However, for both cases, EAM-V significantly underestimates the potential energy barriers. While both EAM-L and EAM-M show decent agreement with the DFT predicted value of the hop mechanisms], they both significantly underestimate the barrier for the exchange mechanism. For both cases, our ML-AGNI models show the same level of agreement for the hop mechanisms that EAM-M and EAM-L show, but performs much better when estimating the barrier for the exchange mechanism, predicting a nearly identical result.

3.4.2 Adatom diffusion on the Al (100) surface

While the Al (111) and (110) surfaces are relatively simplistic in terms of the physical complexity of the pathways in which adatom diffusion can take, self-diffusion on the (100) sur-

face is not as restricted [228, 229]. For some metals, such as Al, Pt, Pd and Au, the adatom is known to diffuse by an exchange mechanism [230] (see Figure 3.4a) where an adatom pushes a surface atom up onto the surface, taking its place in the process. In contrast, for Cu and Rh, the adatom diffuses through a simple (and intuitive) hopping mechanism (see Figure 3.4d) from one 4-fold site to next [231]. This is in stark contrast to both the Al (111) in which an adatom hop is universally lower in energy than an exchange process, as well as the Al (110) surface in which only a few diffusion pathways are even possible, due to the physical structure of the surface.

Furthermore, a multitude of non-trivial low-energy diffusion mechanisms have been shown to exist in the case of Al (100) surface [230, 201, 202, 232, 233]. The complexity of such mechanisms can be seen in Figure 3.4. Besides exchange mechanisms being preferred over the hopping mechanism, past studies have also shown that some complex vacancy-based mechanisms (Figure 3.4f, 3.4e) [201, 202] have similar energy barriers to that of the intuitive hop. Such mechanisms have only been studied with classical parameterized potentials, however, and the question regarding which processes dominate the (100) crystal growth is yet to be answered.

In this section, I have created a catalog of nine mechanisms, varying in both energy and physical complexity, guided by previous work [201, 202, 234]. These nine mechanisms involve atomic exchange, hopping, and vacancy-formation, all involving the same initial configuration of a single adatom on an otherwise clean (100) surface. The physical nature of these nine mechanisms is described in detail throughout this section. The mechanisms are labeled **a**-**i** in the order of increasing barrier height; **a** corresponds to the lowest and **i** to the mechanism with highest barrier energy. In the case where multiple barriers exist along a given pathway, the largest among them is reported as the barrier corresponding to that mechanism. All nine mechanisms are illustrated in Figure 3.4.

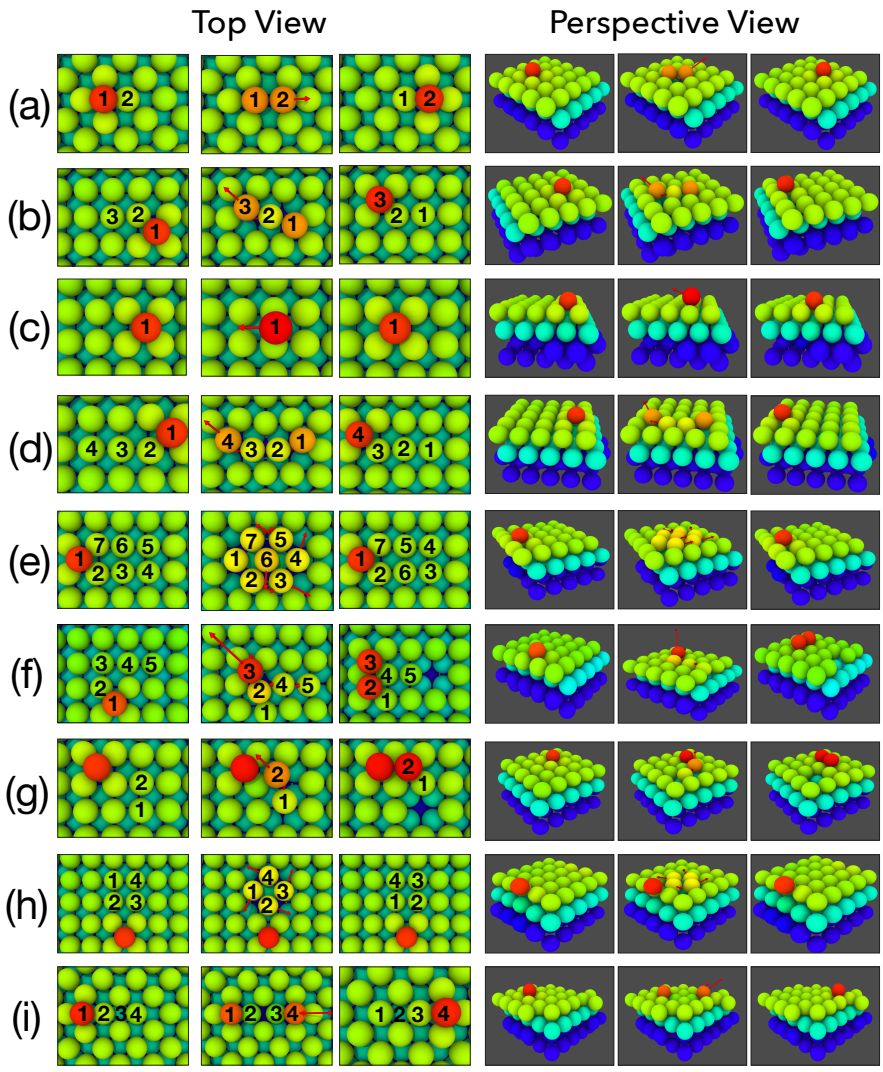

Figure 3.4: The top and perspective views of the nine surface diffusion mechanisms studied in this work. Moving from left to right, the initial, mid-point, and final configurations along the reaction pathway are presented in each view. The atoms are colored corresponding to their height along the surface normal to serve as a guide to the eye. For each mechanism, relevant atoms are numbered to help track their trajectory, and red arrows are used to indicate current trajectory of the atoms.

Physical nature of the diffusion pathways

Mechanism **a** corresponds to the previously discussed two-atom exchange involving an adatom and a surface atom. The adatom pushes a surface atom up onto the surface, taking its place in the process. Mechanism **b** is a 3-atom exchange where an adatom pushes its way into the surface, causing 2 surface atoms to move within the surface plane until the furthest surface atom involved in the exchange is pushed up onto the surface as an adatom. The most simple and intuitive mechanism considered in this work is Mechanism **c** which involves an adatom hopping from one 4-fold site to another, as stated earlier. Mechanism **d** is a 4-atom exchange where an adatom pushes its way into the surface, causing 3 surface atoms to move in a line, within the surface plane, until the furthest surface atom is pushed onto the surface as a new adatom.

Mechanism **e** is a highly complex set of atomic exchanges where various atoms swap positions. This mechanism, as dilettante as it may sound, is reminiscent of a game of musical chairs. The adatom first exchanges with a surface atom, which in turn exchanges, within the surface plane, with a neighboring atom. This process of surface-plane exchange continues in a circular path until the original adatom is pushed back atop the surface to its original position. While the adatoms initial and final positions remain constant, the various surface atoms involved have all exchanged places. This mechanism is arguably the most structurally complex of the nine mechanisms considered here, as reflected by the presence of multiple saddle points along the potential energy surface (PES), to be discussed later (see Figure 3.5).

Mechanism **f** is a 2-part exchange and vacancy creation involving 5 atoms. The first process involves an adatom exchanging with its nearest surface atom, which in turn exchanges with a neighboring surface atom, pushing that atom onto the surface. This process is identical to mechanism **b**. The second part of this process involves 3 surface atoms exchanging, one of which gets pushed onto the surface. This ultimately creates 2 adjacent adatoms, and a surface vacancy.

Mechanism **g** is a vacancy formation mechanism involving a surface atom pushing upon an adjacent surface atom on top of the surface. This new adatom sits adjacent to another adatom. Mechanism **h** involves 4 surface atoms rotating parallel to the surface plane, similar to that of a spinning windmill. At the center of the axis of rotation for the 4 surface atoms exists a 4-fold site. An adatom is located two 4-fold sites away, following any arbitrary straight path. The adatom is not directly involved in the mechanism, but does exert its influence by keeping all exchanging atoms to the surface plane.

Mechanism **i** involves two surface layers rather than one. An atom on the second layer pushes an atom above it until that atom eventually makes its way above the surface as an adatom, where the second layer atom now takes its place. Having a vacancy now formed in the second layer, another adatom pushes down on a surface atom, which in turn rushes to fill the vacancy, with the second adatom taking its place.

Minimum energy profiles

Figure 3.5 showcases the minimum energy profiles for all nine mechanisms considered, while Table 3.4 provides the raw values. Some available literature results, also calculated using DFT but with different exchange-correlation functionals, are included and show good agreement with our computed values. We see that the adatom-surface exchange, mechanism **a**, has a potential energy barrier roughly 3 times less than that of the 4-fold adatom hop, mechanism **c**. As stated previously, mechanisms **b** and **d** also have a potential barrier less than or equal to that of the 4-fold adatom hop. Mechanisms **e** and **f** show a barrier within 0.2 eV of the hop, indicating they could occur with similar frequency. Mechanisms **g** through **i** yield substantially larger barriers and thus are predicted to occur less frequently.

Figure 3.5 clearly suggests that both EAM-L and EAM-M over-estimate the energy barrier for almost all mechanisms. Naturally, due to this inconsistency in barrier heights, the rate of occurrence of each of these mechanism will be substantially lower than that predicted by DFT during molecular dynamics simulations. Further, elevated temperatures

Table 3.4: Al (100) surface diffusion energy barriers, as computed using DFT, ML-AGNI and EAM-V, EAM-L, and EAM-M, for the nine mechanisms considered in this work. Past computations are included in brackets.

Mechanism	Type	DFT (eV)	ML-AGNI (eV)	EAM-V (eV)	EAM-L (eV)	EAM-M (eV)
a	exchange	0.27 [23]	0.31	0.30 [23]	0.63[23]	0.81[23]
b	exchange	0.63 [23]	0.63	0.63[23]	1.00[23]	1.04[23]
c	hop	0.63 [23]	0.42	0.46[23]	0.52[23]	0.53 [23]
d	exchange	0.68 [23]	0.67	0.66 [23]	1.20[23]	1.16[23]
e	exchange	0.75 [23]	0.72	0.84 [23]	1.42[23]	1.60[23]
f	vacancy	0.81 [23]	1.25	0.88[23]	1.19[23]	1.05[23]
g	vacancy	0.89 [23]	1.03	0.90[23]	1.05[23]	0.95[23]
h	exchange	1.03 [23]	0.94	0.94[23]	1.33 [23]	1.34 [23]
i	exchange	1.22 [23]	1.24	1.04[23]	1.38[23]	1.49[23]

will be needed to activate these mechanisms. In contrast, the EAM-V potential captures most barrier heights within 0.12 eV, but fails to capture the energy profile's shape as the complexity increases. This difference can lead to certain pathways being kinetically locked, or favored, at incorrect thermal energies. Thus, no single EAM potential can completely describe the complex nature of adatom surface diffusion on Al (100).

The ML-AGNI force and energy models were also used to predict the MEPs of all nine (100) mechanisms. Overall, the ML-AGNI results align extremely well with DFT. The ML-AGNI profile shape agrees more with respect to DFT than EAM-V's MEP shape, and the ML-AGNI transition state energies yeild an RMSE of 0.21 eV, compared to an RMSE of 0.33 eV and 0.35 eV for EAM-L and EAM-M respectively. While this 0.21 eV RMSE is higher than that of EAM-V's 0.1 eV, this difference can be attributed to the ML-AGNI prediction on mechanism **f**, which is 0.44 eV off compared to DFT. The ML-AGNI RMSE, comapred to DFT, on all mechanisms not including mechanism **f** is 0.08, which is 0.02 eV lower than EAM-V's RMSE of 0.1 on all mechanisms not including mechanism

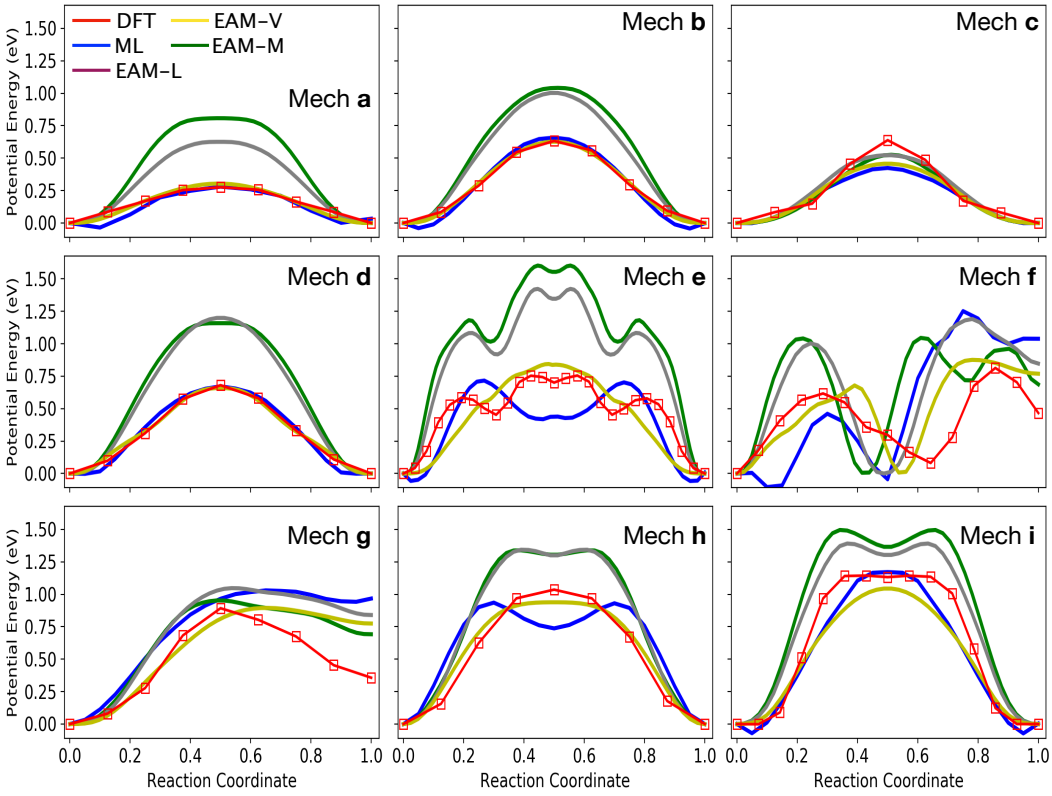

Figure 3.5: Minimum energy profiles for all nine mechanisms studied in this work using DFT, ML-AGNI-AGNI and EAM-V,C, and M. Mechanisms are organized in the order of increasing DFT potential energy barriers.

f. This result, along with the fact that the ML-AGNI MEP shapes are more aligned with DFT than EAM'V's profile shapes, indicate that the ML-AGNI models can more reliably predict the kinetics of adatom/vacancy diffusion profiles on the Al (100) surface. The other benefit of ML-AGNI over EAM, is that, while mechanism **f** is clearly poorly predicted on the part of ML-AGNI, the ML-AGNI models can be iteratively improved by including the configuration from that mechanisms in its training set and retraining the model.

3.5 Surface clustering and growth on the Al (111) and (110) surfaces

Island nucleation on the Al (111) surface

The 2D clustering of adatoms into islands, as a function of initial surface coverage and temperature, was simulated on the Al (111) surface. 2D growth involves numerous unique

surface diffusion pathways that either an individual adatom or cluster can take [235]. While the previous section regarding adatom diffusion showed excellent agreement between our ML-AGNI platform and DFT, the NEB calculations do not considering temperature effects that a truly dynamic environment encounters.

We began by exploring the time-evolution of a system with $\theta = 0.14$ at 300 K. Snapshots during the course of the simulations are shown in Figure 3.6 (right top), for several nanoseconds. The randomly distributed adatoms form small islands, within a few picoseconds, with a densities between 3-6 atoms. Once these small islands have formed, they remain kinetically locked and therefore retain their shape and density. This observation is consistent with past theoretical studies in which dimers, trimers, and larger clusters were shown to be stable once formed and preferred to move in a together, rather than dissociate [236, 237, 238].

As the surface coverage is increased to $\theta = 0.31$ and $\theta = 0.45$, the growth process leads to distinctly different island shapes. At higher coverages, the small compact islands become large fractal-like clusters. However, a direct comparison with experiments on the island shape is difficult due to the time and length-scales required to accurately observe such phenomena. One would need to employ simulation methods such as kineic Monte Carlo simulations or accelerated MD techniques to reach such scales. Nevertheless, the goal of studying different initial coverages is to show that the ML-AGNI models can reliably reproduce the qualitative trends observed by experiments, given the time and length scales we can reasonably cover.

Temperature also plays a crucial role in the morphology of the islands. Past experimental studies, at $\theta = 0.11$, by Busse et al. revealed distinct structural patterns for islands that formed in a temperature range of 50-300 K [239, 240]. At low temperatures the lack of thermal energy results in small islands, as adatoms that were initially close together were able to make short hops to form small islands, which transitions into larger, more compact islands as the temperature increases. To better understand the role of temperature,

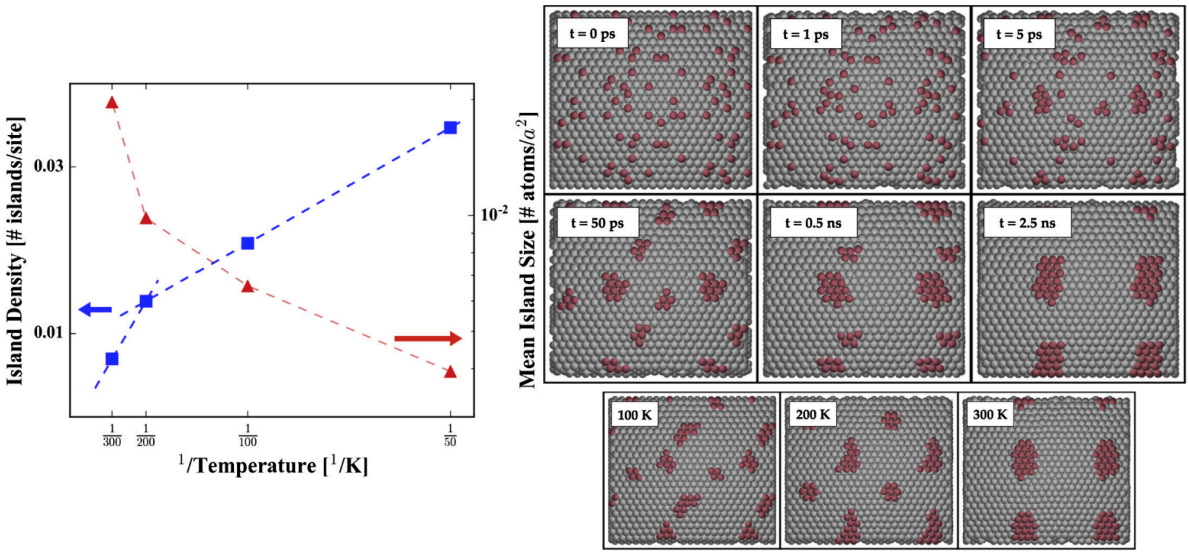

Figure 3.6: Left panel: Island density and size as a function of temperature. a^2 refers to the surface area of the basal plane. Two scaling regimes are observed with a transition temperature of 200K. Right panel: Island ripening as a function of temperature and time. Grey and red colored atoms correspond to the surface atoms and adatoms, respectively. The top panel shows snapshots of the time-evolution of adatoms on Al (111) surface using constant temperature (300 K) molecular dynamics simulation. Adatoms were randoML-AGNIy distributed on the surface as shown t = 0 ps, θ = 0.14. The images shown are a 2x2 repeat of the unit cell. The bottom panel highlights a simulation at the end of 2.5ns for 100K, 200K, 300K, θ = 0.14.

dynamical simulations between 50 K and 300 K were performed, as shown in Figure 3.6 (right bottom). At 100 K, we observe several small islands that remain kinetically locked after formation. At 200 K, the islands take on dendritic shapes, in which adatoms clusters together with little subsequent rearrangement.

Further, in the case of an Al (111) surface Busse et al. experimentally observed two distinct growth regimes, as measured by the change in island density as a function of temperature (T): (1) T$<$ 200 K, (2) T$>$ 200 K [239, 240]. From the MD simulations described above, we have observed an identical transition, T =200 K, shown in Figure 3.6 (left). For the two regimes we compute the activation energy by measuring the slope of each domain, resulting in values of 1.2 K^{-1} and 4.2 K^{-1}. The consistent features observed, both in island shapes and growth regimes, suggests that the MD simulations undertaken with our

ML-AGNI force model is capable of capturing both the thermodynamics and kinetics of the ripening process.

Expitaxial growth on the Al (110) surface

In the previous section, the clustering of adatoms, already present on the surface, at different temperatures and coverages proved that the ML-AGNI models can be reliably used, and qualitatively compared with experiments, to study surface growth processes. However, such a study is only vaguely connected to experimental observations due to the time and length scales employed. In this section, the connection to experiments is expanded upon, by directly observing the shapes and sizes of 3D surface features after atoms are dynamically deposited on the Al (110) surface.

AFM images of epitaxial growth on the Al (110) surface [241], via atomic-layer deposition, provides us with quantitative values in which to benchmark our ML-AGNI models against. At 300K, pyramidal clusters form on the surface, with lengths and heights approximately three and six times smaller than their width, respectively. While the MD simulations performed in this section will still not reach the time and length scales observed in experiments, the time and length-scales used can provide exact qualitative measurements; the size of the pyramidal clusters may be an order of magnitude smaller via MD, but the height-width-length relationship can match experimental observations.

It can be seen from Figure 3.7 that the height-width-length relationship obtained from the ML-AGNI MD simulations match extremely well with experimental observations. The width, height, and length of clusters were calculated as the average of all clusters present at the end of the MD simulation. The height, specifically, was calculated as the distance from the nearest mono-layer atom to the top of a given cluster. The measured average cluster width was measured as 22.31 Å, almost exactly three times smaller than the 68.72 Åwidth. The average cluster height was calculated to be 10.92 Å, in near perfect agreement with the experimental observation of the cluster height to width ratio of 6:1.

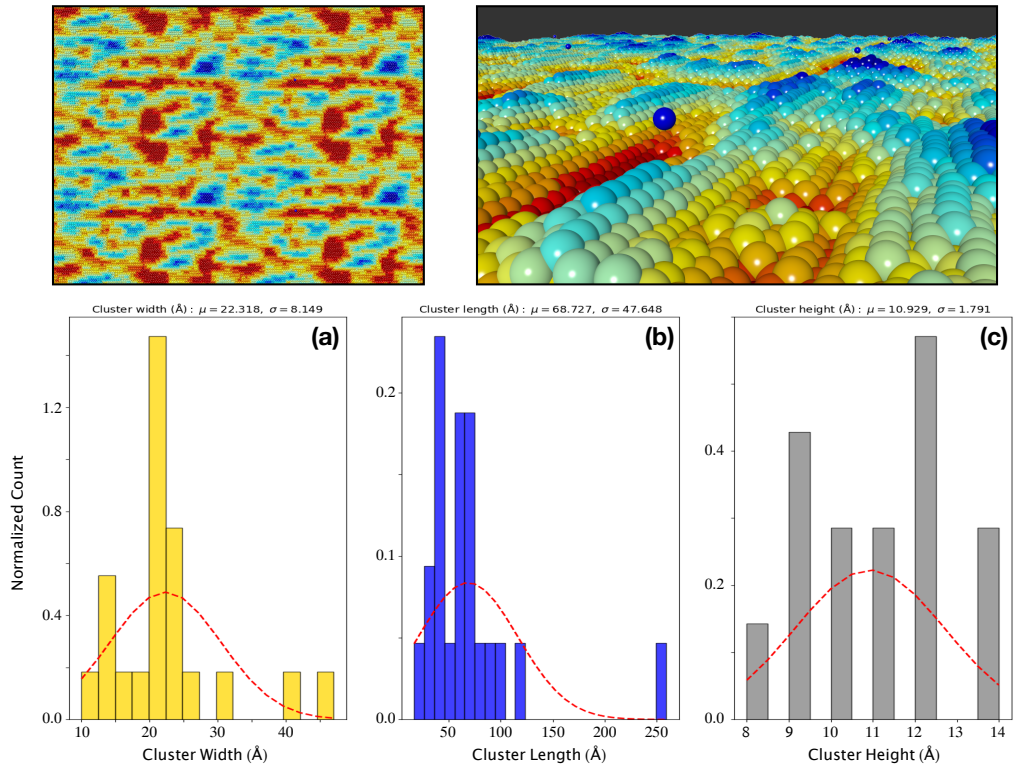

Figure 3.7: (Top) A 2x2 replicated top-down view, shown on the left, and a 3x3 replicated perspective view, shown on the right, of the epitaxial growth of the Al (110 surface. Colors corresponding to the z-position of an atom, with red representing smaller, and blue representing a larger z-position. (Bottom) Normalized histograms for the (a) width, (b) length, and (c) height, of the deposited clusters on the surface after both deposition and equilibration had occurred.)

To build upon the agreement with experiments, Figure 3.7 shows the top-down and perspective views of the Al (110) surface at the end of the MD simulation. AFM images indicate long, tube-shaped clusters spread throughout the surface, with small clusters and valleys filling the remaining space [241]. Figure 3.7 indicates similar surface features, obtained via the MD simulations, being present. The perspective view of the final ML-AGNI simulated structure also clearly shows pyramidal structures being present, whose width-length ratio resembles the long tube-like shape observed in experiments.

3.6 Summary

In this chapter, previously created ML-AGNI force energy models were used to study a multitude of surface phenomena of aluminum. Here, we further extend the scope of previous ML-AGNI works by tackling simulations of increasingly complex physical systems, and significantly larger time and length scales than had been previously considered. The various ML-AGNI models were validated by accurately reproducing the MEPs of a plethora of defect diffusion mechanisms on several low-index Al surfaces, accurately reproducing the correct the melting temperatures of Al surfaces and nano-particles, qualitatively capturing the growth behavior of islands on the (111) surface, and accurately reproducing experimental observations of the cluster shapes and sizes during the epitaxial growth, via atomic-layer deposition, of the Al(110) surface.

The ML-AGNI calculations presented in this chapter show a clear improvement over many commonly used EAM potentials, as well as the subtle improvement over other EAM potentials less commonly used, when considering the MEPs calculated in this chapter. The ML-AGNI models presented here also, purposefully, do not contain reference data for all of the environments studied, indicating there extrapolative power allows them to be reliably used to study a plethora of surface phenomena. Using ML-AGNI models, with the accuracy of DFT, and the speed of classical/semi-empirical models, allows us to accurately and reliably study properties far beyond the reach of DFT. This work adds another layer of proof that ML-AGNI models can make accurate and reliable predictions over multiple length and time-scales, further bridging the gap between DFT and experiments for the study of surface phenomena.

CHAPTER 4
CAPTURING MULTI-SCALE DEFECT PHENOMENA IN PLATINUM WITH MACHINE LEARNING

4.1 Introduction

Many dynamic mechanical phenomena, such as the growth of grains, the temperature dependence of a material's mechanical/elastic properties, and the nucleation of voids, are all governed by individual atomistic processes interacting with one another [16, 17, 18]. However, accurately capturing the intricacies of such processes is often non-trivial, owing to the complexity of the interactions, as well as the time and length scales required to accurately study them [19]. Therefore, any strategy that probes the atomic regime, be it experimental or computational, must be capable of capturing the dynamic evolution of atomistic processes.

Platinum is chosen here because of its commercial importance, particularly in the regime of catalysis [242, 243, 244, 245, 246, 247, 248], as well as its importance as a bulk material, in part because of its strong mechanical properties and high melting temperature [249, 250, 251]. Classical methods have generally struggled to accurately, and universally predict both Pt's surface and bulk properties [252, 253]. While less complex properties, such as the cohesive energy, can be accurately reproduced by many semi-empirical models, more complex phenomena such as the activation energy of a single vacancy, are not reliable [253]. To this end, predictions of more complex properties, such as the dissociation of coupled vacancies, void nucleation, and melting, which are governed by the interactions of less complex phenomena [254, 255, 256], cannot be universally trusted. Therefore, ML can be employed to fill this void and bring the community closer to bridging the gap between QM methods and experimental observations for Pt.

In this chapter, I demonstrate the use of our ML-AGNI platform, in predicting a multitude of properties in Platinum over several length and time-scales. Properties, such as the bulk modulus, vacancy formation energy, and elastic constants, among others, are predicted. Ionic relaxations of highly disordered systems, as well as calculations of phonon frequencies are used to show how our ML-AGNI models respond to both large and small atomic perturbations. The diffusion of a single vacancy within an otherwise pristine bulk system is considered, along with how entropic effects can help to lower the activation barrier for diffusion. The kinetics of the dissociation and diffusion of a divacancy are simulated via nudged elastic band calculations. I demonstrate the use of the AGNI models in exploring how the mechanical properties of Platinum are affected by changes in temperature. Atomic-level properties, such as grain boundary and surface energies, as well as adatom and dimer binding and adsorption energies on several surfaces are calculated to show the models capabilities at accurately capturing the complexity and diversity of atomic-level defect properties. Grain coarsening simulations are also performed, and compared to experimental observations, to explore the ML-AGNI models ability to accurately simulate the dynamic behavior of nano-meter phenomena. The compilation of work presented in this chapter aims to truly realize the potential of ML-AGNI methodologies for the study of materials phenomena over many time and length-scales, bridging the gap between QM, semi-empirical/classical, and experimental methodologies.

4.2 Computational Details

4.2.1 Density functional theory details

All DFT calculations were performed using VASP [194, 195]. The PBE functional [196] was used to calculate the electronic exchange-correlation interaction. PAW potentials and plane-wave basis functions up to a kinetic energy cutoff of 500 eV were used [197]. All projection operators (involved in the calculation of the non-local part of the PAW pseudopotentials) were evaluated in the reciprocal space to ensure further precision. K-poimt

convergence was carefully calibrated to ensure both convergence of energy, but also forces, where possible. However, due to the size of several system considered in this chapter, the convergence with respect to forces could not be met. For all NEB calculations, ionic relaxations considered converged at an energy difference of 10^{-2} eV, and electronic convergence terminated at an energy difference of 10^{-4} eV.

4.2.2 Embedded atom method details

Three EAM potentials, henceforth referred to as EAM-B[249] EAM-Z [250], and EAM-F [251] (due to their respective authors) were chosen for this work and were used as a comparison to the ML-AGNI platform presented in this work. All EAM potentials were chosen for their ability to accurately capture a variety of bulk properties for Pt with respect to experimental evidence.

4.2.3 Machine learning model details

In this section two sets of ML-AGNI models were developed, one pertaining to section 4.3, and the other corresponding to section 4.4. This is due to the use of an iterative improvement method [168], in which new data was added to the first model in order to study new phenomena. The final fingerprint forms for all models are provided in Table 4.3. The following paragraphs detail both processes.

Iteration 1

A comprehensive set of reference data, summarized in Table 4.1, was prepared for Pt in an accurate and uniform manner in order to minimize numerical noise intrinsic to atomistic calculations. All reference data was obtained using VASP [194, 195, 184, 185, 186], with computational details described in section 4.2.1.

During the training phase of the first model creation process, statistical measures were used to determine if a given model is capable of making reliable predictions. In Figure 4.1,

Table 4.1: Summary of the reference data set that was prepared for Platinum ML-AGNI model generation. The data is divided into subsets based on the type of defect that is present. T=0K are designated as either NEB calculations or geometry relaxations, where T>0K represents MD calculations. The final column, titled ML-AGNI iteration, indicates which set of ML-AGNI models contain a particular dataset (1 being the first iteration, used in section 4.3, and 2 being the second iteration, used in section 4.4).

Defect Type	Systems	Temperature (K)	ML-AGNI iteration
Defect-free	Bulk (w/o strain)	300,1000,2000	1,2
Strained Bulk	Bulk (w/ strain $\pm$ 7 %)	300,1000,2000	1,2
Monovacancy	Bulk with 1 vacancy	0 (NEB), 1000, 1500, 2000	1,2
Divacancy	Bulk with Divacancy	0 (NEB), 1000, 1500, 2000	1,2
Clustered vacancies	Bulk with 4 vacancies	1000, 1500, 2000	1,2
Grain boundary	Assorted GBs between $\sum$3 and $\sum$25	0 (Relax),300,1000,1500	2
Grain boundary + vacancy	Assorted GBs between $\sum$3 and $\sum$25	0 (Relax), 0 (NEB)	2
Surface	Slabs corresponding to GB planes	0,300,600,1000,1500	2
Surface + adatom/dimer	Adatoms and dimers on (111), (110), and (100)	0(Relax), 0(NEB)	2
Dislocation	Edge and screw dislocations	0(Relax)	2

Table 4.2: Statistical error metrics of the final ML-AGNI models, for each property learned, generated in this work. All values presented here are the metrics calculated on a given model's test set, not a model's training set. The final rows correspond to the number of training points in the final models. Iteration 1 and 2 correspond to the data present in the model's training sets, as described in section 4.2.3.

Error Metric	Energy model (meV/atom)	Force model (eV/Å)	Stress model (GPa)
Iteration 1			
RMSE	2.73	0.15	0.42
STD	2.71	0.15	0.41
Max 1 % Error	7.90	0.80	1.68
r^2	0.99	0.99	0.99
# Training Points	1728	3000	3000
Iteration 2			
RMSE	6.39	0.23	1.23
STD	6.40	0.22	1.24
Max 1 % Error	12.34	1.83	7.79
r^2	0.99	0.99	0.98
# Training Points	2832	4500	5000

Table 4.3: The final fingerprint forms utilized to learn energy, stresses, or atomic forces. For the property type, the subscripts i and I represent a per-atom or per-structure quantity respectively, and the superscripts α,β represent two possible Cartesian directions.

Property Type	# σ_k	σ_k Range (Å)	Final Fingerprint Form
Forces (F_i^α)	8	(1.0, 8.0)	$\mathbf{v}^1_{i,\alpha;k}$
Stresses ($S_I^{\alpha,\beta}$)	20	(1.5, 11.5)	$\left\{ M^n\left(\sum_{i=1}^N T_{i,\{\alpha,\beta\};k}\right) \right\}$
Energy (E_I)	20	(1.5, 11.5)	$\left\{ M^n\left(\sum_{i=1}^N S_{i,k}\right), M^n\left(\sum_{i=1}^N V_{i,k}\right), M^n\left(\sum_{i=1}^N T_{i,k}\right) \right\}$

several such metrics are provided: (1) the root mean square error (RMSE) as a function of the number of training points, (2) the maximum 1 % error as a function of the number of training points, and (3) a parity plot for the best generated model. For all three cases, both the overall RMSE, as well as the maximum 1% error, decrease as the training set size increases.

However, saturation occurs in the overall learning for all models by a training set size of 3000 points. All statistical error metrics for the first model iteration for the final ML-AGNI models can be seen in Table 4.2. Overall, these metrics indicate that all three ML-AGNI models can adequately capture their respective DFT reference data over a large range of external conditions. However, such statistical metrics are not the deciding factor when determining if a given model can be used to simulate dynamical material properties. Further validation, as seen in the section 4.3, must be performed to say that a given ML-AGNI model can be confidently deployed to study more complex phenomena.

Iteration 2

While the first set of models was trained only to simulate environments close to defect-free bulk, strained defect-free bulk, and bulk with vacancies. More complex phenomena, such a planar and line defects, and combinations of these defect classes, shown in Table 4.1, were not present in the ML-AGNI model's respective training sets. Before performing simulations of these new systems, the model's predictions of potential energy, atomic forces, and the total stress tensor were compared to the reference DFT data. Parity plots, shown in Figure 4.2 (top), indicate that, while the previous ML-AGNI models perform well for grain boundary configurations, they cannot make reliable predictions on surface environments. Therefore, these systems must be added to the three model's training sets before performing any simulations.

Using an iterative improvement scheme developed for our ML-AGNI force models [168], failed configurations were continuously added to all three ML-AGNI model's train-

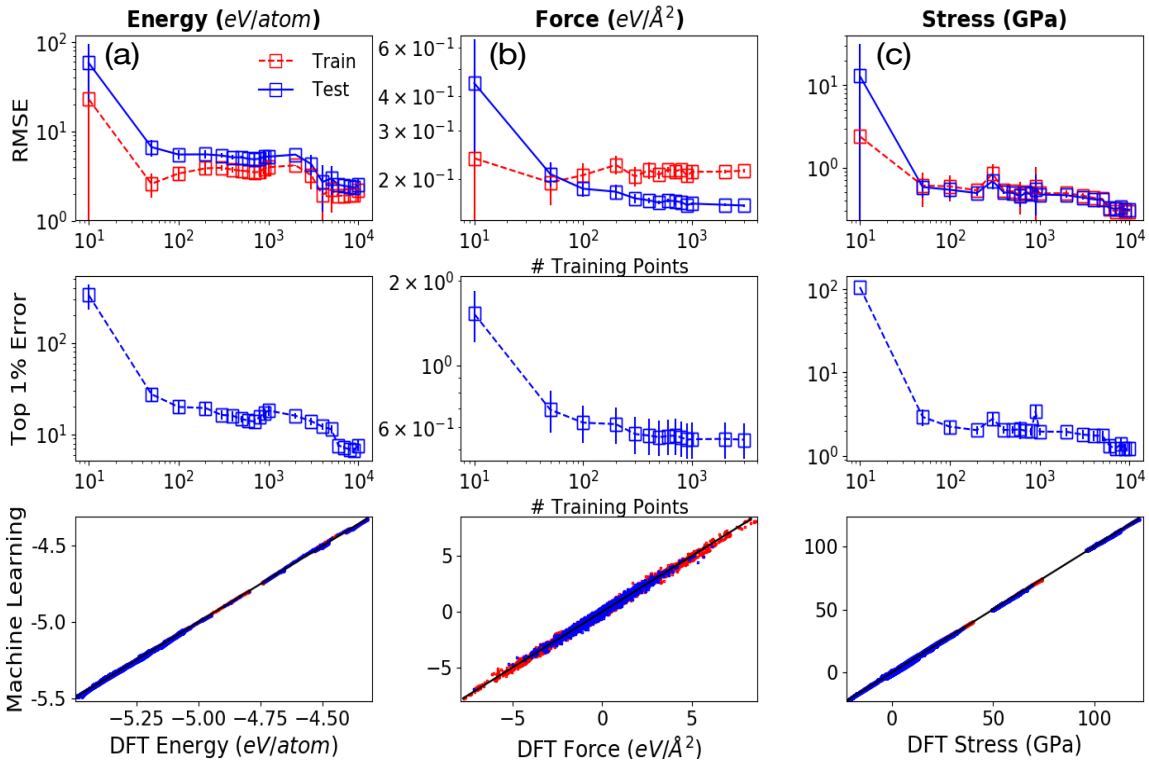

Figure 4.1: Statistical error metrics used to compare ML-AGNI models during the optimization process. The columns are labelled as (a) Energy, (b) Force, (c) Stress. The top row shows the average RMSE of both the training and test sets. The middle row measures the max 1% error of the test set. The x-axis for the top two rows corresponds to the number of training points in a given model. The bottom row shows parity plots of the final model used throughout this work. Column titles indicate the property's units.

ing sets until statistical metrics reached convergence. All statistical error metrics regarding the second model iteration for the final ML-AGNI models can be seen in Table 4.2. From Figure 4.2 (bottom), a clear improvement in all ML-AGNI models can been seen. With converged statistical metrics showing significant improvement in the model's performance, when encountering previously disparate domains in the configuration space, the ML-AGNI models can be reliably deployed to study the phenomena described in section 4.4.

4.2.4 Simulation details

All MD simulations (outside of DFT reference data generation) were performed using LAMMPS [177]. Vibrational calculations were performed using the Atomic Simulation

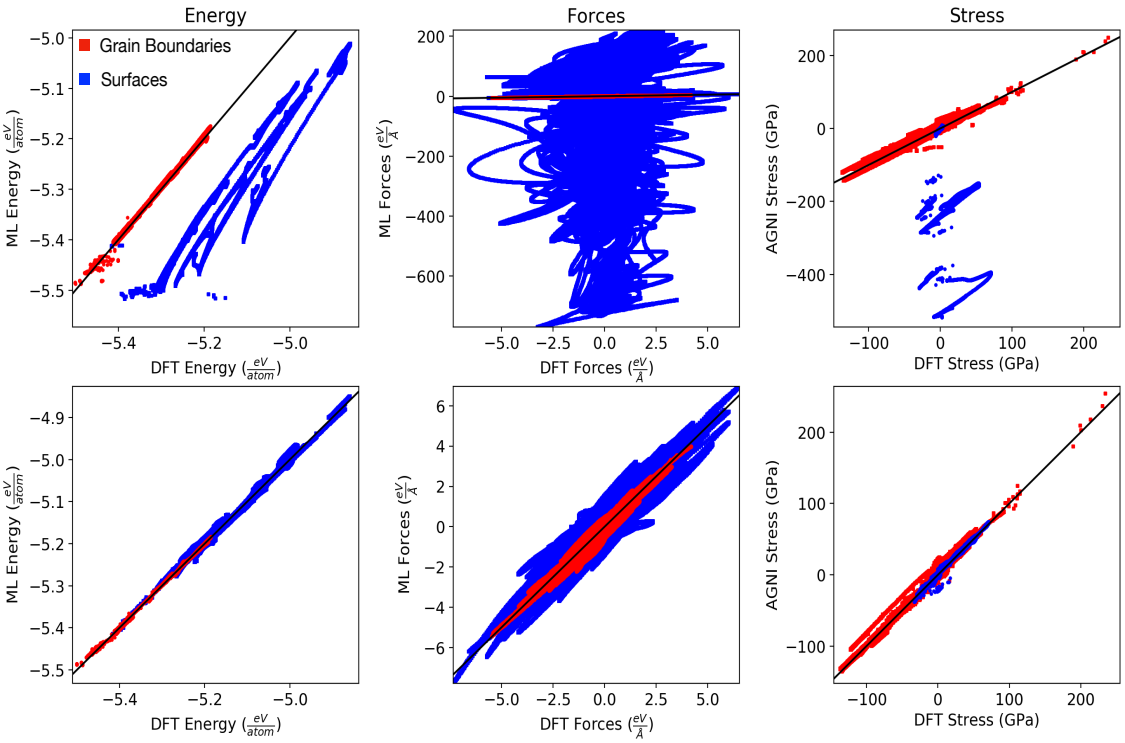

Figure 4.2: Parity plots of the energy, forces, and stresses, predicted on the total set of grain boundary (red) and surface (blue) reference data before (top) and after (bottom) the ML-AGNI models iterative improvement procedure.

Environment (ASE) [257]. Geometry optimizations were performed using both VASP (for DFT) LAMMPS (for EAM and ML-AGNI). NEB calculations, along with the climbing image formalism [186], were employed to determine the minimum energy pathway of diffusion profiles. NEB calculations were performed using both LAMMPS (ML-AGNI-AGNI and EAM), as well as VASP (DFT).

Geometry optimizations were used to gather information such as the grain boundary energy, surface energy, work of separation energy, vacancy formation energy for in-plane vacancies of grain boundaries, and the relaxed structure of both edge and screw dislocations. In this work, grain boundary energy was calculated as:

$$\gamma_{GB} = \frac{E_{GB} - n_{GB}E_0}{2A_{GB}} \tag{4.1}$$

with n_{GB} being the number of atoms in the grain boundary structure, A_{GB} being the

area of the grain boundary plane, and E_0 being the cohesive energy. The surface energy was calculated using the same formula, substituting n_{GB} for n_{Surf}, and A_{GB} for A_{Surf}. A factor of 2 is used in both cases to account for the double counting of energy that occurs from periodicity. The work of separation energy was calculated as:

$$W_{sep} = 2\gamma_{Surf} - \gamma_{GB} \tag{4.2}$$

The grain grain boundary vacancy formation energy, both with respect to a bulk configuration, as well as a pristine grain boundary environment was also calculated. In both cases, the vacancy was placed at the center of the boundary plane. For boundaries that space multiple layers, the vacancy was placed as close to the midpoint (normal to the boundary) as possible. The vacancy formation energy, with respect to bulk was calculated as:

$$E_{vac} = E_{GB+vac} - n_{GB+vac}E_0 \tag{4.3}$$

with n_{GB+vac} being the number of atoms in the grain boundary structure containing a single vacancy, and E_{GB+vac} is the corresponding energy of the structure. When using the pristine grain boundary as the reference, the equation (10) is used, but E_0 is substituted for E_{GB}, where E_{GB} is the energy of the grain boundary system without a vacancy, and is given in $\frac{eV}{atom}$,.

Adsorption energies for both a single adatom, as well as a dimer, were calculated on the Pt (111), (110), and (100) surfaces, using an 80, 144, 180-atom slabs respectively. The binding energy and a dimer on each of these surfaces was also calculated. The adsorption energy was calculated as:

$$E_{ads} = -\frac{1}{N}(E_{slab+adsorbate} - (E_{slab} + NE_{atom})) \tag{4.4}$$

N is defined as the number of adsorbates in the system. $E_{slab+adsorbate}$ is defined as the energy of the slab with the adsorbate bonded to the surface, E_{slab} is the energy of just

the slab (no adsorbate), and E_{atom} is the energy of a single adsorbate atom in a box. The binding energy of a dimer is also defined as:

$$E_{bind} = E_{separate} - E_{together} \tag{4.5}$$

where $E_{separate}$ is defined as the en energy of a system containing a slab with the two atoms in the dimer placed as far away from each other as possible. $E_{together}$ is defined as the energy of the slab with the dimer bonded to the surface, and is equivalent to $E_{slab+adsorbate}$ for the case of the dimer.

In all scenarios, both the ionic positions and the cell volume were allowed to change. Electronic convergence terminated at an energy difference of 10^{-4} eV, and ionic relaxations were considered converged at an energy difference of 10^{-2} eV, for all calculations.

NEB calculations were used to study the diffusion of a single vacancy both along, and away from, the boundary plane, of the $\sum 3[111](111)$ grain boundary, as well as the activation energies of several adatom diffusion mechanisms on the (111), (110), and (100) surfaces. In all scenarios, both the ionic positions and the cell volume were allowed to change. Electronic convergence terminated at an energy difference of 10^{-4} eV, and ionic relaxations were considered converged at an energy difference of 10^{-2} eV, for all calculations.

MD simulations were used to capture both the tensile and shear strains of single crystal FCC Platinum. Simulations were performed for a temperature range of 100K to 1000K. Temperatures above 1000K were not considered, as reliable experimental values do not exist in this regime. Simulations at temperatures lower than 100K were also not considered in this work, as it has been shown that zero-point energy contributions become non-negligible below 100K for Platinum [258, 259]. As the simulations considered in this work are classical in nature, and do not consider quantum effects, temperatures below 100K cannot be reliably predicted.

For the case of tensile strain, a 21x21x21 supercell containing 37,044 atoms is used.

NPT simulations, run for 2 ns at $P = 0$, are used to equilibrate the supercell volume at a given temperature. Then, NVT simulations are performed, in which the cell was strained along the X axis at a rate of $10^{-3}\frac{1}{ps}$ for 10 ns. As the strain along the Y and Z axis remains constant at 0, the elastic constants can be calculated from the stress-strain relationships defined by $\sigma_{xx} = C_{11}e_{xx} + C_{12}(e_{yy} + e_{zz})$ and $\sigma_{yy} = C_{11}e_{yy} + C_{12}(e_{xx} + e_{zz})$, where C_{ij} is a given elastic constant, σ_{ii} is the stress along the ii direction, and e_{ii} is the strain along the ii direction.

For the case of shear strain, the same supercell and simulation arrangement employed during the tensile strain test was used. However, due to the stress-strain relationship, defined by $\sigma_{xy} = C_{44}e_{xy}$, the initial supercell was defined with tilt factors, initially set to 0. After an equilibration run, as defined previously, the cell was deformed along both the X and Y axis, uniformly, at a rate of $10^{-3}\frac{1}{ps}$ for 10 ns. For both tensile and shear strains, the stress was plotted against the strain, for a given elastic constant. A linear regression curve was then fit to the stress-strain relationship, whose slope is the corresponding elastic constant. An R^2 fit of 0.95, as a minimum, was used to determine a line's convergence, before extracting the elastic constants. The bulk, shear, and Young's modulus was then calculated from the predicted elastic constants using the Voigt-Reuss-Hill approximation [260].

MD simulations were performed for properties such as the coefficient of linear expansion, and the change in lattice parameter as a function of temperature. A 25x25x25 supercell, containing 62,500 atoms, was used. NPT simulations, run for 10ns, were performed for temperatures between 100K and 2000K. The final lattice parameter was carefully chosen only after a strict convergence criteria of 10^{-3}Å was met. For the calculation of the coefficient of linear expansion, the reference temperature was set at 300K to compare with experimental values.

MD simulations, were also performed to study how grain sizes are affected by temperature. A 51x51x51 supercell containing 508,971 atoms was used. The initial distribution of grains was created using the voronoi tessellation package in Atomsk [261]. NPT sim-

ulations, run for 1 ns at $P = 0$, were used to equilibrate the supercell volume at a given temperature. Simulations were performed between T=300K and T=700K, to align with experimental results [262]. Previous computational work indicates that 1 ns is sufficient to allow for an equillibration among grain sizes at the temperatures and system size considered in this work [263, 264].

4.3 Capturing multi-scale phenomena in single-crystal bulk Platinum

4.3.1 Understanding bulk thermodynamic properties

The three generated ML-AGNI models were used to reproduce several thermodynamic quantities, shown in Table 4.4. We begin this discussion by looking at the predictions made by the ML-AGNI-energy model. The cohesive energy (E_0), equilibrium volume (V_0), and bulk modulus (B) were all obtained by fitting the Birch-Murnaghan equation of state [265] (EOS) to energies corresponding to volumes between 14 and 17 Å^3. The cohesive energy and the equilibrium volume were also obtained from a geometry optimization.

Table 4.4: Thermodynamic properties of Pt, calculated using either the ML-AGNI energy or stress models, and DFT. * represents the Birch-Murnaghan EOS [265], where ‡ represents the Voigt-Reuss-Hill approximation [260], and $^\wp$ represents a geometry optimization. The values in brackets for the shear and Young's modulus represent the calculated lower and upper bounds. For DFT's calculation of the elastic coefficients, two values are reported using different methods: (1) Energy as a function of strain, and (2) Stress as a function of strain (in brackets). Please see text for details on the prescription used to calculate the elastic constants.

Property	DFT	ML-AGNI-Energy	ML-AGNI-Stress
E_0 (eV/atom)	-6.05*, -6.05$^\wp$	-6.05*, -6.05$^\wp$	-
V_0 (Å^3 / atom)	15.68*,15.73$^\wp$	15.69*,15.74$^\wp$	-
B (GPa)	265.62*, 227.39‡	265.95*, 239.86‡	234.39‡
G (GPa)	[76.51‡, 77.08‡]	[80.91‡, 81.48‡]	[76.22‡, 76.85‡]
E (GPa)	[206.38‡, 207.76‡]	[218.19‡, 219.57‡]	[206.29‡, 207.83‡]
C_{11} (GPa)	341.12 (341.36)	359.83	348.46
C_{12} (GPa)	170.53 (179.07)	179.88	177.36
C_{44} (GPa)	71.61 (65.32)	75.83	71.06
E_{1f} (eV)	0.65	0.55	-
E_{2b} (eV)	-0.18	-0.15	-

The bulk modulus, along with upper and lower bounds for the shear modulus (G), as well as the Young's modulus (E), can also be calculated via the Voigt-Reuss-Hill approximation [260]. Employing both the Birch-Murnaghan EOS and the Voigt-Reuss-Hill approximation allows one to compare the agreement between the ML-AGNI energy and stress values. The elastic constants C_{11}, C_{44}, and C_{12} were calculated according to a prescription described by Ding et al [266]. Figure 4.3 shows energy and stress as a function of strain for the several types of strain used in this work.

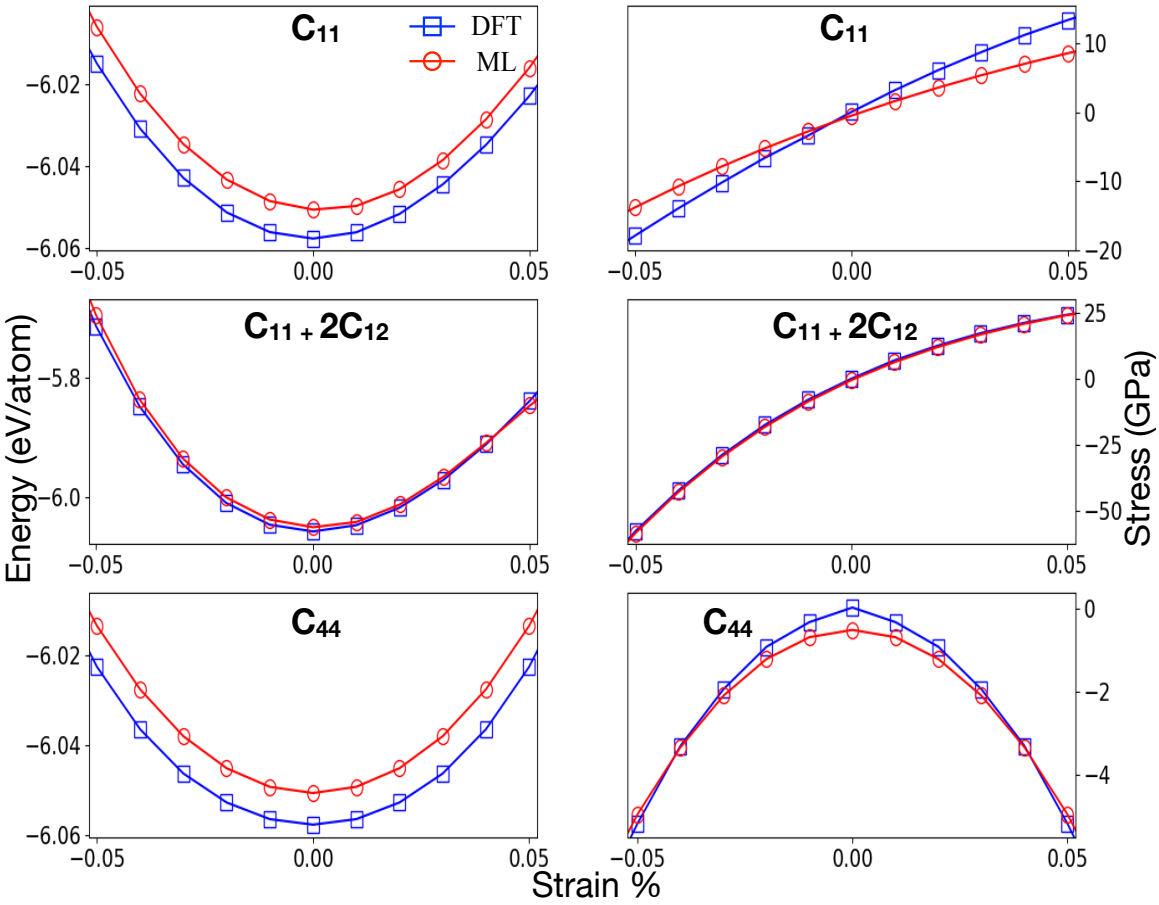

Figure 4.3: Comparison of different elastic constants as computed using DFT and ML-AGNI models, as derived using the energy vs strain trends (first column) and stress vs strain trends (second column). Please see text for more details.

The elastic properties mentioned above can also be calculated with the ML-AGNI-stress model, shown in Figure 4.3 (right). For the case of the bulk, shear, and Young's modulus, the Voigt-Reuss-Hill approximation was used, as this ML-AGNI model only has

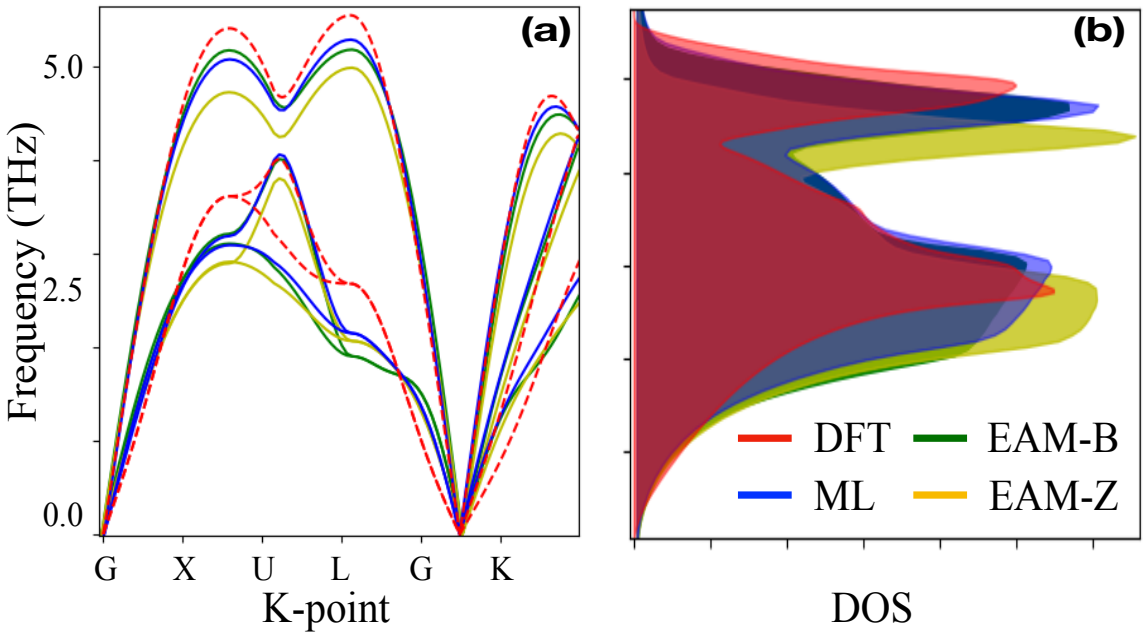

Figure 4.4: (a) Phonon band structure, (b) vibrational density of states,ML-AGNI force model (blue), EAM-Z and EAM-B (green, yellow), and DFT (red). The phonon band structure and DOS were computed using the finite atomic displacement method.

access to stress. The elastic constants were calculated according to $\sigma_{ii} = C_{ii}\varepsilon_{ii}$, where σ_{ii} is the stress. The agreement across multiple, unique approximation methods can be seen between not only the ML-AGNI-energy and ML-AGNI-stress models, but also between the ML-AGNI-stress model and DFT. This agreement shows that both models can be used interchangeably to reliably make predictions of a material's mechanical properties.

We then shift our focus to the ML-AGNI-force model. The vibrational density of states (VDOS) as well the phonon band structure, which have to be properly represented to allow for the prediction of thermodynamic quantities such as thermal expansion, heat capacity, etc, are used to determine the ML-AGNI force model's capability of capturing small atomic perturbations. Figure 4.4(a) shows the phonon band structure, calculated via the finite displacement method [267] and Figure 4.4(b) shows the corresponding VDOS. The ML-AGNI-force model shows good agreement to DFT for predicting the acoustic modes of the phonon band structure, indicating that under small atomic perturbations (as opposed to the much larger displacements often encountered during dynamic trajectories), the fidelity of

the force model is maintained. This also implies that any properties one desires to extract from the phonon frequencies, e,g,. heat capacity, vibrational density of states, etc, can be reliably obtained as well.

For the case of the single vacancy formation energy (E_{1f}), and the divacancy binding energy (E_{2b}), both the ML-AGNI force and energy models were employed. The divacancy binding energy is calculated as the difference in energy between the two vacancies adjacent to one another, and the two vacancies being separated by several intermediate sites. For this, two vacancies were placed next to each other, and NEB calculations were performed (which will be explained in detail in later sections), allowing for one of the vacancies to move away from the other. At some distance away, each vacancy effectively acts as a single vacancy, and no longer feels the effect of the other. Forces and energies, calculated by each of their respective ML-AGNI models, were used to relax the corresponding structures.

4.3.2 Exploring the potential energy surface

The ML-AGNI model's ability to extrapolate during dynamic conditions gives rise to another question: can the ML-AGNI models accurately predict the kinetics of specific atomistic processes with the accuracy of QM? A straightforward approach to answer this question is to perform an ionic relaxation starting from a highly disordered state. To this end, we employ the ML-AGNI-force and ML-AGNI-energy models to perform ionic relaxations on highly disordered systems, starting from initial configurations of: (1) defect-free bulk, and (2) bulk with a single vacancy in a 7x7x7 supercell. Random displacements on these configurations of up to 0.5 Å, in each of the x, y, and z cartesian directions, were used. Each relaxation was terminated when an accuracy of 10^{-7} eV and 10^{-2} eV/Å, for energies and forces respectively, was reached. Several runs were performed with varying random displacement seeds to ensure the fidelity of the model under different disordered configurations. Both scenarios show excellent agreement with their respective equilibrium geometries. A visual representation of these relaxations can be found in Figure 4.5.

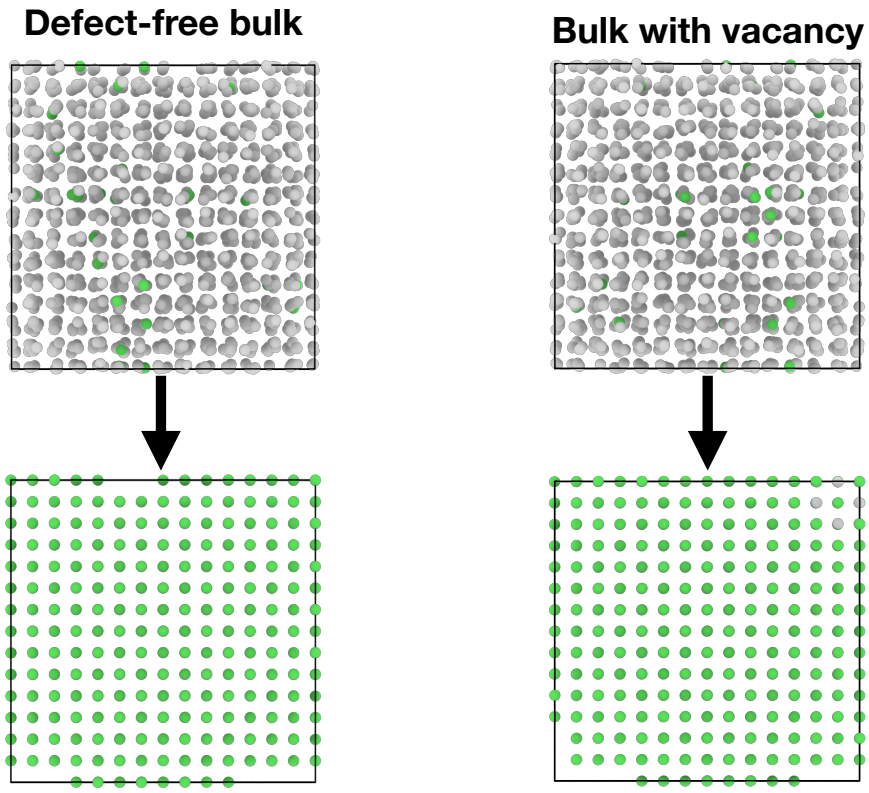

Figure 4.5: The before (top) and after (bottom) atomic configurations, of defect-free bulk (left) and bulk with a single vacancy (right), simulated via a conjugate-gradient geometry optimization. Colors correspond to an atom's coordination, with white representing an unknown coordination (highly asymmetric), and green representing FCC coordination.

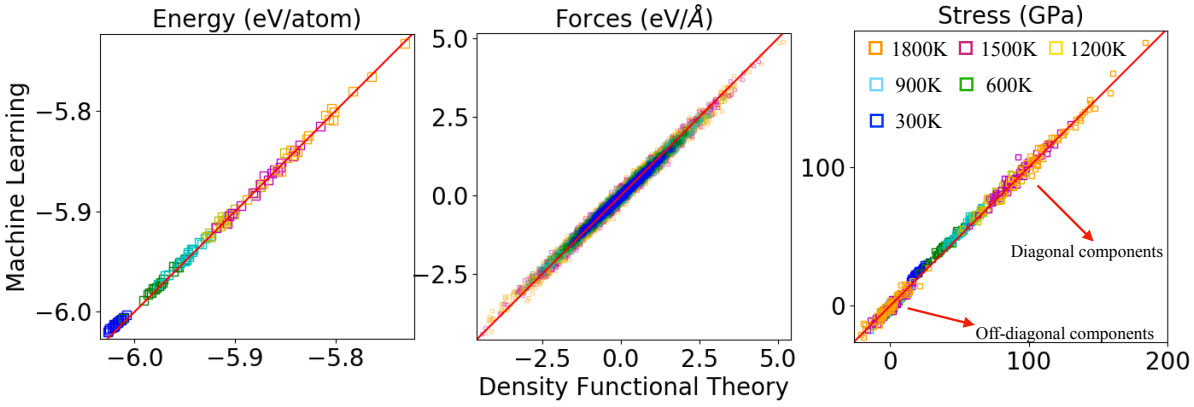

Figure 4.6: ML-AGNI model predictions, compared against DFT for (a) force, (b) stress, (c) energy. Structures were gathered from trajectories of defect-free bulk Pt at different temperatures, generated during MD using the ML-AGNI-force model. It should be noted that the configurations encountered during these MD simulations are not explicitly present in the model's training set. Colors correspond to the different temperatures used.

The ML-AGNI model's performance during dynamic conditions is of great importance, as the complex materials phenomena that we aim to capture occur under these conditions. To this end, we consider MD simulations of a 256-atom bulk configuration. Canonical ensemble MD was performed at several temperatures between 300 and 1800K. A timestep of 0.5 fs was chosen for the runs with a total simulation time of 10ns. Single-step DFT calculations were also performed on several snapshots, randomly chosen from each trajectory to verify the accuracy of the models. Parity plots comparing the forces, stresses, and energies, predicted by both DFT and each corresponding ML-AGNI model, on these snapshots are shown in Figure 4.6. The excellent agreement between the ML-AGNI models and DFT, indicates that all three ML-AGNI models can make accurate predictions within configuration spaces not explicitly employed in their respective training sets.

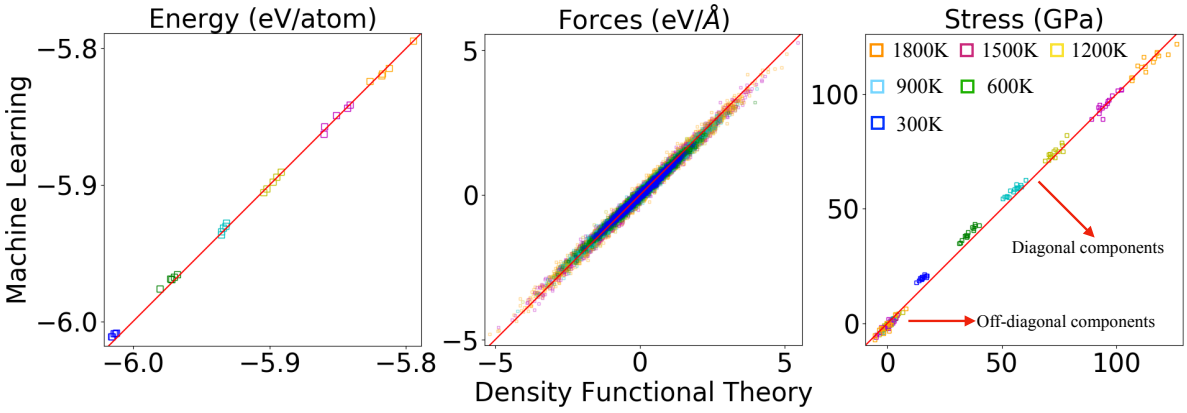

Figure 4.7: ML-AGNI model predictions, compared against DFT for (a) force, (b) stress, (c) energy. Structures were gathered from trajectories of bulk Pt with a single vacancy, at different temperatures, generated during MD using the ML-AGNI-force model. It should be noted that the configurations encountered during these MD simulations are not explicitly present in the model's training set. Colors correspond to the different temperatures used.

Next, we consider MD simulations of a 256-atom bulk configuration containing a single vacancy (a total of 255 atoms). Canonical ensemble MD was performed at several temperatures between 300 and 1800K, shown in Figure 4.7. A timestep of 0.5 fs was chosen for the runs with a total simulation time of 10ns. Single-step DFT calculations were also performed on several snapshots, randomly chosen from each trajectory to verify the

accuracy of the models. Parity plots comparing the forces, stresses, and energies, predicted by both DFT and each corresponding ML-AGNI model, on these snapshots are shown in Figure 4.7. The excellent agreement between the ML-AGNI models and DFT, indicates that all three ML-AGNI models can make accurate predictions within configuration spaces not explicitly employed in their respective training sets.

4.3.3 Capturing the kinetics of vacancy diffusion in bulk

Next, we consider the pathway of a single vacancy hopping from one site to a nearest-neighbor site in a bulk fcc configuration. NEB calculations, performed with the ML-AGNI energy and force models (as well as all three EAM potentials and DFT), along with the climbing image formalism, were used to determine the minimum energy pathway (MEP) of the hop. Figure 4.8(left) shows the MEP predicted by ML-AGNI as well as DFT. For the case of ML-AGNI, the diffusion barrier was predicted to be 1.20 eV, which is in excellent agreement with the calculated DFT value of 1.19 eV. EAM-B, EAM-F, and EAM-Z predict barrier heights of 0.83, 0.81, and 0.54 eV respectively. Experimental values vary depending on vacancy concentration and quench rates[268, 269, 270], however, the values reported are typically between 1.0 and 1.4 eV. Many factors can contribute to the accuracy of the calculated DFT barrier, including the treatment of surface effects around the vacancy [271], as well as the cell size's possible restriction of relaxations [272]. However, one should be reminded that the ML-AGNI models can only be as accurate as the reference data used to train them, and therefore should only be compared to the DFT value, and not experimental values.

The activation energy predicted by the NEB calculations can also be determined through dynamic simulations. In this case, MD runs were performed on a 7x7x7 supercell containing 1371 atoms and a vacancy, between 1000K and 2000K, using the ML-AGNI-force model to drive the dynamics. Simulations were run for a minimum of 1ns (with a time step of 0.5 fs), but were extended for lower temperatures to ensure statistical diversity with

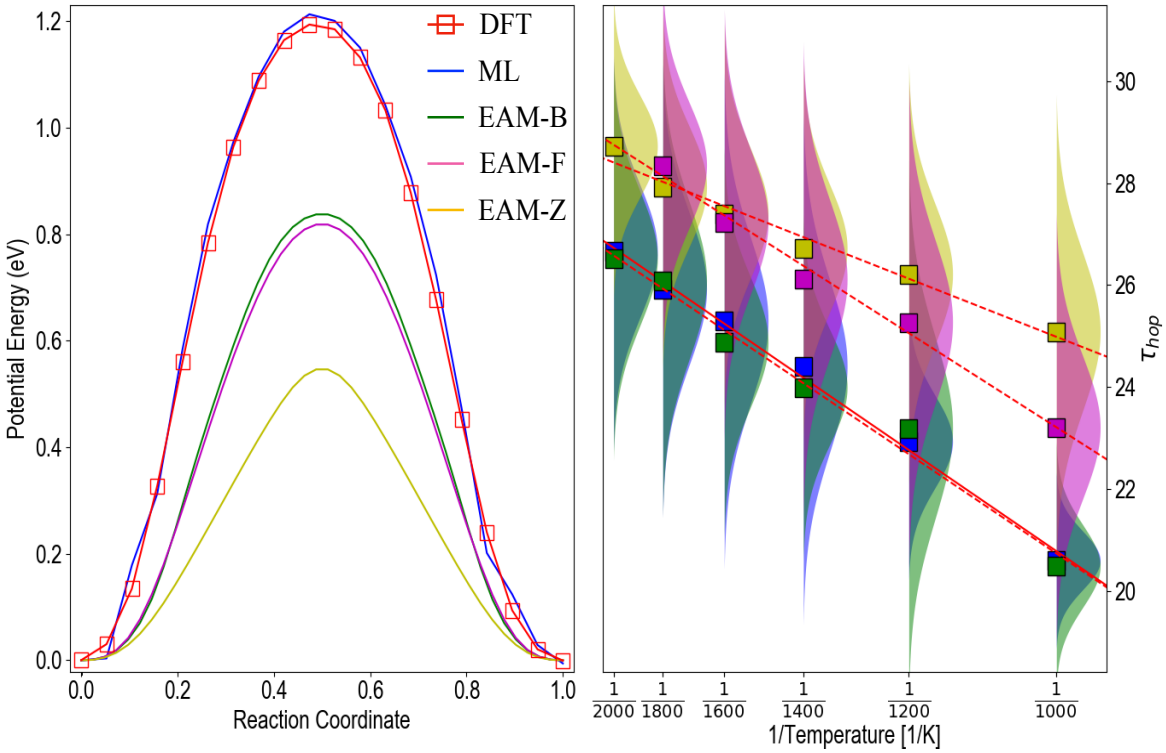

Figure 4.8: (left) Nudged elastic band prediction of a single vacancy migrating in bulk Pt. (right) Arrhenius plots for a single vacancy migrating in bulk Pt, generated from all methods used in this work. For each temperature, the MD simulation time was extended so as to allow at least 25 hopping events (thus allowing estimation of an average hop rate, and the corresponding distribution. A linear fit (red lines) was used to determine the dynamic activation energy (Ea).

regards to the hop rates. By observing the dynamics of the vacancy, the average rate constant (k) for the diffusion process was calculated. k is represented as $\frac{1}{t_{hop}}$, where t_{hop} is the average time taken for a vacancy to migrate from one arbitrary site to an adjacent site. A minimum of 25 hops were recorded at each temperature to ensure that t_{hop} was not dominated by events 2σ or greater away from the mean. Figure 4.8(right) shows an Arrhenius plot of k versus the the reciprocal temperature.

The ML-AGNI force model predicts an activation energy of 0.94 eV. As one cannot obtain a dynamic activation energy from DFT, the value of 1.19 eV, determined from the 0K NEB calculation described earlier, is used and agrees well with the dynamic ML-AGNI result. While the predicted ML-AGNI barrier is slightly lower, when compared to the

NEB barriers (for both ML-AGNI and DFT), one can expect that the activation energy obtained through MD will be lower than that obtained through NEB calculations, as such a methodology neglects any entropic effects that may help to "soften" the barrier [273, 274]. EAM-B, EAM-F, and EAM-Z predict activation energies of 0.96, 0.94, and 0.63 eV respectively, and is in good agreement with their respective NEB energy barriers, indicating little difference between the static and dynamic cases.

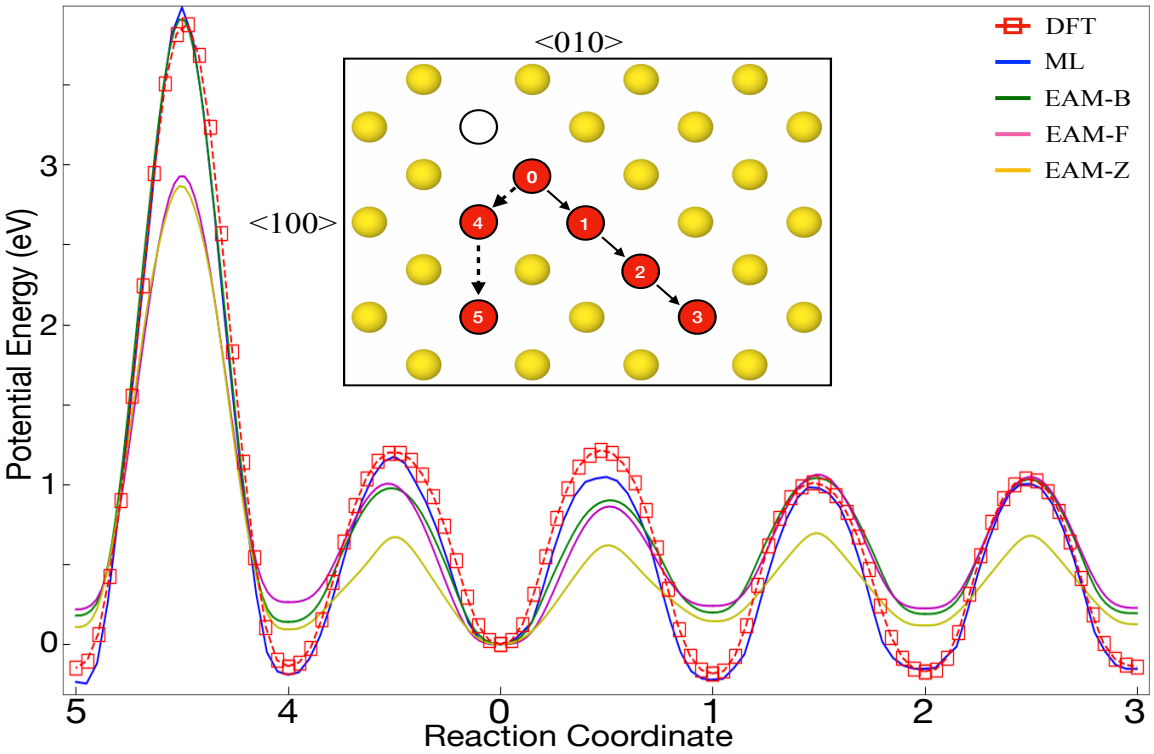

Figure 4.9: Nudged elastic band prediction of divacancy migration in bulk Pt. Reaction coordinates correspond to different positions of one vacancy as it moves away from its divacancy pair. As the pathway traverses from (0,1,2,3), one vacancy moves along the <110> direction away from the other vacancy. As the pathway moves from (0,4,5), one vacancy first moves along a <110> vector away from the other vacancy. After one hop along <110>, it then moves along a <100> vector away from the other vacancy. In all scenarios the first vacancy remains stationary. The inserted diagram outlines this procedure, where the white outlined circle represents the stationary vacancy, and light-red circles represent the different end-points of the second vacancy as it moves along each diffusion pathway (numbers in the inserted diagram correspond to the reaction coordinate values along the x-axis of the main plot). All energies plotted refer to the configuration at reaction coordinate 0 as the reference.

How vacancies interact with one another is also of importance. Here we consider the

diffusion/dissociation of a divacancy pair through NEB calculations, using the ML-AGNI force and energy models, along several possible diffusion pathways. For this, a 4x4x4 FCC supercell containing 254 atoms and a divacancy was considered. Figure 4.9 highlights two possible pathways that can occur during dissociation. From these minimum energy pathways (MEP) we can conclude several important pieces of information. The first pertains to the relative thermodynamic stability of the divacancy versus two isolated vacancies. Both ML-AGNI and DFT predict the divacancy configuration to be higher in energy than that of two isolated vacancies, (this can be seen by observing the difference in energy between the reaction coordinates 0 and 3, as well as 0 and 5, in Figure 4.9). The second belongs to the kinetics of the dissociation/diffusion process. When travelling along the $<110>$ direction (from reaction coordinate 0 to 3), the barrier heights between each reaction coordinate remain consistent, with a decrease in energy of the final configuration (as mentioned previously). However, due to the prohibitively large barrier height when travelling from reaction coordinate 4 to 5, one can make the assumption that, under dynamic conditions, diffusion should occur along the $<110>$ direction.

However, for all three EAM potentials considered in this work, the divacancy is predicted to be more energetically favorable than 2 isolated vacancies, regardless of the diffusion pathway that is chosen. The barrier heights are also predicted to be significantly lower than those calculated by both ML-AGNI and DFT, indicating a more diffuse solid. The differing profiles presented here paint vastly different pictures of vacancy behavior, at least at 0K. DFT and ML-AGNI do not seem to favor divacancy formation, indicating that energy must be provided to the system to allow vacancies to come together. All considered EAM potentials indicate the opposite, in that energy must be supplied to the system to favor vacancy separation. However, we must remind the reader that this picture exists at $T = 0K$, and how this portrayal changes at $T > 0K$ is yet to be fully understood computationally.

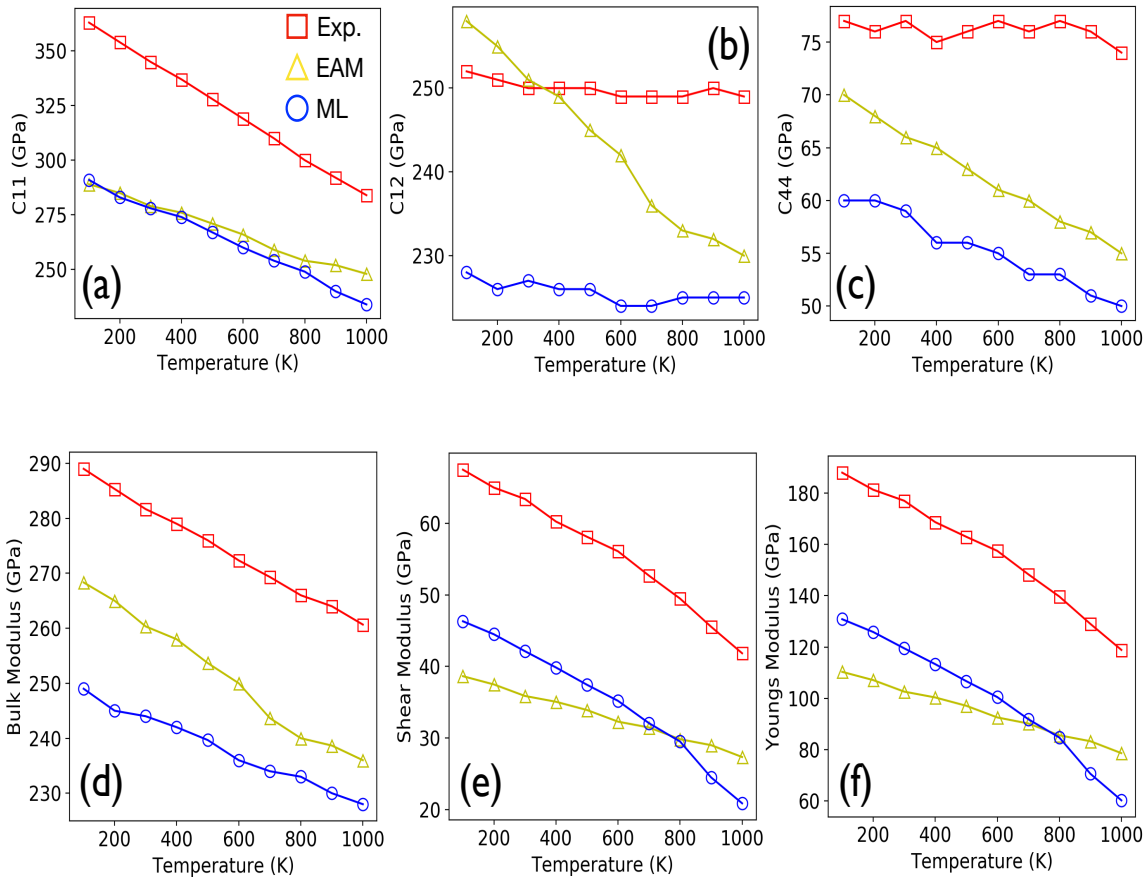

Figure 4.10: (Top) The elastic constants C_{11}, C_{12}, and C_{44}, (a-c) respectively, for our AGNI models (blue), an EAM potential (yellow), and experiments (red) are shown. While absolute values between computational methods and experiments will rarely agree explicitly, due to deviations between experiments and the reference data used to fit the computational models, the difference in slopes should be negligible in order to be considered in agreement with experiments. The AGNI models are the only computational method whose slopes agree quantitatively with experiments. (Bottom) The bulk, shear, and Young's modulus, (d-f) respectively, is shown for our AGNI models (blue), an EAM potential (yellow), and experiments (red). These values were calculated using the elastic constants using the Voigt-Reuss-Hill approximation [260]

4.3.4 Simulating the dynamic evolution of mechanical properties

The dynamic, temperature dependent behavior of the mechanical properties of Platinum was calculated via MD simulations. Figure 4.10 shows the change in the C_{11}, C_{12}, and C_{44} elastic constants as the temperature is increased from 100K to 1000K. Three sets of values are shown: (1) Experimental values [275, 253], (2) AGNI predictions, and (3) EAM predictions. The EAM values shown in Figure 4.10 were taken from previous studies [253]. While several EAM potentials were studied in previous works, only the most reliable potential's values are shown here. This EAM potential will henceforth be referred to as EAM-A, due to its primary author James Adams [276].

One important point that must be mentioned is the relative versus absolute nature of the properties discussed in the remainder of this article. As both ML-AGNI and semi-empirical potentials are fit to a set of reference data, one cannot always compare the absolute values of a predicted property to experimental values. For example, as shown in our previous work [172, 166], the absolute value of the 0K elastic constants will deviate significantly from experiments at low temperature. This discrepancy however, is not due to the model's failure, but rather the value that the model's reference level of theory predicts. In this case, the AGNI models are trained on reference DFT data, generated using the PBE exchange-correlation functional, which deviates from experiments significantly [277, 166, 278]. Therefore, AGNI cannot be expected to predict absolute property values equivalent to experiments, but will make predictions at the corresponding DFT level of theory. Due to these differences amongst various levels of theory, one cannot rely on absolute values, but rather the quantitative, and qualitative, trends that the models yield with respect to experiments.

With this in mind, we begin by looking at several important trends that can be observed from the C_{11}, C_{12}, and C_{44} elastic constants as the temperature is increased from 100K to 1000K. Figure 4.10 shows a visual manifestation of these trends, while Table 4.5 provides the absolute values. Experimentally, C_{11} has been shown to decrease by approximately

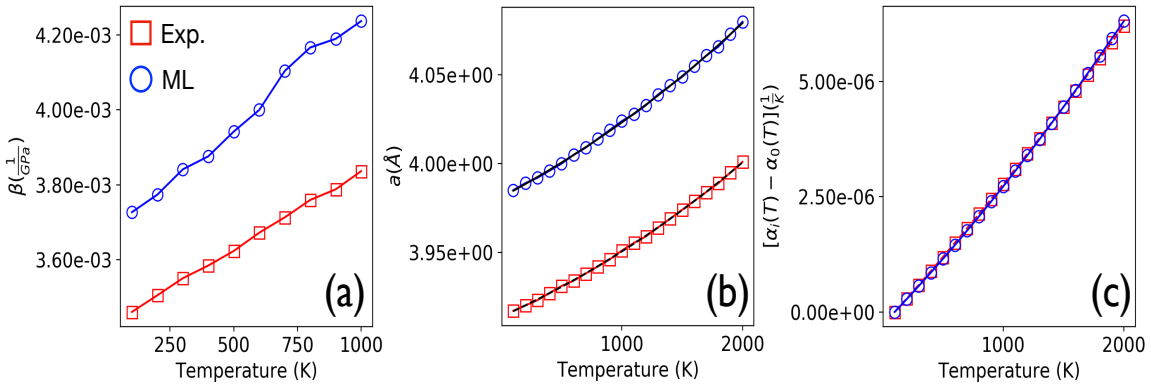

Figure 4.11: The coefficient of isothermal compressability, change in lattice parameter, and coefficient of linear expansion, (a-c) respectively, is shown for our AGNI models (blue),and experiments (red). Lattice parameter values (b) are used to fit a cubic spline (shown in black). Linear expansion values (c) are then calculated from the derivative of the cubic spline.

22% between 100K and 1000K, while EAM-A predicts a thermal degradation of (14%), and the AGNI framework a degradation of (20%). Contrary to C_{11}, however, both C_{12}, and C_{44} show little to no thermal degradation experimentally, (1%) and (4%) respectively. However, EAM-A shows significant thermal degradation with respect to experiments in both C_{12} (11%), and C_{44} (21%). The AGNI framework performs substantially better than EAM-A, yielding degradation of (1%) and (16%) , for C_{12}, and C_{44} respectively. While AGNI's predicted change in C_{11} and C_{12} between is nearly identical when compared to experiments, thermal degradation in C_{44} is still 4 times that of experiments; though EAM-A yields a degradation greater than 5 times that of experiments.

Understanding how a material will respond to various forms of stress is critically important for a variety of applications [253, 279, 280, 266]. To this end, the dynamic behavior of the bulk, shear, and Young's modulus can be calculated from the predicted elastic constants using the Voigt-Reuss-Hill approximation [260]. Figure 4.10, and Table 4.5 show the change in these properties as the temperature is increased from 100K to 1000K. Experimental predictions of the bulk modulus indicate a thermal degradation of (10%), compared to a degradation of (12%) and (8%) for EAM-A and AGNI respectively. Therefore, one can

Table 4.5: Absolute values for the properties predicted in this work. δ represents the percent difference between the property values at 100K vs 1000K. $\frac{dX}{dT}$ represents the slope of a given property as a function of temperature.

Property	Experiments	EAM-A	AGNI
δC_{11} (%)	22	14	20
δC_{12} (%)	1	11	1
δC_{44} (%)	4	21	16
δB (%)	10	12	8
$\frac{dB}{dT}(\frac{GPa}{K})$	-0.03	-0.04	-0.02
$\delta \mu$ (%)	39	29	54
$\frac{d\mu}{dT}(\frac{GPa}{K})$	-0.03	-0.01	-0.03
δE (%)	37	29	53
$\frac{dE}{dT}(\frac{GPa}{K})$	-0.07	-0.03	-0.07
$\frac{d\beta}{dT}(\frac{1}{GPaK})$	$4.17\text{x}10^{-7}$	$5.67\text{x}10^{-7}$	$4.11\text{x}10^{-7}$
$\frac{da}{dT}(\frac{\text{Å}}{K})$	$9.33\text{x}10^{-5}$	–	$1.16\text{x}10^{-4}$

argue that both EAM and AGNI will perform equally well in understanding the resistance to compression. For the shear modulus, experimental values indicate a thermal loss of (39%), compared to a degradation of (29%) and (54%) for EAM-A and AGNI respectively. Finally, for Young's modulus, experimental values indicate a decrease of (37%), compared to a decrease of (29%) and (53%) for EAM-A and AGNI respectively. From these metrics, both AGNI and EAM show moderate deviations, when compared to experiments, when understanding the response to both linear and shear stresses.

However, If we assume that the change of these properties is perfectly linear between 100K and 1000K, we can easily calculate their slopes, shown in Table 4.5, which will provide the rate in which these properties change as a function of temperature. For the case of the bulk modulus, we arrive at slopes of -0.03 $\frac{GPa}{K}$, -0.04 $\frac{GPa}{K}$, and -0.02 $\frac{GPa}{K}$ for experiments, EAM-A, and AGNI respectively. For the shear modulus, we obtain slopes of -0.03 $\frac{GPa}{K}$, -0.01 $\frac{GPa}{K}$, and -0.03 $\frac{GPa}{K}$ for experiments, EAM-A, and AGNI respectively. Finally, for Young's modulus, we calculate slopes of -0.07 $\frac{GPa}{K}$, -0.03 $\frac{GPa}{K}$, and -0.07 $\frac{GPa}{K}$

for experiments, EAM-A, and AGNI respectively. Therefore, while EAM-A and AGNI's prediction yield moderate errors when one considers only the absolute thermal degradation over the entire temperature range, the slopes of these relationships tell a different story, where AGNI outperforms EAM-A significantly.

Another important aspect of the dynamic mechanical response of Platinum that must be well understood is the physical change in the supercell as a function of temperature. To this end we present calculations for the lattice parameter, coefficient of isothermal compressibility, and coefficient of linear expansion, shown in Figure 4.11 and Table 4.5. In a bulk material, the coefficient of isothermal compressibility can be represented as the inverse of the bulk modulus [281], and can be thought of as the relative volume change that will occur in response to an applied stress. From Figure 2 one can see good agreement between the ML-AGNI models and experiments. As described previously, the rate of change in the isothermal compressibility can be calculated by assuming a linear rate of change. Experiments predict a rate of change of $4.17\text{x}10^{-7}$ $\frac{1}{GPaK}$, while EAM-A and AGNI yield rates of $5.67\text{x}10^{-7}$ $\frac{1}{GPaK}$ and $4.11\text{x}10^{-7}$ $\frac{1}{GPaK}$ respectively.

Figure 4.11 also provides information about change in lattice parameter as a function of temperature. As can be seen in Figure 4.11b, AGNI and experimental values of the change in lattice parameter as a function of temperature, show exceptional agreement between over the entire temperature range. Small deviations close to the melting temperature can be explained from the results obtained in our previous work [166]. As before, if we take the slope of this curve, information about the rate of change in lattice parameter as a function of temperature can be calculated. Experiments indicate a rate of change of $9.33\text{x}10^{-5}$ $\frac{\text{Å}}{K}$, while AGNI predicts a rate of $1.16\text{x}10^{-4}$ $\frac{\text{Å}}{K}$ respectively.

Finally, the information encoded in the change in lattice parameter can be used to calculate the coefficient of linear expansion as a function of temperature [282]. A cubic spline is fit to the lattice parameter values, shown in black in Figure 4.11b. The derivative of this spline is then used to calculate the coefficient of linear expansion, shown in Figure 4.11c.

As the difference in lattice parameter between experiments and PBE creates an artificial shift in the coefficient of linear expansion, the values in Figure 4.11c are referenced to the value at 100K for both AGNI and experiments. As there are small deviations in the lattice parameter at high temperatures, errors in the coefficient of linear expansion, at these same temperatures, are to be expected. Even with small discrepancies near the melting temperature, the agreement between AGNI and experiments can clearly be seen.

4.4 Multi-scale defect behavior of polycrystalline platinum

4.4.1 Predicting the atomic structure of edge and screw dislocations

Edge and screw dislocations play a crucial role in the plasticity and fracture of metals [283, 284, 285, 286]. Therefore, accurately predicting the geometry of dislocation lines is of paramount importance. To this end, we have studied the $\frac{1}{2}[110]$ edge and screw dislocation. As Pt is an fcc metal, the most favorable slip system is $\frac{1}{2} < 110 > 111$ [287], We employ the dislocation extraction algorithm [288] (DXA) to determine the geometric information around the dislocation core. Using a 1x1x3 supercell of the relaxed dislocation system (due to the requirements of the DXA algorithm, and the reduction in the z-direction required for the system sizes needed to perform a DFT relaxation), the dislocation type, dislocation line length, and the dislocation's Burgers vector were determined.

When considering the edge dislocation, upon relaxation, the dislocation type determined by the DXA analysis was $\frac{1}{2} < 110 >$ for all levels-of-theory used in this work. The dislocation line length was calculated as 14.61 Åfor DFT, and 14.61 Å, 14.22 Å, 13.89 Å, and 13.91 Åfor ML-AGNI, EAM-B, EAM-F, and MEA-Z respectively. The Burgers vector for all models was calculated as $\frac{1}{2}[0\bar{1}\bar{1}]$. Upon relaxation, the initial dislocation core split into two cores, that migrated away from each other along the dislocation's Burgers vector. The final core centers were located 9.31 Åapart for DFT and 9.11 Å, 15.03 Å, 18.05 Å, and 18.05 Åfor ML-AGNI, EAM-B, EAM-F, and MEA-Z respectively. The agreement between ML-AGNI and DFT can be seen in both the dislocation line length, as well as the

separation distance between dislocation cores. While the calculated dislocation line lengths for all EAM potentials will not necessarily agree with DFT, due to differences in the equilibrium lattice parameters, there does exist substantial disagreement in the core separation distance between the EAM models used in the work and DFT.

When considering the screw dislocation, upon relaxation, the dislocation type determined by the DXA analysis was $\frac{1}{2} < 110 >$ for all models use. The dislocation line length was calculated as 8.439 Åfor DFT, and 8.58 Å, 8.37 Å, 8.27 Å, and 8.28 Åfor ML-AGNI, EAM-B, EAM-F, and MEA-Z respectively. The Burgers vector for all models was calculated as $\frac{1}{2}[0\bar{1}\bar{1}]$. Unlike the edge dislocation, the initial screw dislocation core remained intact after relaxation for all levels-of-theory. While there is no discernible difference between ML-AGNI/EAM and DFT for the relaxed screw dislocation structure, there is a exists a substantial discrepancy between the relaxed EAM and DFT edge dislocation structure. This disparity is alleviated when using the ML-AGNI models, which show a near perfect agreement with DFT.

4.4.2 Understanding the behavior of clean surfaces

In this work we calculate properties of clean surfaces, such as the surface energy and the inter-layer relaxation difference for a variety of low-index surfaces. Figure 4.13b, and Table 4.6, show all surface energy calculations for ML-AGNI and the three EAM potentials with respect to the corresponding DFT prediction. Statistically, our ML-AGNI models have an root mean square error (RMSE) of 0.08 $\frac{J}{m^2}$ with respect to the DFT surface energies. EAM-B, EAM-Z, and EAM-F yield RMSE values of 0.10 $\frac{J}{m^2}$, 0.62 $\frac{J}{m^2}$, 0.05 $\frac{J}{m^2}$ respectively. Here, EAM-F performs slightly better than our ML-AGNI models, though both models perform equally well as the surface complexity increases.

The inter-layer relaxation difference, δd_{12} and δd_{23} was calculated for the (111), (110), and the (100) surfaces. Table 4.7 provides the calculated values, along with experimental predictions where they are available [289, 290]. For the (111) surface, δd_{12} is calculated as

Table 4.6: Properties of low-index Platinum surfaces. All energy values are given in units of eV, while d_{adatom} is shown in Å, and δd_{xy} is provided in %. All properties shown here are calculated using T=0K methods (optimizations or NEB).

Surface	DFT	ML-AGNI	EAM-B	EAM-F	EAM-Z
(111)	1.51	1.47	1.62	2.08	1.44
$(11\bar{2})$	1.68	1.79	1.82	2.37	1.69
(021)	1.89	1.92	1.91	2.50	1.87
(013)	1.89	2.02	1.90	2.46	1.83
$(2\bar{2}1)$	1.62	1.77	1.78	2.33	1.65
$(\bar{3}32)$	1.80	1.77	1.84	2.41	1.76
$(\bar{1}13)$	1.82	1.87	1.85	2.36	1.74
(230)	1.89	1.96	1.90	2.49	1.84
$(3\bar{3}\bar{4})$	1.61	1.65	1.75	2.26	1.58
$(1\bar{1}\bar{6})$	1.59	1.63	1.73	2.23	1.56
(340)	1.89	1.97	1.89	2.47	1.83

$+0.92\%$ for DFT, in good agreement with experiments, which indicate a positive relaxation difference. While our ML-AGNI models indicate a smaller percent change than both DFT and experiments, they do predict a positive inter-layer relaxation difference. This is in contrast to all EAM potentials, which predict a negative inter-layer relaxation difference. Experimental predictions indicate that there is no substantial difference between the second and third layers, though both DFT and ML-AGNI yield a small negative value for δd_{23}. However all EAM potentials predict a positive difference.

For the (110) surface, δd_{12} is calculated as -15.92% for DFT, in good agreement with experiments. Our ML-AGNI models again predict a value roughly half that of the DFT value, but correctly capture its negative nature. Among the EAM potentials, there exists a substantial spread, with EAM-F performing extremely well, EAM-Z performing comparably to our ML-AGNI models, and EAM-B showing significant deviation from both DFT and experiments. For δd_{23}, DFT deviates significantly from experiments, with DFT

Table 4.7: Properties of low-index Platinum surfaces. All energy values are given in units of eV, while d_{adatom} is shown in Å, and δd_{xy} is provided in %. All properties shown here are calculated using T=0K methods (optimizations or NEB).

Property	Exp	DFT	ML-AGNI	EAM-B	EAM-F	EAM-Z
(111)						
δd_{12}	+1.1 $\pm$ 0.5	+0.92	+0.24	-1.29	-4.11	-2.32
δd_{23}	0.0	-0.71	-0.54	+1.41	+1.27	+0.47
d_{adatom}		2.57	2.54	2.56	2.35	2.35
$E_{1,hop}$	0.26 $\pm$ 0.02	0.32	0.28	0.09	0.03	0.05
$E_{1,exc}$		1.70	1.75	1.70	0.82	1.90
$E_{1,ads}$		4.45	3.75	4.39	4.44	3.97
$E_{2,ads}$		4.61	3.89	4.62	4.90	4.37
$E_{2,bind}$		0.54	0.60	0.42	0.94	0.82
(110)						
δd_{12}	-18.0 $\pm$ 5.0	-15.92	-8.29	-3.37	-14.92	-8.76
δd_{23}	-10.0 $\pm$ 5.0	+8.53	+9.00	+3.09	+3.99	+3.36
d_{adatom}		2.64	2.74	2.68	2.54	2.59
$E_{1,hop}$	0.84 $\pm$ 0.1	1.10	0.70	0.21	0.23	0.23
$E_{1,exc}$	0.78 $\pm$ 0.1	0.91	0.81	0.50	0.41	0.24
$E_{1,ads}$		5.42	4.54	5.08	5.44	5.15
$E_{2,ads}$		5.53	4.66	5.25	5.63	5.41
$E_{2,bind}$		0.22	0.26	0.33	0.38	0.53
(100)						
δd_{12}	+0.2 $\pm$ 2.6	-2.46	-1.41	+0.03	-4.27	-4.25
δd_{23}		-0.80	-0.94	+2.32	+3.54	-0.54
d_{adatom}		2.63	2.70	2.61	2.40	2.47
$E_{1,hop}$		1.06	0.65	0.65	0.68	0.95
$E_{1,exc}$	0.47 $\pm$ 0.1	0.43	0.41	0.83	0.29	0.36
$E_{1,ads}$		5.22	4.08	4.75	5.06	4.45
$E_{2,ads}$		5.31	4.30	4.91	5.22	4.74
$E_{2,bind}$		0.20	0.13	0.34	0.47	0.56

predicting a positive inter-layer relaxation difference, and experiments indicating a negative difference. As our ML-AGNI models are trained on DFT data, they are expected to follow its trend. Our ML-AGNI models are in near perfect agreement with DFT, and all levels-of-theory indicate a positive δd_{23} occurs.

For the (100) surface, there is a significant spread among experiments regarding δd_{12}, with some predicting a positive difference, and others a negative difference. DFT, ML-AGNI, and EAM-B fall within the possible values, indicated by experiments, while both EAM-F and EAM-Z fall outside of the experimental spread. As no experimental values exist for δd_{23}, we can only compare our ML-AGNI models to DFT, which indicate good agreement. Both EAM-B and EAM-F deviate significantly from DFT, though EAM-Z is in good agreement, though we would like to emphasize that the true value is unknown.

4.4.3 Simulating the kinetics of surface adsorbates

In this section, we discuss the introduction of defects onto the (111), (110), and (100) surfaces. First we consider a single adatom on each surface. Upon relaxing each system, the adatom adsorption energy, and distance between adatom and surface atoms is calculated, and can be found in Table 4.7. Our ML-AGNI models, as well as all EAM potentials, agree well with DFT with regards to the bond distance, when considering the differences in equilibrium lattice parameter. However, our ML-AGNI models, while predicting the exact trend in adsorption energy with respect to DFT, yields values approximately 1eV lower than DFT. For all surfaces, there exists a spread among EAM values, but the trend in adsorption energy with respect to DFT is captured exactly.

The activation energy for adatom diffusion is also considered, calculated via the NEB method, and can be found in Table 4.7. For all surfaces, two mechanisms are considered: (1) hop, (2) two-atom exchange. For the (111) surface hop and exchange, our ML-AGNI models are in excellent agreement with both DFT and experiments [291, 292]. All EAM potentials significantly underestimate the hop mechanisms, but most perform well for the

exchange profile. For the (110) surface hop and exchange, our ML-AGNI models are again in excellent agreement with both DFT and experiments [293]. All EAM potentials significantly underestimate the activation energy of both mechanisms, with only EAM-B predicting a reasonable energy barrier for the exchange mechanism. For the (100) surface hop and exchange, our ML-AGNI models are once again in excellent agreement with both DFT and experiments [292]. The various EAM potentials fare slightly better here, though significant discrepancies exist for EAM-B's exchange, and EAM-Z's hop predictions.

We finally consider the adsorption and binding energies of a dimer on the (111), (110), and (100) surfaces, which can be found in Table 4.7. The DFT calculated energies are in good agreement with reported literature values [294], where available. Similarly to the adatom adsorption energy, our ML-AGNI models, while predicting the exact trend in the dimer adsorption energy with respect to DFT, yields values approximately 1eV lower than DFT. For all surfaces, there exists a spread among EAM predicted values, but, again, the trend in dimer adsorption energy with respect to DFT is captured correctly. Our ML-AGNI models predict the dimer binding energy, on all surfaces, to be in excellent agreement with the calculated DFT values. EAM-B performs well for all surfaces, while EAM-F deviates from DFT on both the (110) and (100) surfaces, and EAM-Z deviates significantly from DFT for all surfaces considered.

4.4.4 Predicting grain boundary energies

Accurately predicting properties, such as the grain boundary energy, surface energy, and work of separation energy, is an important step in simulating the complex behavior of material defect classes [295, 296, 297, 298, 299, 300]. Recent work has provided a simple prescription of the creation of grain boundary structures, as well as a list of low-*sum* grain boundary, surface, and work of separation energies to benchmark our DFT values against [301]. All grain boundary configurations used in this work were constructed using the Aimsgb software [302]. Figure 4.12 provides the reader with a visual representation of all

grain boundaries considered in this work, while Figure 4.13a encapsulates the data as a parity plot. Table 4.8 contains all grain boundary energies calculated here.

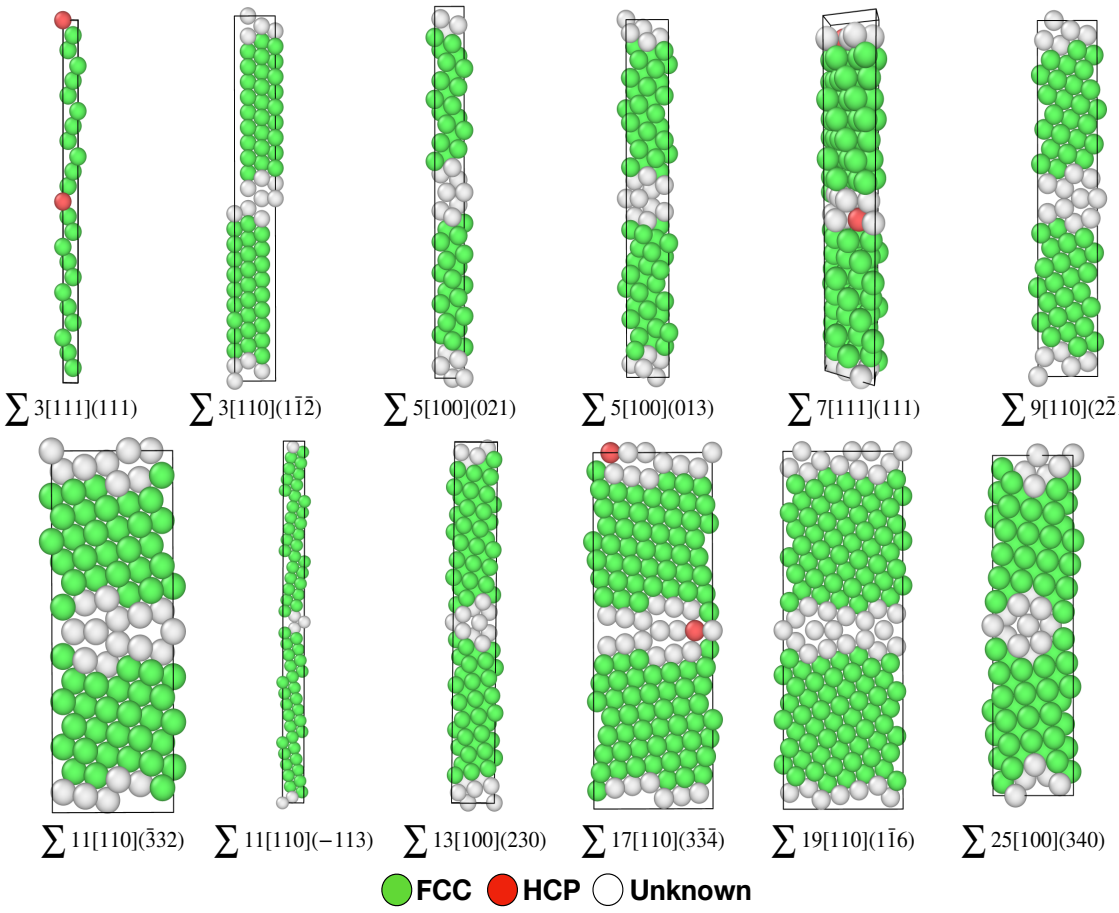

Figure 4.12: All grain boundary structures predicted in this work, prior to relaxation. Colors correspond to an atom's coordination environment.

Statistically, our ML-AGNI models have an root mean square error (RMSE) of 0.13 $\frac{J}{m^2}$ with respect to the DFT grain boundary energies. EAM-B, EAM-Z, and EAM-F yield RMSE values of 0.19 $\frac{J}{m^2}$, 0.17 $\frac{J}{m^2}$, 0.23 $\frac{J}{m^2}$ respectively. From these values, the agreement between DFT and our ML-AGNI models can clearly be seen. It is also worth noting that agreement between DFT and ML-AGNI, compared to the agreement between DFT and EAM, is greater as the complexity of the boundary plane increases. This indicates that our ML-AGNI models could be used to accurately explore the grain boundary energy for boundaries more complex than ∑25; a region in which the EAM potentials considered here

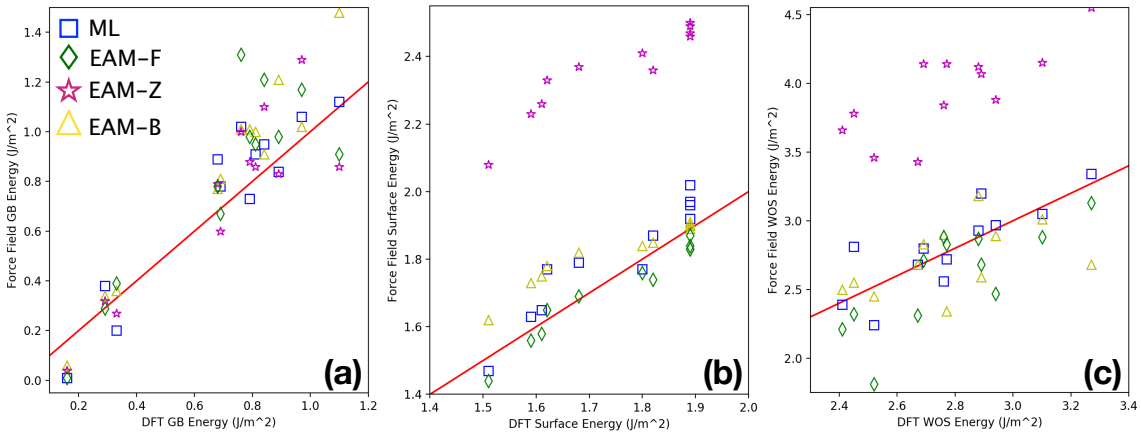

Figure 4.13: Grain boundary energy (a), surface energy (b), and work of separation energy (c) calculated for all grain boundaries and surfaces studied in this work. The parity line corresponds to the DFT prediction.

are likely to deviate from DFT.

The combination of surface and grain boundary energies can be used to predict the work of separation energy, or the energy required the cleave the grain boundary into two free surfaces. Figure 4.13c shows this data as a parity plot. Statistically, our ML-AGNI models have an root mean square error (RMSE) of 0.17 $\frac{J}{m^2}$ with respect to the DFT grain boundary energies. EAM-B, EAM-Z, and EAM-F yield RMSE values of 0.26 $\frac{J}{m^2}$, 1.17 $\frac{J}{m^2}$, 0.29 $\frac{J}{m^2}$ respectively. As our ML-AGNI models are in good agreement with DFT for both grain boundary and surface energies, the work of separation energies are also predicted extremely well. As all EAM potentials considered in this work perform inadequately for either surface energies or grain boundary energies, the combination of them compounds their errors. Statistical metrics used to judge the accuracy of all levels-of-theory used here, for all thermodynamic properties discussed, can be found in Table 4.10.

4.4.5 Capturing the behavior of grain boundaries in the presence of vacancies

During a dynamic environment, point defects diffuse in and around grain boundaries, making their way from one grain to another [303, 304, 305]. Therefore, understanding these environments at the atomic level allows us to fundamentally understand whether grain

Table 4.8: Grain boundary, surface, and work of separation energies, given in $\frac{J}{m^2}$, for several grain boundaries. Boundaries are ordered by increasing $\sum$.

Property	DFT	ML-AGNI	EAM-B	EAM-Z	EAM-F
Grain boundary energy					
$\sum 3(111)[111]$	0.16	0.01	0.06	0.04	0.01
$\sum 3(110)[1\bar{1}\bar{2}]$	0.69	0.78	0.81	0.60	0.67
$\sum 5(100)[021]$	1.10	1.12	1.48	0.86	0.91
$\sum 5(100)[013]$	0.89	0.84	1.21	0.83	0.98
$\sum 7(111)[111]$	0.29	0.38	0.34	0.32	0.29
$\sum 9(110)[2\bar{2}1]$	0.79	0.73	1.01	0.88	0.98
$\sum 11(110)[\bar{3}32]$	0.81	0.91	1.00	0.86	0.95
$\sum 11(110)[\bar{1}13]$	0.33	0.20	0.36	0.27	0.39
$\sum 13(100)[230]$	0.84	0.95	0.91	1.10	1.21
$\sum 17(110)[3\bar{3}\bar{4}]$	0.76	1.02	1.01	1.00	1.31
$\sum 19(110)[1\bar{1}\bar{6}]$	0.97	1.06	1.02	1.29	1.17
$\sum 25(100)[340]$	0.68	0.89	0.77	0.79	0.78
Work of separation energy					
$\sum 3(111)[111]$	2.88	2.93	3.18	4.12	2.87
$\sum 3(110)[1\bar{1}\bar{2}]$	2.69	2.80	2.83	4.14	2.71
$\sum 5(100)[021]$	2.77	2.72	2.34	4.14	2.83
$\sum 5(100)[013]$	2.89	3.20	2.59	4.07	2.68
$\sum 7(111)[111]$	2.76	2.56	2.90	3.84	2.88
$\sum 9(110)[2\bar{2}1]$	2.45	2.81	2.55	3.78	2.32
$\sum 11(110)[\bar{3}32]$	2.41	2.39	2.50	3.66	2.21
$\sum 11(110)[\bar{1}13]$	3.27	3.34	2.68	4.55	3.13
$\sum 13(100)[230]$	2.94	2.97	2.89	3.88	2.47
$\sum 17(110)[3\bar{3}\bar{4}]$	2.52	2.24	2.45	3.46	1.81
$\sum 19(110)[1\bar{1}\bar{6}]$	2.67	2.68	2.68	3.43	2.31
$\sum 25(100)[340]$	3.10	3.05	3.01	4.15	2.88

boundaries aid or prohibit the diffusion of point defects such as vacancies. To this end we have calculated the vacancy formation energy of the grain boundaries discussed in the last few paragraphs. However, the vacancy formation energy was calculated with respect to two distinct reference environments, providing unique insight into how vacancies affect the stability of both grain boundaries, as well as the vacancy diffusion process.

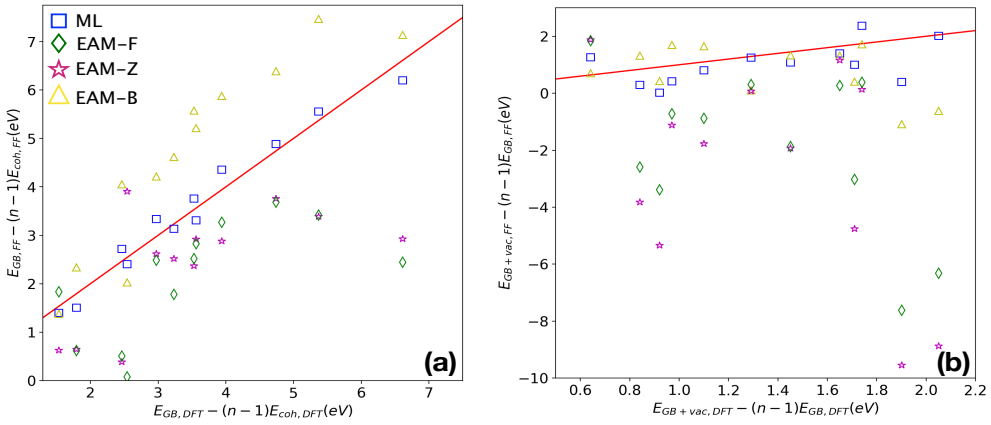

Figure 4.14: Vacancy formation energy of a single vacancy located inside of the grain boundary plane, using (a) bulk and (b) corresponding perfect grain boundary, as the reference system.

The first reference environment considered was a perfect bulk configuration. By using a bulk configuration as the reference, a direct comparison to the bulk vacancy formation energy can be made, providing insight into the thermodynamic stability of a vacancy within the grain boundary, compared to the bulk-like region of a grain. Using equation 10, and following the prescription described earlier in this work, the vacancy formation energy was calculated for all grain boundaries studied. Figure 4.14a provides the results of these calculations as a parity plot, and all values can be found in Table 4.9. Statistically, our ML-AGNI models have an root mean square error (RMSE) of 0.26 eV with respect to the DFT grain boundary energies. EAM-B, EAM-Z, and EAM-F yield RMSE values of 1.43 eV, 1.77 eV, 1.58 eV respectively. Our ML-AGNI models clearly show a significant improvement over the existing EAM potentials, for every considered grain boundary configuration.

It should also be noted that such environments were not included in the ML-AGNI

Table 4.9: Vacancy formation energies, given in eV, of a single vacancy within the GB plane with respect to a perfect bulk system, as well as with respect to the perfect grain boundary system, corresponding to each GB given in Table 4.8.

Property	DFT	ML-AGNI	EAM-B	EAM-Z	EAM-F
$E_{vacform}$ **bulk reference**					
$\sum 3(111)[111]$	1.53	1.40	1.38	1.84	0.63
$\sum 3(110)[1\bar{1}\bar{2}]$	2.54	2.41	2.03	0.08	3.91
$\sum 5(100)[021]$	2.97	3.34	4.22	2.49	2.62
$\sum 5(100)[013]$	3.56	3.31	5.22	2.83	2.92
$\sum 7(111)[111]$	2.46	2.72	4.06	0.51	0.39
$\sum 9(110)[2\bar{2}1]$	3.23	3.14	4.62	2.52	2.32
$\sum 11(110)[\bar{3}32]$	4.74	4.89	6.39	3.69	3.76
$\sum 11(110)[\bar{1}13]$	1.79	1.51	2.34	0.62	0.65
$\sum 13(100)[230]$	3.53	2.97	5.38	2.52	2.37
$\sum 17(110)[3\bar{3}\bar{4}]$	5.37	5.56	7.47	3.42	3.39
$\sum 19(110)[1\bar{1}\bar{6}]$	6.61	6.20	7.14	2.45	2.93
$\sum 25(100)[340]$	3.94	4.36	5.88	3.27	2.88
$E_{vacform}$ **GB reference**					
$\sum 3(111)[111]$	1.65	1.40	1.32	0.28	1.17
$\sum 3(110)[1\bar{1}\bar{2}]$	1.29	1.26	0.11	0.31	0.08
$\sum 5(100)[021]$	0.64	1.27	0.71	1.85	1.88
$\sum 5(100)[013]$	1.10	0.81	1.66	-0.88	-1.77
$\sum 7(111)[111]$	0.97	0.42	1.70	-0.72	-1.11
$\sum 9(110)[2\bar{2}1]$	1.45	1.09	1.34	-1.87	-1.92
$\sum 11(110)[\bar{3}32]$	1.71	0.99	0.41	-3.02	-4.75
$\sum 11(110)[\bar{1}13]$	1.74	2.37	1.72	0.39	0.14
$\sum 13(100)[230]$	0.84	0.30	1.33	-2.59	-3.82
$\sum 17(110)[3\bar{3}\bar{4}]$	2.05	2.02	-0.61	-6.32	-8.87
$\sum 19(110)[1\bar{1}\bar{6}]$	1.90	0.40	-1.08	-7.61	-9.54
$\sum 25(100)[340]$	0.92	0.02	0.44	-3.39	-5.33

Table 4.10: Statistical metrics used to judged all force field's performance on various thermodynamic properties calculated in this work. Each block corresponds to a specific property. The units of each value presented here corresponds to the units used for each property displayed in this chapper.

Statistical metrics	ML-AGNI	EAM-B	EAM-Z	EAM-F
γ_{GB}				
RMSE	0.13	0.19	0.17	0.23
σ	0.12	0.13	0.16	0.20
r^2	0.94	0.97	0.89	0.87
γ_{Surf}				
RMSE	0.08	0.1	0.61	0.04
σ	0.05	0.06	0.05	0.03
r^2	0.94	0.96	0.93	0.97
WOS				
RMSE	0.17	0.25	1.17	0.29
σ	0.17	0.24	0.19	0.22
r^2	0.82	0.47	0.77	0.77
$E_{vacform}$ **Bulk reference**				
RMSE	0.26	1.43	1.58	1.77
σ	0.26	0.83	1.13	1.09
r^2	0.98	0.91	0.62	0.63
$E_{vacform}$ **GB reference**				
RMSE	0.66	1.30	5.64	4.44
σ	0.57	1.16	3.79	2.95
r^2	0.53	-0.45	-0.47	-0.53

model's respective training sets. Therefore, we conclude that the ML-AGNI models can reliably extrapolate to such configuration domains, using precursor information such as pristine grain boundaries, and vacancies in a bulk configuration. Such an ability is crucial when simulating material's phenomena containing hundreds of thousands (or more) of atoms, as it is impossible to train the ML-AGNI models on every possible permutations of atomic configurations during a dynamic process.

The second reference environment considered was a grain boundary configuration without a vacancy. By using the grain boundary as the reference, one can compare the relative thermodynamic stability of the pristine grain boundary versus the boundary in the presence of a vacancy. Here, a positive number indicates that the pristine grain boundary would be more energetically favorable, compared to a negative number, which indicates the vacancy within the boundary plane is more favorable. Figure 4.14b provides the results of these calculations as a parity plot, and all values can be found in Table 4.9. Statistically, our ML-AGNI models have an root mean square error (RMSE) of 0.66 eV with respect to the DFT grain boundary energies. EAM-B, EAM-Z, and EAM-F yield RMSE values of 1.30 eV, 4.45 eV, 5.64 eV respectively.

It can be seen from Figure 4.14b that many predictions made by the EAM potentials actually indicate that the vacancy within the plane is more energetically stable, a result in stark contrast to DFT. Therefore, while the EAM potentials provide a good understanding of properties for the grain boundaries and surfaces, the introduction of a second defect within these configurations pushes their predictions into pure extrapolation, in which their accuracy breaks down. However, our ML-AGNI models clearly have the ability to make reliable predictions in this regime, and are a clear improvement over the existing models for Pt. Statistical metrics used to judge the accuracy of all levels-of-theory used here, for all thermodynamic properties discussed, can be found in Table 4.10.

However, the question of how likely is the diffusion of vacancies to occur along or away from the grain boundary plane, is not completely answered by the above calculations.

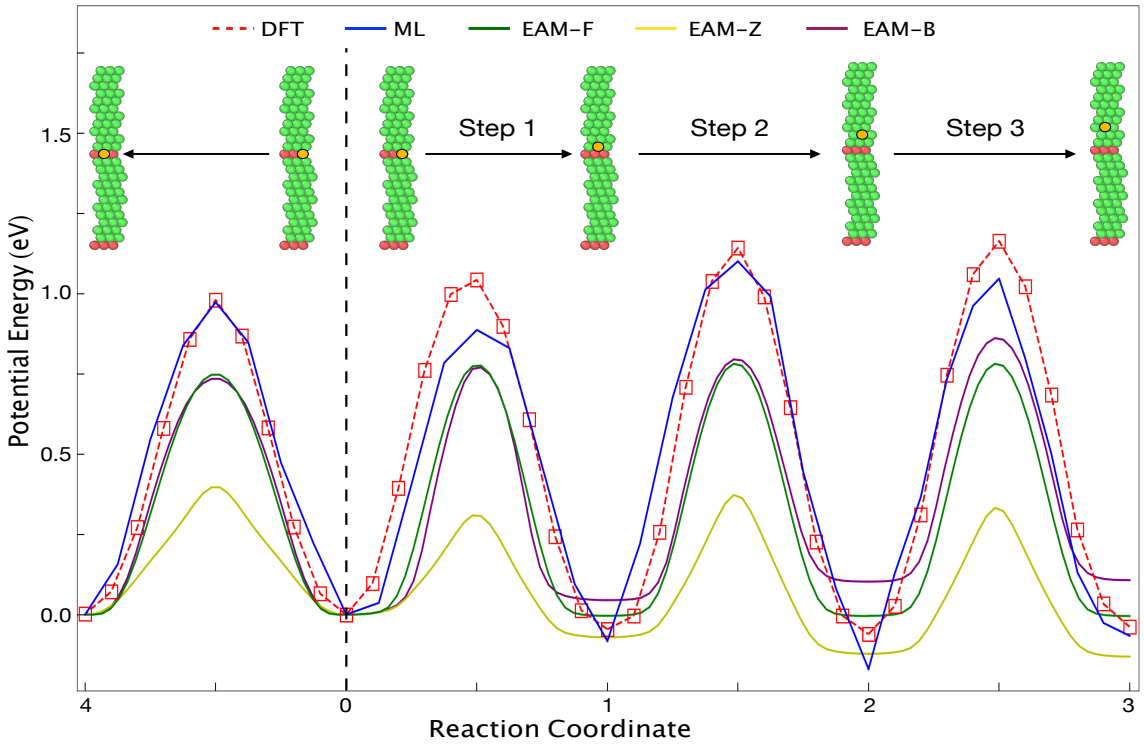

Figure 4.15: Nudged elastic band calculated diffusion pathways for a mono-vacancy diffusing in and away from the $\sum 3(111)[111]$ grain boundary plane. Reaction coordinates correspond to the pathway taken by the vacancy. The pathway taken along each reaction coordinate is described visually above the energy profiles.

In order to truly probe the kinetics of the diffusion process itself, nudged elastic band calculations were used to study these mechanisms. Here we consider a vacancy diffusing in and around the $\sum 3(111)[111]$ grain boundary plane. A 3x3x1 super-cell containing 215 atoms was used (compared to the 27 atom cell used to calculate the grain boundary energy) to avoid the vacancy interacting with its periodic image. Due to the super-cell sizes required to achieve this, only $\sum 3(111)[111]$ was considered in this work, and we leave a though a more thorough analysis for future work.

Figure 4.15 shows the minimum energy profile for the two diffusion pathways. Here there are two reactions present: (1) a vacancy moving to an adjacent site within the grain boundary plane, defined as moving from reaction coordinate 0 to 4 in Figure 4.15, and (2) a vacancy moving along the grain boundary normal into the bulk portion of the gain, defined as moving, in order, from reaction coordinate 0 to 1, then 1 to 2, and finally from 2 to 3 in Figure 4.15. From these calculations, one can see an increase in the DFT transition state energies as the vacancy diffuses away from the grain boundary plane, but also a negative energy difference between the initial configuration (vacancy in plane) and the final configuration (vacancy $10\mathring{A}$ away from boundary plane), which is consistent with the thermodynamic properties discussed previously. Our ML-AGNI models follow this trend, lining up with both DFT, but also the ML-AGNI predictions of the grain boundary vacancy formation energy.

However, the EAM potentials predictions disagree with not only DFT, but also with each other. All three EAM potentials predict a unique relationship between the initial and final configurations, for the pathway moving the vacancy away from the boundary plane. Only EAM-Z predicts the correct qualitative relationship, in that the final configuration is lower in energy than the initial configuration. Though this comes at the cost of transition state energies being nearly four times lower than that of DFT, indicating the diffusion mechanism to occur more frequently at lower temperatures. EAM-B and EAM-F, while predicting more accurate transition state energies, indicate that the vacancy is either equally likely,

or more likely, to end up staying within the boundary plane compared to migrating into the bulk-like region. This is both inconsistent with the DFT-NEB prediction, but also the respective EAM calculations of the grain boundary vacancy formation energy, indicating that these EAM potentials are not sufficient to study these configuration spaces.

4.4.6 Simulating the dynamic evolution of grains

While the previous section aimed to capture an atomic-level understanding of different defect classes,and their interactions with each other, larger length and time-scales must be explored to truly connect with experimental observations. To this end, we consider the phenomena of grain coarsening, as a function of temperature, through MD (NPT) simulations. Here, we aim to connect to experimental observations of annealing nano-crystalline Platinum during an irreversible recovery process [262] by calculating the average grain size as a function of temperature.

Experimentally, prior to 175C, there is no change in the average grain size observed, outside of statistical fluctuations. It has been proposed that this behavior is due to the relaxation of unstable grain boundaries, to their respective metastable configurations [262]. Between 175C and 200C the mean grain size begins to increase, and continues to increase through 325C.

Figure 4.16 (top) shows the distribution of grains sizes, along with a fitted, normalized gaussian function, for several temperatures around the transition point between metastable grain-boundary transition, and grain growth. Figure 4.16 (bottom) shows the mean grain sizes plotted as a function of each temperature studied in this work. The NPT simulations performed using our ML-AGNI models predict a transition point at exactly the same temperature as experiments, showing excellent agreement between ML-AGNI and experiments. We also extend the temperature range beyond that of experiments, to 425C. While our MD simulations indicate that grain growth plateaus between 325C and 350C, such a feature could be an artifact of the system size, and larger system sizes may not yield such

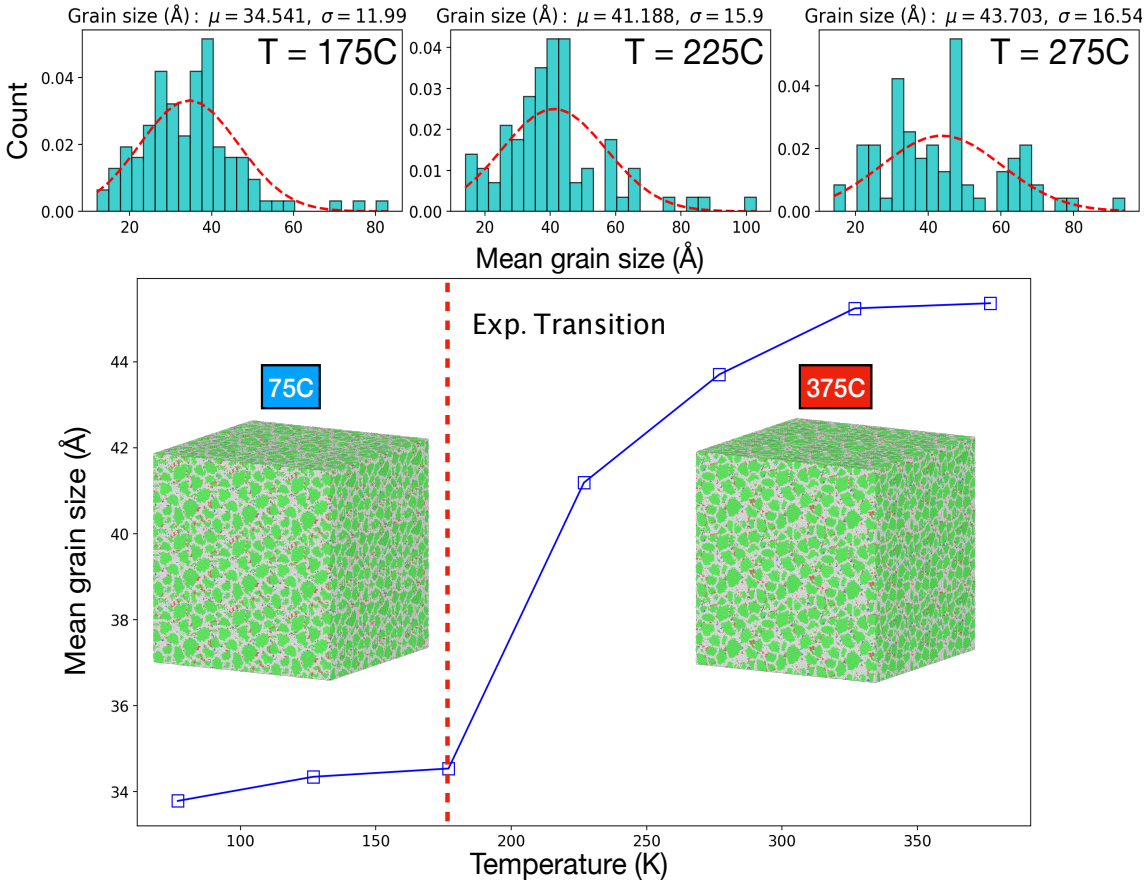

Figure 4.16: (Top) Normalized histograms detailing the grain sizes calculated from MD simulations at temperatures between 125C and 225C. Mean grain size and spread of grain sizes can be seen above each histogram. (Bottom) Predicted grain size as a function of temperature. The vertical dotted line corresponds to the experimental transition temperature, in which grain grows begins. The resulting grain structure from the ML-AGNI MD simulations for 75C and 325C are shown to the left and right, respectively.

behavior.

There is one critical piece of information to note from these MD simulations. We emphasize here, that with the system sizes considered in this work, we cannot attain mean grain sizes in direct comparison with experiments. However, previous MD work on grain growth has indicated that system sizes containing more than 16 million atoms would be needed to quantitatively compare the grain structure with experiments. Therefore, the aim of this work is not to predict the exact grain structure, but rather to observe that grain growth does not occur prior to 175C.

4.5 Summary

In this chapter, we further extend the scope of the ML-AGNI paradigm by incorporating the predictions of atomic forces, stresses, and potential energy simultaneously and seamlessly through three independent ML-AGNI models. This paradigm bypasses the primary drawback of many prominent ML-AGNI strategies by independently learning all predicted atomic-level properties. The various ML-AGNI models were validated by accurately reproducing bulk thermal, vibrational, elastic, and diffusive properties of bulk Platinum. In particular, we highlight the ability of the ML-AGNI models to accurately predict properties such as the kinetics of divacancy dissociation/diffusion, the temperature dependence of the mechanical properties of Platinum, as well as the dynamic evolution of grain sizes during an annealing process, simulated via MD.

The ML-AGNI models presented in this chapter show a clear improvement over current EAM potentials, when considering the predictions made over all of the various tests performed in this work. The ML-AGNI models used here also represent a paradigm shift, in that a first iteration of models were created to study purely bulk and vacancy behavior, and were then iteratively improved to study grain boundary and surface phenomena, using the previous ML-AGNI models as a starting point. They also, purposefully, do not contain reference data for all of the environments studied here, indicating there extrapolative power allows them to be reliably used to study a plethora of materials phenomena. Using ML-AGNI models, with the accuracy of DFT, and the speed of classical/semi-empirical models, allows us to accurately and reliably study properties that cannot be computed using DFT. This work adds another layer of validation that ML-AGNI models can make reliable predictions over multiple length and time-scales, and solidifies ML-AGNI as a vital tool in the study of atomic and nano-scale research.

CHAPTER 5
UNDERSTANDING THE ATOMIC STRUCTURE OF LIQUID PHASES OF LITHIUM WITH MACHINE LEARNING

5.1 Introduction

For many years, alkali metals were considered relatively simple systems, owing to their straightforward electronic structure at low temperatures and pressures [306]. However, over the last twenty years, it has become apparent that such metals are not so simple, and exhibit a rich set of structural transitions throughout both the solid and liquid phases at increasing pressures [307, 308, 309, 310, 311, 312, 313]. Perhaps more interestingly, is that the local atomic structure in a particular liquid phase, is shockingly similar to the corresponding crystal phase (at a specific pressure) [309]. Therefore, the notion that understanding the geometries present in the liquid phases, computationally, can lead to insights regarding the crystal phases is gaining popularity, in part due to the difficultly in experimentally determining the atomic structure of crystal phases at high pressures. However, studying the liquid phases computationally is a daunting challenge, due to the time-scales required to accurately capture the liquid phases' structure, as well as the lack of reliable semi-empirical/classical models for these domains [314, 315].

In this chapter, I use a combination of DFT and ML to accurately predict the atomic structure of liquid phases of lithium, over a range of nearly 400GPa. Nearest-neighbor distributions, coupled with time-averaged pair correlation functions are used to generate a reliable picture of an atom's local geometry at different pressures. A comparison between three models, used to predict the atomic forces, using KRR, NN, and EAM, is made for several different liquid phases, to emphasize the need to transition to NN to reliable study these configuration spaces. The NN force model is then used to study the entire range of

pressures, and validated against DFT. Finally, the NN force model, combined with KRR models for energy and stresses, is used to perform anisotropic NPT simulations to study the crystal phase, at a given pressure, obtained when dynamically quenching from a particular liquid phase.

5.2 Computational details

5.2.1 Density functional theory details

DFT calculations were performed to generate a robust set of data for the training of ML models. This data also serves to validate the ML models. All DFT calculations were performed using VASP [194, 195]. The PBE functional [196] was used to calculate the electronic exchange-correlation interaction. A customized PAW potential was used, due to the complexity of oscillations in the core region at high pressures making previously available PAW potentials inadequate for this work. Plane-wave basis functions up to a kinetic energy cutoff of 1350 eV were used [197]. All projection operators (involved in the calculation of the non-local part of the PAW pseudopotentials) were evaluated in the reciprocal space to ensure further precision. A k-point mesh of 1x1x1 was used, but was shifted from the gamma point by $(\frac{1}{2}\text{x}\frac{1}{2}\text{x}\frac{1}{2})$. This shift yields convergence, with a single kpoint, to the same energy as a 4x4x4 mesh centered at the gamma point, thereby reducing the cost of all DFT calculations.

MD simulations were performed in the canonical ensemble, at $T = 1000K$, for all liquid simulations. The Nose mass was carefully calibrated to predict the correct phonon density of states of several liquid phases. MD simulations began at a pressure of 77GPa, as the structure at this pressure was previously known. Each run was performed for 50ps, to allow for equilibration of the atoms, followed by a 5% increase and decrease of the unit vectors, to simulate different pressures. This process was performed until a range of pressures between 36GPa and 345GPa was obtained.

Table 5.1: Statistical error metrics of the final ML-AGNI models, for each property learned, generated in this work. All values presented here are the metrics calculated on a given model's test set, not a model's training set. The final rows correspond to the number of training points in the final models. The force model column is broken into 2 pieces, the first number corresponding to KRR, and the second number corresponding to the NN model.

Error Metric	Energy model (meV/atom)	Force model (eV/Å)	Stress model (GPa)
RMSE	3.37	0.45; 0.24	9.41
STD	3.37	0.44; 0.25	9.41
Max 1 % Error	9.35	8.42; 1.73	39.21
r^2	0.99	0.81; 0.99	0.99
# Training Points	5000	5000; 10,000,000	5000

5.2.2 Machine learning model details

To generate a ML model capable of learning the atomic forces, the $\mathbf{v}^2$ fingerprint was used. Due to the highly asymmetric structures present in the liquid phases, having a densely populated set of symmetry functions at specific distances from an atom, provides a significant benefit over the atom-centered approach described in $\mathbf{v}^1$. 48 symmetry functions were used to generate the fingerprint, each with a $w = 0.1$. A NN was used to establish a mapping from the $\mathbf{v}^2$ features to the atomic force components. The architecture and training process of the NN is described in chapter 2. The NN model was trained on 10,000,000 reference DFT points from across all liquid phases. The final NN model yielded an RMSE of $0.24\frac{eV}{\mathring{A}}$, standard deviation of $0.25\frac{eV}{\mathring{A}}$, and maximum 1% error or $1.73\frac{eV}{\mathring{A}}$ on the remaining DFT data not included in the mode's training set.

KRR was used to generate energy and stress tensor models, using the fingerprint setup described in chapter 2, and shown in table 5.1. Each model was trained on 5,000 reference points. The final KRR energy model yielded an RMSE of $3.37\frac{meV}{atom}$, standard deviation of $3.37\frac{meV}{atom}$, and maximum 1% error or $9.35\frac{meV}{atom}$ on the remaining DFT data not included in the mode's training set. The final KRR stress tensor model yielded an RMSE of 9.41kB, standard deviation of 9.42kB, and maximum 1% error or 39.21kB on the remaining DFT data not included in the mode's training set.

Table 5.2: The final fingerprint forms utilized to learn energy, stresses, or atomic forces. For the property type, the subscripts i and I represent a per-atom or per-structure quantity respectively, and the superscripts α,β represent two possible Cartesian directions.

Property Type	# σ_k	σ_k Range (Å)	Final Fingerprint Form
Forces (F_i^{α})	48	(1.0, 8.0)	$\mathbf{v}^2_{i,\alpha;k}$
Stresses ($S_I^{\alpha,\beta}$)	20	(1.0, 8.0)	$\left\{ M^n\left(\sum_{i=1}^{N} T_{i,\{\alpha,\beta\};k}\right) \right\}$
Energy (E_I)	20	(1.0, 8.0)	$\left\{ M^n\left(\sum_{i=1}^{N} S_{i,k}\right), M^n\left(\sum_{i=1}^{N} V_{i,k}\right), M^n\left(\sum_{i=1}^{N} T_{i,k}\right) \right\}$

5.2.3 Molecular dynamics details

All EAM and ML MD calculations were performed using LAMMPS [177]. To calculate the nearest-neighbor distributions, NVT simulations, at a given pressure, were performed for 25ps. Anisotropic NPT simulations were also performed using the ML models to study the crystal structure obtained via quenching. These MD simulations were performed for 50ns, allowing ample time for equilibration at a new pressure.

5.3 Simulating the atomic structure of liquid lithium

5.3.1 Comparison of semi-empirical potentials with machine learning models

Several pressures, 36GPa, 114GPa, and 345GPa were chosen to benchmark the created ML models, with both the reference DFT data, as well as an EAM potential chosen from the literature. It should also be noted that there are very few EAM potentials available for lithium, and none that claim any reliability when studying liquid phases [314, 315]. The benchmark pressures were chosen due to their differences in local atomic structure, providing a good basis for the range of pressures studied in this chapter. Figure 5.1 shows the nearest-neighbor distributions for the three benchmark pressures, for all levels-of-theory used to study them. Each curve represents a histogram of the nth nearest-neighbor, averaged over the entire MD simulation.

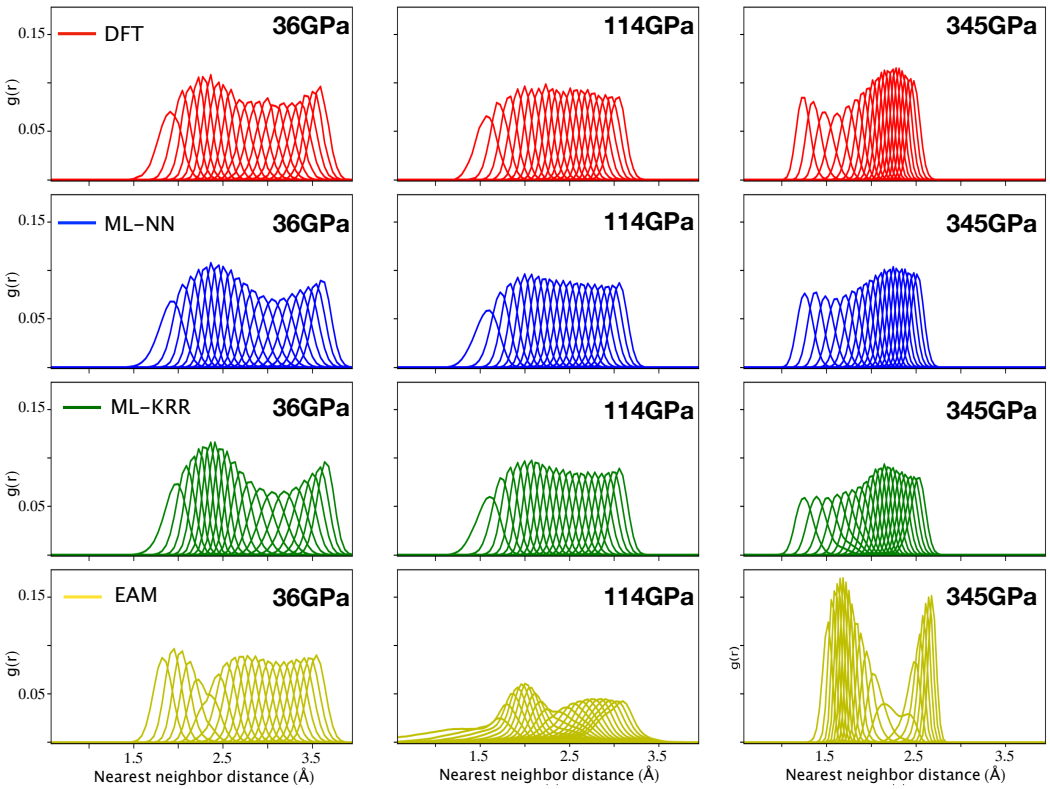

Figure 5.1: N^{th} nearest neighbor positions histograms, averaged over the course of an MD simulation, with each column corresponding to a different liquid phase of Li. Colors represent different simulation methods, with red being DFT, blue being a NN ML-AGNI model, green being a KRR ML-AGNI model, and yelloe representing an EAM potential.

At 36GPa, two peaks are observed with DFT, one corresponding to the peak in the 6^{th} nearest-neighbor located at approximately 2.42 Å, and the other corresponding to the peak in the 20^{th} nearest-neighbor located at approximately 3.52 Å. The NN simulations predict identical results to DFT, though with slightly different densities for several of the distributions. However, the KRR model predicts the first peak to correspond to the 7^{th} nearest-neighbor located at approximately 2.47 Å. While the KRR model does predict the second peak at the 20^{th} nearest-neighbor peak, the depth of the valley between the two peaks is much deeper than that of the DFT and NN distribution. Finally, one can see that the EAM generated distribution is poorly predicted, with the first peak corresponding to the peak in the 2^{nd} nearest-neighbor, and almost not difference in the density between the 9^{th} and 20^{th} neighbor distributions.

At 114GPa, only a single peak is observed with DFT, corresponding to the peak in the 8^{th} nearest-neighbor located at approximately 2.23 Å. The NN simulations predict a similar trend with respect to DFT, with only a single peak present. However, this peak occurs at the 5^{th} nearest-neighbor. The KRR model predicts the presence of two peaks, albeit the second peak is very subtle. The first peak is predicted to correspond to the 6^{th} nearest-neighbor located at approximately 2.12 Å, and the second peak at 3.09 Å, corresponding to the 20^{th} nearest-neighbor distribution. Again, is it obvious that the EAM generated distribution is in poor agreement with DFT, with atoms more-or-less overlapping with each other, an indication of a complete breakdown in the physics of the system, and a nearest-neighbor distribution in total disagreement with DFT.

At 345GPa, two peaks are observed with DFT, one corresponding to the peak in the 1^{st} nearest-neighbor located at approximately 1.26 Å, and the other corresponding to the peak in the 15^{th} nearest-neighbor located at approximately 2.31 Å. The NN simulations predict a very similar trend, but yielding distribution densities more subtle than the stark differences observed by DFT. However, the first peak does correspond to the peak in the 1^{st} nearest-neighbor located at approximately 1.24 Å, and the other corresponding to the peak in the 14^{th} nearest-neighbor located at approximately 2.25 Å. The KRR model predicts the presence of only a single peak, corresponding to the 12^{th} nearest-neighbor located at approximately 2.16 Å. Similarly to the previous pressures, the EAM generated distribution is in stark contrast to DFT, with the EAM potential actually predicting a stable crystalline phase present at 345GPa. While experiments have yet to probe this regime thoroughly, it is unlikely that this combination of pressure and temperature would result in a crystal phase [316, 317].

5.3.2 Neural network predictions of liquid lithium

The previous section discussed the predictions made by two ML models, as an EAM potential, with respect to DFT. This sections aims to fill the gaps between liquid phases studied

in the previous section using the NN model. Figure 5.2 shows nearest-neighbor histograms for all the pressures studied here, obtained via DFT and the NN model. From this plot, one can see the overall excellent agreement between ML and DFT, especially for pressures up to 161GPa. Between 161GPa and 279GPa some discrepancies arise, especially at 161GPa, 194GPa, and 279GPa. For 161GPa and 194GPa, there is disagreement between DFT and ML regarding the peaks around the 15^{th} nearest-neighbor, with DFT predicting an observable peak, and ML predicting a nearly uniform density for all peaks between 10^{th} nearest-neighbor and the 20^{th} nearest-neighbor distribution. At 279GPa, DFT clearly predicts a peak at the 1^{st} nearest-neighbor distribution, followed by a slight valley and then a sharp rise. The NN model however does not predict a peak at the 1^{st} nearest-neighbor distribution, and instead gradually rises until a peak is reached at the 15^{th} nearest-neighbor distribution. It should be noted however, that ML and DFT do agree on the location of the peak located at the 15^{th} nearest-neighbor distribution.

While it is useful, as a first step, to compare the general shape and position of the nearest-neighbor histograms, it is still a relatively qualitative comparison between ML and DFT. A more telling analysis comes from the calculation of the average nearest-neighbor distances, relative to a given liquid phase. From this information, we can determine if, for example, the first nearest neighbor at 345GPa, is closer or further away, on average, than the first nearest neighbor at 46GPa. This provides us with important information regarding the structural differences between liquid phases, and ultimately provides insight to the potential crystal structures at a given pressure.

This information can be found in Figure 5.3, for DFT and ML. Here, the reference is chosen as the liquid phase at 46GPa, and is based on the level-of-theory (ML liquid phases use the liquid phase at 46GPa, predicted by ML, as their reference, and not the liquid phase predicted by DFT at 46GPa). Only a select few liquid phases are shown for the sake of simplicity, as the curves become indistinguishable from each other when all phases are present. From Figure 5.3, it is observed that, as the pressure increases,

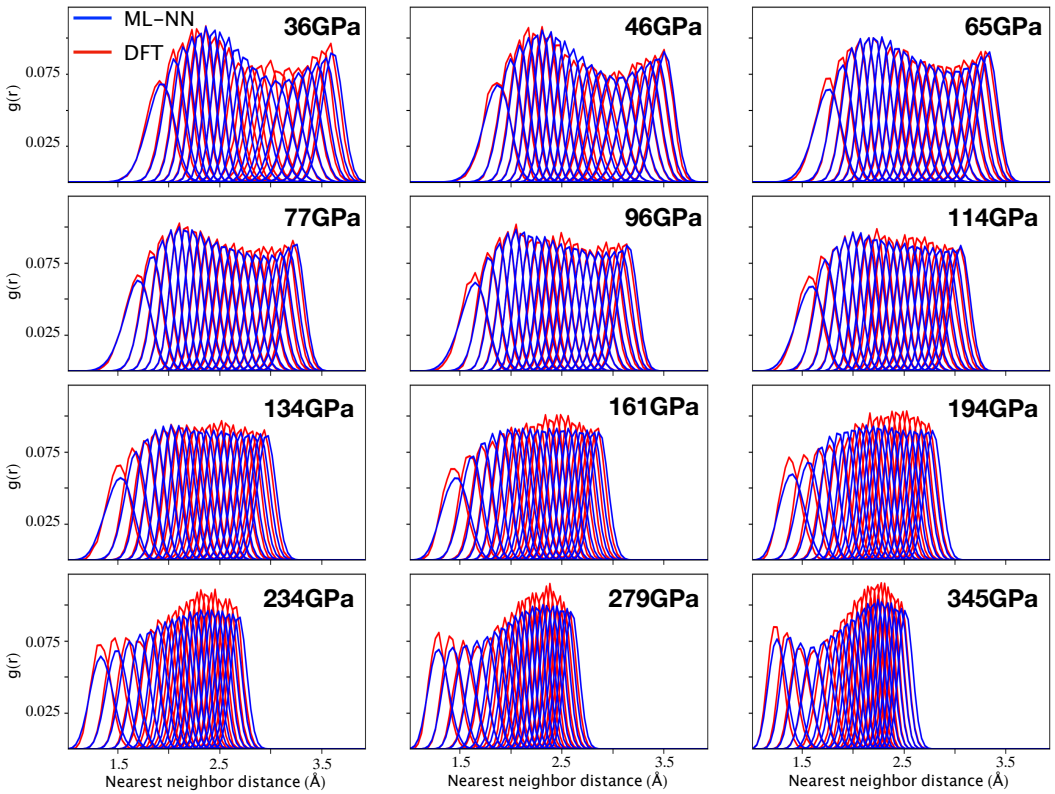

Figure 5.2: Nth nearest neighbor positions histograms, averaged over the course of an MD simulation, with each plot corresponding to a different liquid phase of Li. Colors represent different simulation methods, with red being DFT, and blue being a NN ML-AGNI model. All x and y axis are fixed, to give the reader a visual understanding of the decrease in nearest-neighbor distances as the pressure increases.

the first two nearest-neighbors are, on average, closer together. However, from the 3rd nearest-neighbor to the 8th nearest-neighbor, the average distances is larger than that of the reference phase. This is due to the fact that, at lower pressures, the liquid is more diffuse, owing to a larger percentage of free-volume. At higher pressures, the structure is much less diffuse, effectively locking the atoms into a highly disordered configuration. In all cases, ML and DFT show excellent agreement, with both the trend captured correctly, but also the relative difference in the curves, with respect to pressure changes, also being predicted correctly. As the nearest-neighbor index increases, the disagreement between ML and DFT also grows. However, this could be in-part due to the fingerprint chosen to represent the structures, with the atoms located at the tail end of the nearest-neighbor distribution having

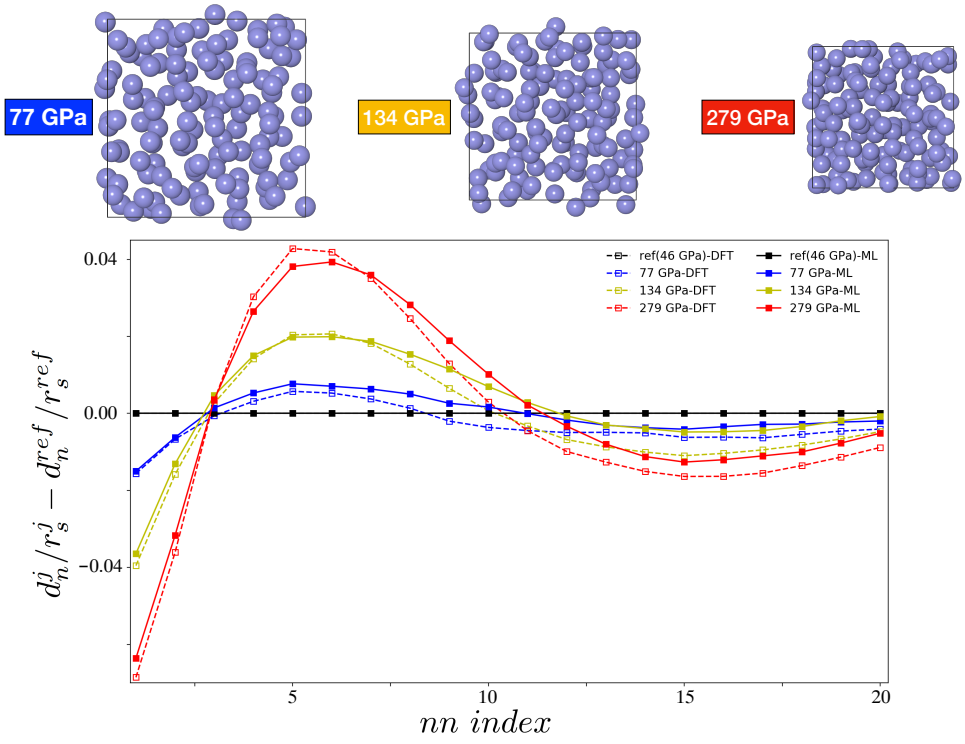

Figure 5.3: Relative nearest-neighbor distances for several liquid phases of Li. Colors correspond to a different liquid phase, while open and filled square markers correspond to different simulation methods (open) DFT, (filled) ML-AGNI, and the dashed lines correspond to DFT, while the solid lines correspond to ML-AGNI. The reference phase was taken as the phase at 46GPa. Negative numbers imply a shorter distance between neighbors than at the reference phase, whereas positive numbers indicate a larger distance between neighbors than at the reference phase. Images shown at the top represent the atomic configuration of the various liquid phases plotted below.

their influence reduced due to the cutoff function. Therefore, a slight change in fingerprint may result in immediate improvement of these regions.

5.4 Recovering crystal structures of lithium via dynamic quenching

The dynamic behavior of phase changes is non-trivial, and often impossible, due to the complexity of such transformation, but also the time-scales required to accurately observe them[318, 319]. However, one can use a slow-quench MD method, in which the thermostat slowly cools the configuration, while tailoring the rate of cooling to allow for equilibration

at each new average temperature. Such simulations often require many nanoseconds to observe any change in the atomic structure, and are therefore well outside of the reach of DFT.

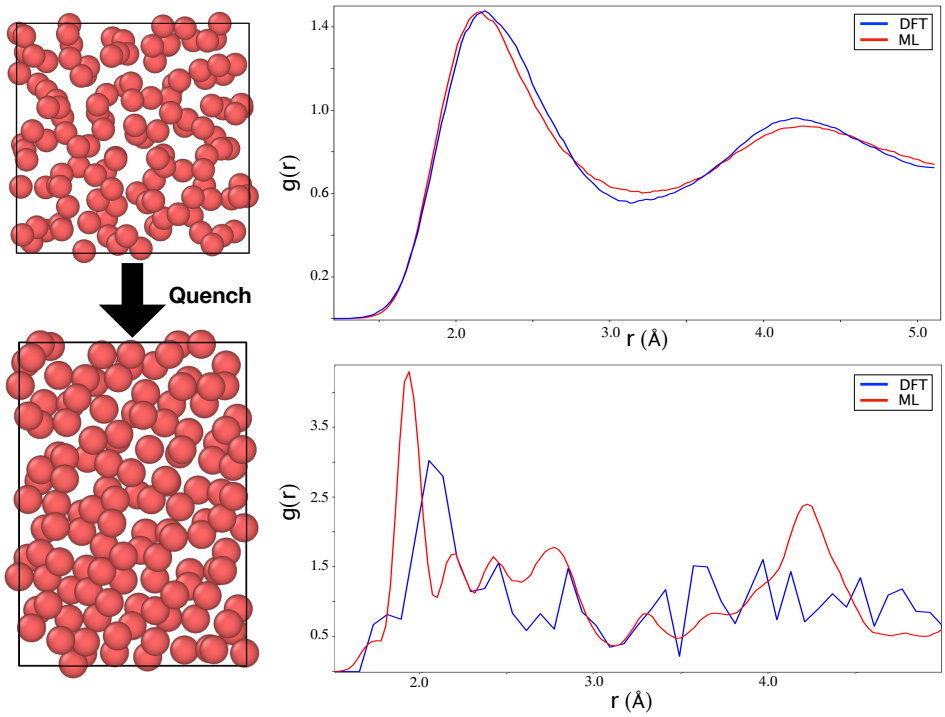

Figure 5.4: (Left) Atomic configurations of the liquid phase of Li at 77GPa at (top) 1000K, and (bottom) 200K. Structures were obtained via anisotropic NPT simulations with the NN ML-AGNI models. (Right) Time-averaged pair-correlation functions at (top) 1000K, and (bottom) 200K. Colors correpsond to the level-of-theory, with red corresponding to ML-AGNI, and blue corresponding to DFT.

Here, the quenching of the liquid phase, corresponding to 77GPa is studied, via anisotropic NPT simulations. There are a few caveats to such simulations though: (1) The number of atoms present in the liquid does not line up with the required number of atoms in the corresponding crystal phase, and (2) only 0K atomic positions exist for the crystal phase at 77GPa. These limitations will obviously affect the final structure comparison between DFT and ML however, the goal of this section is not to compare the exact positions of atoms, but rather to gain insight into whether the ML models can be trained on only liquid phases

and quench to a structure even remotely close to the DFT prediction.

Figure 5.4 shows the results of the ML MD simulation. On the left, the initial liquid structure is shown at the top, and the final "crystal" structure is observed at the bottom. The right side of the plot shows the time-averaged pair correlation function of both the liquid phase (top) and the resulting crystal phase (bottom). A few interesting observations emerge from this data. Both DFT and ML show a small peak prior to 2Å, followed by a large peak. While there appears to be a splitting of the peaks from ML, and only a single broad peak with DFT, one must remember that the DFT data is obtained at 0K, and may show splitting at temperatures $>$ 0K. Several peaks follow up to 3Å, in which a large valley is observed. Both ML and DFT show peaks up to 3Å, aligned at similar distances, but with different densities. Both DFT and ML predict an almost identical valley shape after 3Å, indicating that the immediate structure.

The final cell shape, obtained by ML, also agrees somewhat with DFT. The final predicted lattice parameters for ML were (a =10.73Å, b =7.81Å, c =11.12Å), compared to the predicted DFT values of (a =9.08Å, b =7.22Å, c =9.93Å). While the absolute values are slightly off, they shouldn't agree completely due to the limitation described earlier. However, the liquid phase's cell began as a perfect cube, indicating that the ML stress tensor model is capable of independently altering the lattice vectors during a dynamic simulation, and at least qualitatively agree with the predicted DFT structure. The relative agreement in final structures also indicate that the NN force model is capable of extrapolating to environments, especially those with wildly different cell shapes than it was trained on, with decent accuracy, far outperforming any classical/semi-empirical model for lithium.

5.5 Summary

In this chapter, a NN model for atomic forces, along with KRR models for the energy and stress tensor predictions was created to study the dynamics of liquid lithium. The atomic structure of liquid phases, spanning nearly 400GPa was studied. A comparison of

KRR and NN model, for the prediction of atomic forces was performed to highlight the breakdown of KRR models, and the need to explore more sophisticated ML algorithms for complex materials problems. Nearest-neighbor distributions were calculated for all studied liquid phases, to showcase the good overall agreement between ML and DFT. Relative nearest-neighbor distances were also calculated, showing not only the differences between the atomic structure of various liquid phases, but also the ML model's ability to accurately model these differences. Finally, the dynamic quenching of a liquid phase of lithium at 77GPa was performed using anisotropic NPT simulations, with the ML predicted unit cell and atomic structure in decent overall agreement with DFT.

The ML calculations presented in this chapter show a clear improvement over the available EAM potential, with the ability to simulate complex properties of highly disordered liquid phases of lithium. The ML models presented here also, purposefully, do not contain reference data for all of the environments studied, indicating there extrapolative power allows them to be reliably used to study a multitude of phenomena. Using ML models, with the accuracy of DFT, and the speed of classical/semi-empirical models, allows one to accurately and reliably study structural properties of physical complex systems. This work adds another layer of proof that ML models can make accurate and reliable predictions on systems that are far from the pristine case-study examples of the past, further bridging the gap between DFT and experiments for the study of liquid metals.

CHAPTER 6

SUMMARY AND OUTLOOK

Understanding the atomic-level behavior of materials, and how that translates to observable experimental phenomena is an important topic in materials science. These problems encompasses time and length scales that span several orders of magnitude, pushing current theoretical/computational methods to their limit. As our need for better materials pushes us to probe and manipulate these regimes, the ability to understand the complexity that awaits us grows ever more necessary. Ultimately, our capacity to conquer such problems relies on our ability to reliably simulate the dynamic environments that await us, capturing both the thermodynamic and kinetic relationships that exist. Thus far, a combination of *ab initio* methods and classical/semi-empirical methods have been instrumental in our understanding of the processes that take place in these domains. Their ability to predict properties such as energy, forces, and stresses, for a diverse set of chemical species and configurations, makes them immeasurably powerful. Nevertheless, the computational cost of *ab initio* methods severally restricts the types of problems that can be studied to that of length-scales on the order of a few nano-meters, and time-scales of a few nano-seconds. While semi-empirical/classical reduce this burden, and open the door to the exploration of more complex regimes, their lack of transferability also restricts their applicability to a small set of problems with configurations similar to the data used to create them. To overcome these drawbacks, this work employs emerging machine learning techniques to build upon the best aspects of *ab initio* and semi-empirical/classical methods. By combining the accuracy of *ab initio* methods, with the sophisticated mathematical frameworks of machine learning, predictive models can be created in a fraction of the time as classical methods, but at prediction costs equivalent to them. Such a framework ultimately allows for the study of problems with the accuracy of *ab initio* methods, but at the cost of semi-empirical/classical

methods.

In this thesis, machine learning methods were used in the construction of predictive models for the study of atomic/nano-level materials behavior. A prescription to numerically decompose an atom's local geometry, and map those values to properties such as the potential energy, atomic forces, and total stress tensor was proposed. Integration of this platform into LAMMPS for the study of a multitude of materials problems ranging from nudged elastic band calculations to molecular dynamics was described. Using this platform, several distinct aspects of atomistic phenomena, were then considered.

In the first example, surface phenomena, such as the melting temperature of the Al (111), (110), (100) surfaces and (111)-(100) Wulff nano-particles, the kinetics of adatom diffusion processes on the Al (111), (110), and (100) surfaces, the nucleation of islands on the Al (111) surface, and the expitaxial growth of the Al (110) surface via atomic-layer deposition was studied. In the second example, the behavior of point, planar, and line defects in Platinum was studied, along with the dynamic behavior of defect-free bulk properties. Grain boundary and surface energies were predicted for a variety of non-trivial boundaries/surfaces. The kinetics of defect diffusion, such as the migration of adatoms on surfaces, and vacancies in bulk, and around grain boundaries was studied. The temperature dependence of the mechanical and elastic properties of defect-free bulk environments was predicted. Finally, the dynamic effects of temperature on the coarsening of grains was also predicted. In the third example, the atomic structure of liquid lithium was studied over a range of pressures spanning nearly 400 GPa. The failure of more simplistic machine learning methods, and the need to move to more complex ones, is discussed. Crystal structures, obtained by dynamically quenching the liquid environments, were then studied, and compared to experimentally observed atomic configurations.

Thus far, the work in this thesis has demonstrated the power of machine learning for atomistic materials simulations. This work paves the way for the use of these methods to study more complex phenomena, that no method currently available can reliably predict.

However, there are still challenges that need to be solved before such methods will be used by the community as a mainstream tool. These challenges are discussed below.

The need for more data

As the types of problems one wishes to study become more and more complex, in terms of the physical structures required to study such phenomena, the need for reliable reference data will increase exponentially. However, the reference data used, generally created by *ab initio* methods, is not cheap, and rapidly a wall will be reached. Enhanced sampling techniques, such a metadynamics or accelerated molecular dynamics, will be needed to effectively explore the required conjuration spaces. This data must also be created in a uniform manner, as any discrepancies in the accuracy of the reference data will wreak havoc on the machine learning models.

Adaptive machine learning models

Eventually one runs into a problem, where including more points into your machine learning model does not improve its predictive capabilities. This is in part due to the model's prediction being heavily weighted in a particular region of the configuration space. Therefore, adaptive models, that can intelligently scan the complexity of the environments provided, and select the training data that will result in the best model, will become increasingly important. Even more so, the ability to retrain models on-the-fly during a prediction will eliminate the tedious down-time required to analyze the model's deficiencies and improve it manually. Such a paradigm will dramatically speed up the model generation/retraining processes, allowing for the efficient exploration of interesting phenomena.

Numerical descriptors for complex chemical systems

Perhaps the most important, and difficult, of the challenges is the need for better numerical descriptors. The fingerprinting process used in this work has been very successful in the

study of elemental metals, but what about other chemical systems? Can these fingerprints be reliably used for systems in which bonding plays an important role? What about systems with long-range electronic effects? What changes are required to study alloy, oxide, and polymer systems? Most of the urgent materials problems require the study of these systems, only increasing the urge for the construction of descriptors that can study them. One must be careful however, as any increased complexity will come at the cost of speed, transferability, or both.

Appendices

APPENDIX A

PRELIMINARY MACHINE LEARNING MODELS FOR ELEMENTAL SYSTEMS

In this section three machine learning models are presented: (1) Aluminum stress tensor model, (2) Copper potential energy model, (3) Copper stress tensor model, and (4) Carbon potential energy model. While these three models have not been tested as rigorously as those presented earlier in this thesis, they are still capable models, trained over a diverse set of reference data, and should be capable of making reliable predictions for numerous environments.

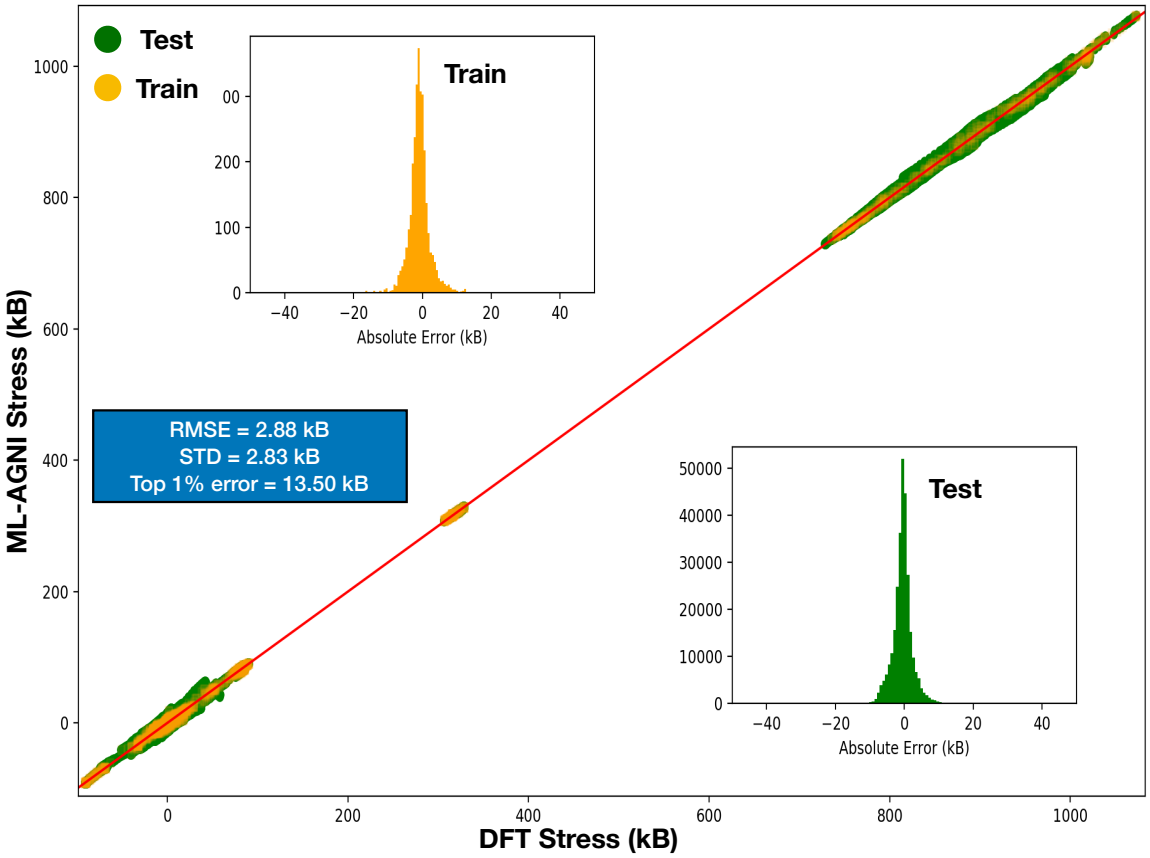

Figure A.1: Parity plot representing the ML model's stress tensor predictions on the DFT reference data for Aluminum. The plot is broken into the predictions made on the training (yellow), and test (green) data. Two of the inserted figures show a histogram of the absolute errors between ML and DFT for both the training and test set (colors correspond to those in the main plot). The third inset shows statistical metrics used to judge the model's performance versus DFT.

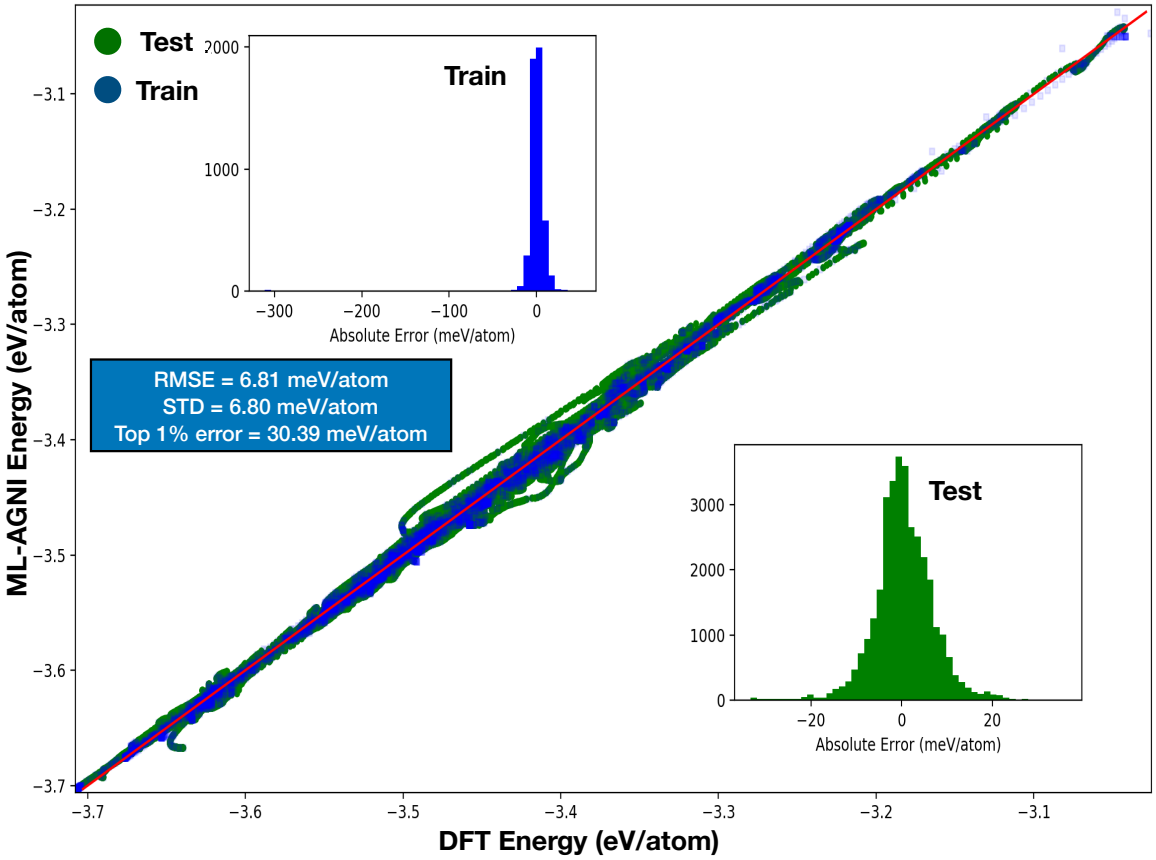

Figure A.2: Parity plot representing the ML model's potential energy predictions on the DFT reference data for Copper. The plot is broken into the predictions made on the training (blue), and test (green) data. Two of the inserted figures show a histogram of the absolute errors between ML and DFT for both the training and test set (colors correspond to those in the main plot). The third inset shows statistical metrics used to judge the model's performance versus DFT.

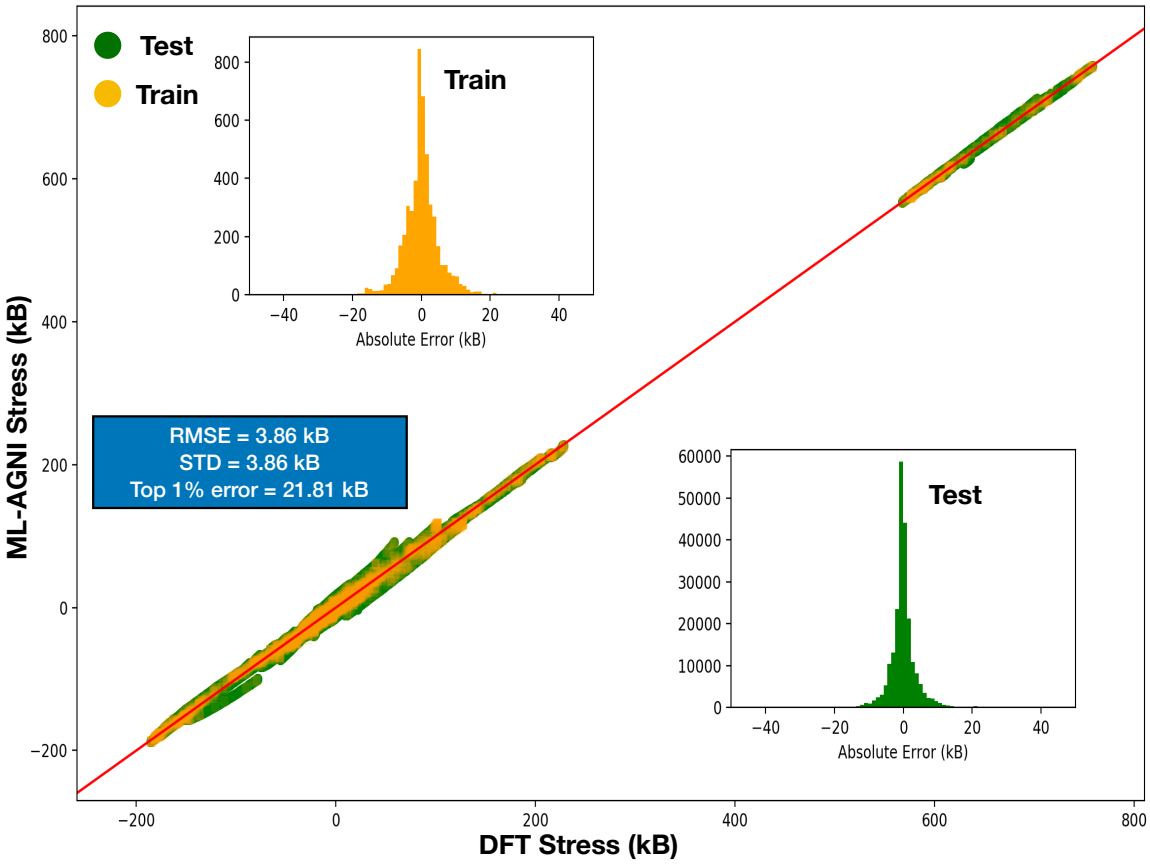

Figure A.3: Parity plot representing the ML model's stress tensor predictions on the DFT reference data for Copper. The plot is broken into the predictions made on the training (yellow), and test (green) data. Two of the inserted figures show a histogram of the absolute errors between ML and DFT for both the training and test set (colors correspond to those in the main plot). The third inset shows statistical metrics used to judge the model's performance versus DFT.

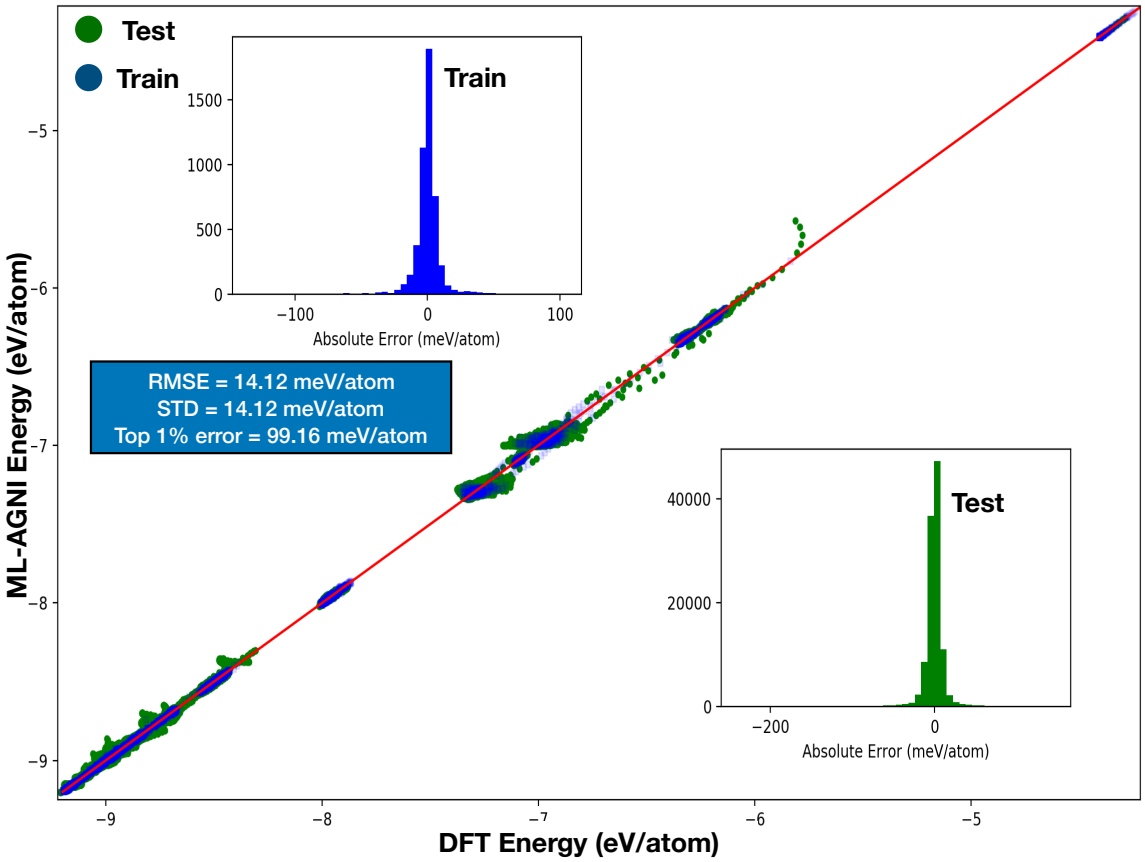

Figure A.4: Parity plot representing the ML model's potential energy predictions on the DFT reference data for Carbon. The plot is broken into the predictions made on the training (blue), and test (green) data. Two of the inserted figures show a histogram of the absolute errors between ML and DFT for both the training and test set (colors correspond to those in the main plot). The third inset shows statistical metrics used to judge the model's performance versus DFT.

APPENDIX B

THEORETICAL DETAILS REGARDING THE EMBEDDED ATOM METHOD

The underlying principle that embodies the EAM methodology is the idea that the cohesive energy of a configuration of atoms can be represented as the sum of atomic embedding energies [76]. This notion stems from the physics of the jellium model [320], in which at any arbitrary point in space, an object encounters a uniform electron density as well as the uniform distribution of atomic nuclei. For a metallic system, the embedding energies were combined with an electrostatic term [321], effectively making each atom in the system embedded into an electron gas that arises from all other atoms. Therefore, different atomic environments would encounter different electron density profiles, making such a method extremely transferable to a multitude of atomic configurations.

The EAM representation of the cohesive energy is generally defined as:

$$E_{coh} = \sum_i G_i \left(\sum_{j \neq i} \rho_j^a(R_{ij}) \right) + \frac{1}{2} \sum_{i,j \neq i} U_{ij}(R_{ij}) + E_{error} \tag{B.1}$$

Where G_i represents the combined effects of the kinetic, exchange, and correlation energies. This term can be represented as $G_i(\bar{\rho}) = G[\rho_i^a + \bar{\rho}_i] - G[\rho_i^a] - G[\bar{\rho}_i]$, with $\bar{\rho}_i$ representing some constant electron density around an embedded atom. $\rho_j^a(R_{ij})$ is the contribution to the total electron density embedded atom i encounters from atom j. $U_{ij}(R_{ij})$ is an electrostatic term embedded atom i encounters from atom j. E_{error} is defined as the error in the background density $\bar{\rho}_i$.

Generally the embedding function is represented semi-empirically through several tunable parameters such as the lattice parameter, cohesive energy, elastic constants, and the vacancy formation energy [76]. Generally, these properties are chosen as they explicitly determine the many-body interactions encountered within a material. There are many ap-

proaches one can take to represent the embedding functions, including the interpolation of splines or the use of analytic functional forms. In any case, the flexibility provided by the embedding functions allows for one to tailor the overall fit to the application at hand. However, this flexibility comes with drawbacks, as discussed throughout the main text.

REFERENCES

[1] A. Manthiram, "Materials challenges and opportunities of lithium ion batteries," *The Journal of Physical Chemistry Letters*, vol. 2, no. 3, pp. 176–184, 2011. eprint: https://doi.org/10.1021/jz1015422.

[2] W. Ashraf, "Carbonation of cement-based materials: Challenges and opportunities," *Construction and Building Materials*, vol. 120, pp. 558 –570, 2016.

[3] D. Maroudas, "Multiscale modeling of hard materials: Challenges and opportunities for chemical engineering," *American Institute of Chemical Engineers. AIChE Journal*, vol. 46, no. 5, p. 878, May 2000, Copyright - Copyright American Institute of Chemical Engineers May 2000.

[4] Y. Xue, Y. Li, J. Zhang, Z. Liu, and Y. Zhao, "2d graphdiyne materials: Challenges and opportunities in energy field," *Science China Chemistry*, vol. 61, no. 7, pp. 765–786, 2018.

[5] P. Mohanty, K. K. Pant, and R. Mittal, "Hydrogen generation from biomass materials: Challenges and opportunities," *WIREs Energy and Environment*, vol. 4, no. 2, pp. 139–155, 2015. eprint: https://onlinelibrary.wiley.com/doi/pdf/10.1002/wene.111.

[6] A. Yadollahi and N. Shamsaei, "Additive manufacturing of fatigue resistant materials: Challenges and opportunities," *International Journal of Fatigue*, vol. 98, pp. 14 –31, 2017.

[7] P. C. RAY, H. YU, and P. P. FU, "Toxicity and environmental risks of nanomaterials: Challenges and future needs," *Journal of Environmental Science and Health, Part C*, vol. 27, no. 1, pp. 1–35, 2009. eprint: https://doi.org/10.1080/10590500802708267.

[8] T. Thomas, T. Bahadori, N. Savage, and K. Thomas, "Moving toward exposure and risk evaluation of nanomaterials: Challenges and future directions," *WIREs Nanomedicine and Nanobiotechnology*, vol. 1, no. 4, pp. 426–433, 2009. eprint: https://onlinelibrary.wiley.com/doi/pdf/10.1002/wnan.34.

[9] E.-K. Lim, T. Kim, S. Paik, S. Haam, Y.-M. Huh, and K. Lee, "Nanomaterials for theranostics: Recent advances and future challenges," *Chemical Reviews*, vol. 115, no. 1, pp. 327–394, 2015.

[10] C. N. R. Rao and A. K. Cheetham, "Science and technology of nanomaterials: Current status and future prospects," *J. Mater. Chem.*, vol. 11, pp. 2887–2894, 12 2001.

[11] Y. Zhao and C. Burda, "Development of plasmonic semiconductor nanomaterials with copper chalcogenides for a future with sustainable energy materials," *Energy Environ. Sci.*, vol. 5, pp. 5564–5576, 2 2012.

[12] A. D. Maynard and R. J. Aitken, "Assessing exposure to airborne nanomaterials: Current abilities and future requirements," *Nanotoxicology*, vol. 1, no. 1, pp. 26–41, 2007. eprint: https://doi.org/10.1080/17435390701314720.

[13] D. Chimene, D. L. Alge, and A. K. Gaharwar, "Two-dimensional nanomaterials for biomedical applications: Emerging trends and future prospects," *Advanced Materials*, vol. 27, no. 45, pp. 7261–7284, 2015. eprint: https://onlinelibrary.wiley.com/doi/pdf/10.1002/adma.201502422.

[14] F. Hossain, O. J. Perales-Perez, S. Hwang, and F. Román, "Antimicrobial nanomaterials as water disinfectant: Applications, limitations and future perspectives," *Science of The Total Environment*, vol. 466-467, pp. 1047 –1059, 2014.

[15] L. J. Brennan, M. T. Byrne, M. Bari, and Y. K. Gun'ko, "Carbon nanomaterials for dye-sensitized solar cell applications: A bright future," *Advanced Energy Materials*, vol. 1, no. 4, pp. 472–485, 2011. eprint: https://onlinelibrary.wiley.com/doi/pdf/10.1002/aenm.201100136.

[16] J. K. Nørskov, F. Abild-Pedersen, F. Studt, and T. Bligaard, "Density functional theory in surface chemistry and catalysis," *Proceedings of the National Academy of Sciences*, vol. 108, no. 3, pp. 937–943, 2011. eprint: https://www.pnas.org/content/108/3/937.full.pdf.

[17] C. Guillaume, E. Gregoryanz, O. Degtyareva, M. McMahon, M. Hanfland, S. Evans, M. Guthrie, S. Sinogeikin, and H. Mao, "Cold melting and solid structures of dense lithium," *Nature Physics*, vol. 7, 2011.

[18] M. Buehler, *Atomistic Modeling of Materials Failure*. 2008.

[19] A. J. Cohen, P. Mori-Sánchez, and W. Yang, "Insights into current limitations of density functional theory," *Science*, vol. 321, no. 5890, pp. 792–794, 2008. eprint: https://science.sciencemag.org/content/321/5890/792.full.pdf.

[20] W. G. HOOVER and C. G. HOOVER, "Links between microscopic and macroscopic fluid mechanics," *Molecular Physics*, vol. 101, no. 11, pp. 1559–1573, 2003. eprint: https://doi.org/10.1080/0026897021000026647.

[21] J. Zyss and J. L. Oudar, "Relations between microscopic and macroscopic lowest-order optical nonlinearities of molecular crystals with one- or two-dimensional units," *Phys. Rev. A*, vol. 26, pp. 2028–2048, 4 1982.

[22] J. L. Lebowitz, "Microscopic origins of irreversible macroscopic behavior," *Physica A: Statistical Mechanics and its Applications*, vol. 263, no. 1, pp. 516 –527, 1999, Proceedings of the 20th IUPAP International Conference on Statistical Physics.

[23] J. Chapman, R. Batra, B. Uberuaga, G. Pilania, and R. Ramprasad, "A comprehensive computational study of adatom diffusion on the aluminum (100) surface," *Computational Materials Science*, vol. 158, pp. 353 –358, 2019.

[24] B. Wirth, K. Nordlund, D. Whyte, and D. Xu, "Fusion materials modeling: Challenges and opportunities," *MRS Bulletin*, vol. 36, no. 3, 216–222, 2011.

[25] A. Kawamoto, J. Jameson, Kyeongjae Cho, and R. W. Dutton, "Challenges for atomic scale modeling in alternative gate stack engineering," *IEEE Transactions on Electron Devices*, vol. 47, no. 10, pp. 1787–1794, 2000.

[26] M. Sitti and H. Hashimoto, "Controlled pushing of nanoparticles: Modeling and experiments," *IEEE/ASME Transactions on Mechatronics*, vol. 5, no. 2, pp. 199–211, 2000.

[27] E. A. Carter, "Challenges in modeling materials properties without experimental input," *Science*, vol. 321, no. 5890, pp. 800–803, 2008. eprint: `https://science.sciencemag.org/content/321/5890/800.full.pdf`.

[28] M. F. Lensink, S. Velankar, M. Baek, L. Heo, C. Seok, and S. J. Wodak, "The challenge of modeling protein assemblies: The casp12-capri experiment," *Proteins: Structure, Function, and Bioinformatics*, vol. 86, no. S1, pp. 257–273, 2018. eprint: `https://onlinelibrary.wiley.com/doi/pdf/10.1002/prot.25419`.

[29] R. O. Jones, "Density functional theory: Its origins, rise to prominence, and future," *Rev. Mod. Phys.*, vol. 87, pp. 897–923, 2015.

[30] H. Rafii-Tabar, "Computational modelling of thermo-mechanical and transport properties of carbon nanotubes," *Physics Reports*, vol. 390, no. 4, pp. 235 –452, 2004.

[31] A. Crocker, P. Flewitt, and G. Smith, "Computational modelling of fracture in polycrystalline materials," *International Materials Reviews*, vol. 50, no. 2, pp. 99–125, 2005. eprint: `https://doi.org/10.1179/174328005X14285`.

[32] D. D. Vvedensky, "Multiscale modelling of nanostructures," *Journal of Physics: Condensed Matter*, vol. 16, no. 50, R1537–R1576, 2004.

[33] M. Kireitseu, V. Kompis, H. Altenbach, V. Bochkareva, D. Hui, and S. Eremeev, "Continuum mechanics approach and computational modelling of submicrocrystalline and nanoscale materials," *Fullerenes, Nanotubes and Carbon Nanostructures*, vol. 13, no. 4, pp. 313–329, 2005. eprint: https://doi.org/10.1080/15363830500237176.

[34] K. Burke, J. Werschnik, and E. K. U. Gross, "Time-dependent density functional theory: Past, present, and future," *The Journal of Chemical Physics*, vol. 123, no. 6, p. 062 206, 2005. eprint: https://doi.org/10.1063/1.1904586.

[35] K. Burke, "Perspective on density functional theory," *The Journal of Chemical Physics*, vol. 136, no. 15, p. 150 901, 2012. eprint: https://doi.org/10.1063/1.4704546.

[36] A. D. Becke, "Perspective: Fifty years of density-functional theory in chemical physics," *The Journal of Chemical Physics*, vol. 140, no. 18, 18A301, 2014. eprint: https://doi.org/10.1063/1.4869598.

[37] R. G. Parr, "Density functional theory of atoms and molecules," in *Horizons of Quantum Chemistry*, K. Fukui and B. Pullman, Eds., Dordrecht: Springer Netherlands, 1980, pp. 5–15, ISBN: 978-94-009-9027-2.

[38] P. Hohenberg and W. Kohn, "Inhomogeneous electron gas," *Phys. Rev.*, vol. 136, B864–B871, 1964.

[39] L. Kohn W.; Sham, "Self-consistent equations including exchange and correlation effects," *Phys. Rev.*, vol. 140, A1133–A1138, 1965.

[40] J. Hafner, C. Wolverton, and G. Ceder, "Toward computational materials design: The impact of density functional theory on materials research," *MRS Bulletin*, vol. 31, no. 9, 659–668, 2006.

[41] M. D. Towler, A. Zupan, and M. Causà, "Density functional theory in periodic systems using local gaussian basis sets," *Computer Physics Communications*, vol. 98, no. 1, pp. 181 –205, 1996.

[42] M. Ljungberg, J. Mortensen, and L. Pettersson, "An implementation of core level spectroscopies in a real space projector augmented wave density functional theory code," *Journal of Electron Spectroscopy and Related Phenomena*, vol. 184, no. 8, pp. 427 –439, 2011.

[43] O. B. Malcıoğlu, R. Gebauer, D. Rocca, and S. Baroni, "Turbotddft – a code for the simulation of molecular spectra using the liouville–lanczos approach to time-dependent density-functional perturbation theory," *Computer Physics Communications*, vol. 182, no. 8, pp. 1744 –1754, 2011.

[44] D. R. Bowler and T Miyazaki, "Calculations for millions of atoms with density functional theory: Linear scaling shows its potential," *Journal of Physics: Condensed Matter*, vol. 22, no. 7, p. 074 207, 2010.

[45] D. M. Deaven and K. M. Ho, "Molecular geometry optimization with a genetic algorithm," *Phys. Rev. Lett.*, vol. 75, pp. 288–291, 2 1995.

[46] P. Pulay and G. Fogarasi, "Geometry optimization in redundant internal coordinates," *The Journal of Chemical Physics*, vol. 96, no. 4, pp. 2856–2860, 1992. eprint: https://doi.org/10.1063/1.462844.

[47] P. Császár and P. Pulay, "Geometry optimization by direct inversion in the iterative subspace," *Journal of Molecular Structure*, vol. 114, pp. 31 –34, 1984.

[48] H. B. Schlegel, "Geometry optimization," *WIREs Computational Molecular Science*, vol. 1, no. 5, pp. 790–809, 2011. eprint: https://onlinelibrary.wiley.com/doi/pdf/10.1002/wcms.34.

[49] B. Hartke, "Global geometry optimization of clusters using genetic algorithms," *The Journal of Physical Chemistry*, vol. 97, no. 39, pp. 9973–9976, 1993. eprint: https://doi.org/10.1021/j100141a013.

[50] M. von Arnim and R. Ahlrichs, "Geometry optimization in generalized natural internal coordinates," *The Journal of Chemical Physics*, vol. 111, no. 20, pp. 9183–9190, 1999. eprint: https://doi.org/10.1063/1.479510.

[51] F. Maseras and K. Morokuma, "Imomm: A new integrated ab initio + molecular mechanics geometry optimization scheme of equilibrium structures and transition states," *Journal of Computational Chemistry*, vol. 16, no. 9, pp. 1170–1179, 1995. eprint: https://onlinelibrary.wiley.com/doi/pdf/10.1002/jcc.540160911.

[52] J. McIver and A. Komornicki, "Rapid geometry optimization for semi-empirical molecular orbital methods," *Chemical Physics Letters*, vol. 10, no. 3, pp. 303 –306, 1971.

[53] G. Kresse and J. Hafner, "Ab initio molecular dynamics for liquid metals," *Phys. Rev. B*, vol. 47, pp. 558–561, 1 1993.

[54] J. C. Tully, "Molecular dynamics with electronic transitions," *The Journal of Chemical Physics*, vol. 93, no. 2, pp. 1061–1071, 1990. eprint: https://doi.org/10.1063/1.459170.

[55] M. Karplus and J. A. McCammon, "Molecular dynamics simulations of biomolecules," *Nature Structural Biology*, vol. 9, no. 9, pp. 646–652, 2002.

[56] S. Nosé and M. Klein, "Constant pressure molecular dynamics for molecular systems," *Molecular Physics*, vol. 50, no. 5, pp. 1055–1076, 1983. eprint: https://doi.org/10.1080/00268978300102851.

[57] G. J. Martyna, D. J. Tobias, and M. L. Klein, "Constant pressure molecular dynamics algorithms," *The Journal of Chemical Physics*, vol. 101, no. 5, pp. 4177–4189, 1994. eprint: https://doi.org/10.1063/1.467468.

[58] B. J. Alder and T. E. Wainwright, "Studies in molecular dynamics. i. general method," *The Journal of Chemical Physics*, vol. 31, no. 2, pp. 459–466, 1959. eprint: https://doi.org/10.1063/1.1730376.

[59] J. H. Thurtell and G. W. Thurtell, "Adsorption and diffusion at rough surfaces: A comparison of statistical mechanics, molecular dynamics, and kinetic theory," *The Journal of Chemical Physics*, vol. 88, no. 10, pp. 6641–6646, 1988. eprint: https://doi.org/10.1063/1.454452.

[60] J. Cao and G. A. Voth, "The formulation of quantum statistical mechanics based on the feynman path centroid density. iv. algorithms for centroid molecular dynamics," *The Journal of Chemical Physics*, vol. 101, no. 7, pp. 6168–6183, 1994. eprint: https://doi.org/10.1063/1.468399.

[61] P Español and P Warren, "Statistical mechanics of dissipative particle dynamics," *Europhysics Letters (EPL)*, vol. 30, no. 4, pp. 191–196, 1995.

[62] J. Wu, "Density functional theory for chemical engineering: From capillarity to soft materials," *AIChE Journal*, vol. 52, no. 3, pp. 1169–1193, 2006. eprint: https://aiche.onlinelibrary.wiley.com/doi/pdf/10.1002/aic.10713.

[63] D. W. Oxtoby, "Density functional methods in the statistical mechanics of materials," *Annual Review of Materials Research*, vol. 32, no. 1, pp. 39–52, 2002. eprint: https://doi.org/10.1146/annurev.matsci.32.100401.103425.

[64] R. O. Jones, "Density functional theory: Its origins, rise to prominence, and future," *Rev. Mod. Phys.*, vol. 87, pp. 897–923, 3 2015.

[65] A. J. Cohen, P. Mori-Sánchez, and W. Yang, "Challenges for density functional theory," *Chemical Reviews*, vol. 112, no. 1, pp. 289–320, 2012, PMID: 22191548. eprint: https://doi.org/10.1021/cr200107z.

[66] V. Karasiev and S. Trickey, "Issues and challenges in orbital-free density functional calculations," *Computer Physics Communications*, vol. 183, no. 12, pp. 2519 – 2527, 2012.

[67] N. Nakatsuji, "Cluster expansion of the wavefunction. excited states," *Chemical Physics Letters*, vol. 59, no. 2, pp. 362 –364, 1978.

[68] M. H. F. Sluiter and Y. Kawazoe, "Cluster expansion method for adsorption: Application to hydrogen chemisorption on graphene," *Phys. Rev. B*, vol. 68, p. 085 410, 8 2003.

[69] A. Seko, Y. Koyama, and I. Tanaka, "Cluster expansion method for multicomponent systems based on optimal selection of structures for density-functional theory calculations," *Phys. Rev. B*, vol. 80, p. 165 122, 16 2009.

[70] H. Nakatsuji and K. Hirao, "Cluster expansion of the wavefunction. symmetry-adapted-cluster expansion, its variational determination, and extension of open-shell orbital theory," *The Journal of Chemical Physics*, vol. 68, no. 5, pp. 2053–2065, 1978. eprint: https://doi.org/10.1063/1.436028.

[71] A. F. Oliveira, G. Seifert, T. Heine, and H. A. A. Duarte, "Density-functional based tight-binding: an approximate DFT method," *Journal of the Brazilian Chemical Society*, vol. 20, pp. 1193 –1205, 2009.

[72] G. Seifert, "Tight-binding density functional theory: an approximate kohnsham dft scheme," *The Journal of Physical Chemistry A*, vol. 111, no. 26, pp. 5609–5613, 2007, PMID: 17439198. eprint: https://doi.org/10.1021/jp069056r.

[73] K. Koura and H. Matsumoto, "Variable soft sphere molecular model for inverse-power-law or lennard-jones potential," *Physics of Fluids A: Fluid Dynamics*, vol. 3, no. 10, pp. 2459–2465, 1991. eprint: https://doi.org/10.1063/1.858184.

[74] A. P. Sutton and J. Chen, "Long-range finnis–sinclair potentials," *Philosophical Magazine Letters*, vol. 61, no. 3, pp. 139–146, 1990. eprint: https://doi.org/10.1080/09500839008206493.

[75] R. A. Johnson, "Alloy models with the embedded-atom method," *Phys. Rev. B*, vol. 39, pp. 12 554–12 559, 17 1989.

[76] M. S. Daw, S. M. Foiles, and M. I. Baskes, "The embedded-atom method: A review of theory and applications," *Materials Science Reports*, vol. 9, no. 7, pp. 251 –310, 1993.

[77] T. P. Senftle, S. Hong, M. M. Islam, S. B. Kylasa, Y. Zheng, Y. K. Shin, C. Junkermeier, R. Engel-Herbert, M. J. Janik, H. M. Aktulga, T. Verstraelen, A. Grama, and A. C. T. van Duin, "The reaxff reactive force-field: Development, applications and future directions," *npj Computational Materials*, vol. 2, no. 1, p. 15 011, 2016.

[78] R. E. Caflisch, "Monte carlo and quasi-monte carlo methods," *Acta Numerica*, vol. 7, 1–49, 1998.

[79] A. Stirling, M. Iannuzzi, A. Laio, and M. Parrinello, "Azulene-to-naphthalene rearrangement: The car–parrinello metadynamics method explores various reaction mechanisms," *ChemPhysChem*, vol. 5, no. 10, pp. 1558–1568, 2004. eprint: https://chemistry-europe.onlinelibrary.wiley.com/doi/pdf/10.1002/cphc.200400063.

[80] X. Biarnés, S. Bongarzone, A. V. Vargiu, P. Carloni, and P. Ruggerone, "Molecular motions in drug design: The coming age of the metadynamics method," *Journal of Computer-Aided Molecular Design*, vol. 25, no. 5, pp. 395–402, 2011.

[81] H. Li, D. Min, Y. Liu, and W. Yang, "Essential energy space random walk via energy space metadynamics method to accelerate molecular dynamics simulations," *The Journal of Chemical Physics*, vol. 127, no. 9, p. 094 101, 2007. eprint: https://doi.org/10.1063/1.2769356.

[82] D. Hamelberg, J. Mongan, and J. A. McCammon, "Accelerated molecular dynamics: A promising and efficient simulation method for biomolecules," *The Journal of Chemical Physics*, vol. 120, no. 24, pp. 11 919–11 929, 2004. eprint: https://doi.org/10.1063/1.1755656.

[83] J. A. Board, J. W. Causey, J. F. Leathrum, A. Windemuth, and K. Schulten, "Accelerated molecular dynamics simulation with the parallel fast multipole algorithm," *Chemical Physics Letters*, vol. 198, no. 1, pp. 89 –94, 1992.

[84] A. F. Voter, "Hyperdynamics: Accelerated molecular dynamics of infrequent events," *Phys. Rev. Lett.*, vol. 78, pp. 3908–3911, 20 1997.

[85] R. E. Rudd and J. Q. Broughton, "Coarse-grained molecular dynamics and the atomic limit of finite elements," *Phys. Rev. B*, vol. 58, R5893–R5896, 10 1998.

[86] ——, "Coarse-grained molecular dynamics: Nonlinear finite elements and finite temperature," *Phys. Rev. B*, vol. 72, p. 144 104, 14 2005.

[87] T. Aoyagi, F. Sawa, T. Shoji, H. Fukunaga, J. ichi Takimoto, and M. Doi, "A general-purpose coarse-grained molecular dynamics program," *Computer Physics Communications*, vol. 145, no. 2, pp. 267 –279, 2002.

[88] N. A. Benedek, A. L.-S. Chua, C. Elsässer, A. P. Sutton, and M. W. Finnis, "Interatomic potentials for strontium titanate: An assessment of their transferability and comparison with density functional theory," *Phys. Rev. B*, vol. 78, p. 064 110, 6 2008.

[89] A. Tveito, K. H. Jæger, G. T. Lines, Paszkowski, J. Sundnes, A. G. Edwards, T. Māki-Marttunen, G. Halnes, and G. T. Einevoll, "An evaluation of the accuracy of classical models for computing the membrane potential and extracellular potential for neurons," *Frontiers in Computational Neuroscience*, vol. 11, p. 27, 2017.

[90] Z Li and H. A. Scheraga, "Monte carlo-minimization approach to the multiple-minima problem in protein folding," *Proceedings of the National Academy of Sciences*, vol. 84, no. 19, pp. 6611–6615, 1987. eprint: `https://www.pnas.org/content/84/19/6611.full.pdf`.

[91] U. H. Hansmann and Y. Okamoto, "New monte carlo algorithms for protein folding," *Current Opinion in Structural Biology*, vol. 9, no. 2, pp. 177 –183, 1999.

[92] E. Shakhnovich, G. Farztdinov, A. M. Gutin, and M. Karplus, "Protein folding bottlenecks: A lattice monte carlo simulation," *Phys. Rev. Lett.*, vol. 67, pp. 1665–1668, 12 1991.

[93] F. B. Brown, R. D. Mosteller, and W. R. Martin, *Monte Carlo - Advances and Challenges*. Switzerland: Paul Scherrer Institut - PSI, 2008, ISBN: 978-3-9521409-5-6.

[94] X. Wu, X. Zhu, G. Wu, and W. Ding, "Data mining with big data," *IEEE Transactions on Knowledge and Data Engineering*, vol. 26, no. 1, pp. 97–107, 2014.

[95] M. Chen, S. Mao, and Y. Liu, "Big data: A survey," *Mobile Networks and Applications*, vol. 19, no. 2, pp. 171–209, 2014.

[96] M. Richardson, A. Prakash, and E. Brill, "Beyond pagerank: Machine learning for static ranking," in *Proceedings of the 15th International Conference on World Wide Web*, ser. WWW '06, Edinburgh, Scotland: Association for Computing Machinery, 2006, 707–715, ISBN: 1595933239.

[97] A. K. McCallum, K. Nigam, J. Rennie, and K. Seymore, "Automating the construction of internet portals with machine learning," *Information Retrieval*, vol. 3, no. 2, pp. 127–163, 2000.

[98] T. Joachims and F. Radlinski, "Search engines that learn from implicit feedback," *Computer*, vol. 40, no. 8, pp. 34–40, 2007.

[99] Taichi Joutou and Keiji Yanai, "A food image recognition system with multiple kernel learning," in *2009 16th IEEE International Conference on Image Processing (ICIP)*, 2009, pp. 285–288.

[100] N. E. Ayat, M. Cheriet, L. Remaki, and C. Y. Suen, "Kmod - a new support vector machine kernel with moderate decreasing for pattern recognition. application

to digit image recognition," in *Proceedings of Sixth International Conference on Document Analysis and Recognition*, 2001, pp. 1215–1219.

[101] B. Zoph, V. Vasudevan, J. Shlens, and Q. V. Le, "Learning transferable architectures for scalable image recognition," in *The IEEE Conference on Computer Vision and Pattern Recognition (CVPR)*, 2018.

[102] M. Bojarski, D. D. Testa, D. Dworakowski, B. Firner, B. Flepp, P. Goyal, L. D. Jackel, M. Monfort, U. Muller, J. Zhang, X. Zhang, J. Zhao, and K. Zieba, *End to end learning for self-driving cars*, 2016. arXiv: 1604.07316 [cs.CV].

[103] J. Kim and J. Canny, "Interpretable learning for self-driving cars by visualizing causal attention," in *The IEEE International Conference on Computer Vision (ICCV)*, 2017.

[104] M. Martinez, C. Sitawarin, K. Finch, L. Meincke, A. Yablonski, and A. Kornhauser, *Beyond grand theft auto v for training, testing and enhancing deep learning in self driving cars*, 2017. arXiv: 1712.01397 [cs.CV].

[105] R. Ramprasad, R. Batra, G. Pilania, A. Mannodi-Kanakkithodi, and C. Kim, "Machine learning and materials informatics: Recent applications and prospects," *npj Comput. Mater.*, vol. 54, 2017.

[106] A. Radovic, M. Williams, D. Rousseau, M. Kagan, D. Bonacorsi, A. Himmel, A. Aurisano, K. Terao, and T. Wongjirad, "Machine learning at the energy and intensity frontiers of particle physics," *Nature*, vol. 560, no. 7716, pp. 41–48, 2018.

[107] J. Gasteiger and J. Zupan, "Neural networks in chemistry," *Angew. Chem. Int. Ed.*, vol. 32, pp. 503–527, 1993.

[108] B. G. Sumpter, C. Getino, and D. W. Noid, "Theory and applications of neural computing in chemical science," *Annu. Rev. Phys. Chem.*, vol. 45, pp. 439–481, 1994.

[109] K. Rajan, "Materials informatics," *Mater. Today*, vol. 8, pp. 38–45, 2005.

[110] A. Mannodi-Kanakkithodi, A. Chandrasekaran, C. Kim, T. D. Huan, G. Pilania, V. Botu, and R. Ramprasad, "Scoping the polymer genome: A roadmap for rational polymer dielectrics design and beyond," *Mater. Today*, vol. 21, pp. 785–796, 2017.

[111] C. Kim, A. Chandrasekaran, T. D. Huan, D. Das, and R. Ramprasad, "Polymer genome: A data-powered polymer informatics platform for property predictions," *J. Phys. Chem. C*, vol. 122, pp. 17 575–17 585, 2018.

[112] G. Pilania, C. Wang, X. Jiang, S. Rajasekaran, and R Ramprasad, "Accelerating materials property predictions using machine learning," *Sci. Rep.*, vol. 3, p. 2810, 2018.

[113] T. D. Huan, A. Mannodi-Kanakkithodi, and R. Ramprasad, "Accelerated materials property predictions and design using motif-based fingerprints," *Phys. Rev. B*, vol. 92, 2015.

[114] A. Mannodi-Kanakkithodi, G. Pilania, T. D. Huan, T. Lookman, and R. Ramprasad, "Machine learning strategy for the accelerated design of polymer dielectrics," *Sci. Rep.*, vol. 6, p. 20 952, 2016.

[115] N. Artrith, A. Urban, and G. Ceder, "Constructing first-principles phase diagrams of amorphous lixsi using machine-learning-assisted sampling with an evolutionary algorithm," *The Journal of Chemical Physics*, vol. 148, no. 24, p. 241 711, 2018. eprint: https://doi.org/10.1063/1.5017661.

[116] Z. W. Ulissi, A. R. Singh, C. Tsai, and J. K. Nørskov, "Automated discovery and construction of surface phase diagrams using machine learning," *The Journal of Physical Chemistry Letters*, vol. 7, no. 19, pp. 3931–3935, 2016, PMID: 27558978. eprint: https://doi.org/10.1021/acs.jpclett.6b01254.

[117] J Behler, "Atom-centered symmetry functions for constructing high-dimensional neural network potentials," *J. Chem. Phys*, vol. 134, 2011.

[118] V. Botu and R. Ramprasad, "Adaptive machine learning framework to accelerate ab initio molecular dynamics," *Int. J. Quant. Chem.*, vol. 115, pp. 1074–1083, 2015.

[119] A. P. Bartók, M. C. Payne, R. Kondor, and G. Csányi, "Gaussian approximation potentials: The accuracy of quantum mechanics, without the electrons," *Phys. Rev. Lett.*, vol. 104, p. 136 403, 13 2010.

[120] K. Xia, H. Gao, C. Liu, J. Yuan, J. Sun, H.-T. Wang, and D. Xing, "A novel superhard tungsten nitride predicted by machine-learning accelerated crystal structure search," *Science Bulletin*, vol. 63, no. 13, pp. 817 –824, 2018.

[121] B. Meredig, A. Agrawal, S. Kirklin, J. E. Saal, J. W. Doak, A. Thompson, K. Zhang, A. Choudhary, and C. Wolverton, "Combinatorial screening for new materials in unconstrained composition space with machine learning," *Phys. Rev. B*, vol. 89, p. 094 104, 9 2014.

[122] I. M. Mosa, S. Biswas, A. M. El-Sawy, V. Botu, C. Guild, W. Song, R. Ramprasad, J. F. Rusling, and S. L. Suib, "Tunable mesoporous manganese oxide for high performance oxygen reduction and evolution reactions," *J. Mater. Chem. A*, vol. 4, pp. 620–631, 2 2016.

[123] V. Botu, R. Ramprasad, and A. B. Mhadeshwar, "Ceria in an oxygen environment: Surface phase equilibria and its descriptors," *Surface Science*, vol. 619, pp. 49 –58, 2014.

[124] V. Botu, A. B. Mhadeshwar, S. L. Suib, and R. Ramprasad, "Optimal dopant selection for water splitting with cerium oxides: Mining and screening first principles data," in *Information Science for Materials Discovery and Design*, T. Lookman, F. J. Alexander, and K. Rajan, Eds. Cham: Springer International Publishing, 2016, pp. 157–171, ISBN: 978-3-319-23871-5.

[125] T. B. Blank, S. D. Brown, A. W. Calhoun, and D. J. Doren, "Neural network models of potential energy surfaces," *The Journal of Chemical Physics*, vol. 103, no. 10, pp. 4129–4137, 1995. eprint: https://doi.org/10.1063/1.469597.

[126] H. Gassner, M. Probst, A. Lauenstein, and K. Hermansson, "Representation of intermolecular potential functions by neural networks," *The Journal of Physical Chemistry A*, vol. 102, no. 24, pp. 4596–4605, 1998. eprint: https://doi.org/10.1021/jp972209d.

[127] S. Lorenz, A. Groß, and M. Scheffler, "Representing high-dimensional potential-energy surfaces for reactions at surfaces by neural networks," *Chemical Physics Letters*, vol. 395, no. 4, pp. 210 –215, 2004.

[128] J. Behler and M. Parrinello, "Generalized neural-network representation of high-dimensional potential-energy surfaces," *Phys. Rev. Lett.*, vol. 98, p. 146 401, 2007.

[129] J. C. Thomas, J. S. Bechtel, A. R. Natarajan, and A. Van der Ven, "Machine learning the density functional theory potential energy surface for the inorganic halide perovskite cspbbr3," *Phys. Rev. B*, vol. 100, p. 134 101, 13 2019.

[130] N. Artrith and A. Urban, "An implementation of artificial neural-network potentials for atomistic materials simulations: Performance for tio2," *Computational Materials Science*, vol. 114, pp. 135 –150, 2016.

[131] B. Jiang and H. Guo, "Permutation invariant polynomial neural network approach to fitting potential energy surfaces," *The Journal of Chemical Physics*, vol. 139, no. 5, p. 054 112, 2013. eprint: https://doi.org/10.1063/1.4817187.

[132] A. Thompson, L. Swiler, C. Trott, S. Foiles, and G. Tucker, "Spectral neighbor analysis method for automated generation of quantum-accurate interatomic potentials," *Journal of Computational Physics*, vol. 285, pp. 316 –330, 2015.

[133] A. V. Shapeev, "Moment tensor potentials: A class of systematically improvable interatomic potentials," *Multiscale Modeling Simulation*, vol. 14, no. 3, 1153–1173, 2016.

[134] A. Glielmo, C. Zeni, and A. De Vita, "Efficient nonparametric *n*-body force fields from machine learning," *Phys. Rev. B*, vol. 97, p. 184 307, 18 2018.

[135] K. Hansen, F. Biegler, R. Ramakrishnan, W. Pronobis, O. A. von Lilienfeld, K.-R. Müller, and A. Tkatchenko, "Machine learning predictions of molecular properties: Accurate many-body potentials and nonlocality in chemical space," *The Journal of Physical Chemistry Letters*, vol. 6, no. 12, pp. 2326–2331, 2015, PMID: 26113956. eprint: https://doi.org/10.1021/acs.jpclett.5b00831.

[136] P. O. Dral, A. Owens, S. N. Yurchenko, and W. Thiel, "Structure-based sampling and self-correcting machine learning for accurate calculations of potential energy surfaces and vibrational levels," *The Journal of Chemical Physics*, vol. 146, no. 24, p. 244 108, 2017. eprint: https://doi.org/10.1063/1.4989536.

[137] V. Botu and R. Ramprasad, "Learning scheme to predict atomic forces and accelerate materials simulations," *Phys. Rev. B*, vol. 92, p. 094 306, 2015.

[138] M. Rupp, R. Ramakrishnan, and O. A. von Lilienfeld, "Machine learning for quantum mechanical properties of atoms in molecules," *The Journal of Physical Chemistry Letters*, vol. 6, no. 16, pp. 3309–3313, 2015. eprint: https://doi.org/10.1021/acs.jpclett.5b01456.

[139] A. Glielmo, P. Sollich, and A. De Vita, "Accurate interatomic force fields via machine learning with covariant kernels," *Phys. Rev. B*, vol. 95, p. 214 302, 21 2017.

[140] S. Chmiela, A. Tkatchenko, H. E. Sauceda, I. Poltavsky, K. T. Schütt, and K.-R. Müller, "Machine learning of accurate energy-conserving molecular force fields," vol. 3, no. 5, 2017.

[141] L. D. Landau and E. M. Lifschitz, *Quantum mechanics*. German Democratic Republic: Akademie Verlag, 1988.

[142] J. M. Combes, P. Duclos, and R. Seiler, "The born-oppenheimer approximation," in *Rigorous Atomic and Molecular Physics*, G. Velo and A. S. Wightman, Eds. Boston, MA: Springer US, 1981, pp. 185–213, ISBN: 978-1-4613-3350-0.

[143] E. Nelson, "Derivation of the schrödinger equation from newtonian mechanics," *Phys. Rev.*, vol. 150, pp. 1079–1085, 4 1966.

[144] T. Liszka and J. Orkisz, "The finite difference method at arbitrary irregular grids and its application in applied mechanics," *Computers Structures*, vol. 11, no. 1, pp. 83 –95, 1980, Special Issue-Computational Methods in Nonlinear Mechanics.

[145] R. E. Stanton, "Hellmann-feynman theorem and correlation energies," *The Journal of Chemical Physics*, vol. 36, no. 5, pp. 1298–1300, 1962. eprint: https://doi.org/10.1063/1.1732731.

[146] B. G. LIPPERT, J. HUTTER, and M. PARRINELLO, "A hybrid gaussian and plane wave density functional scheme," *Molecular Physics*, vol. 92, no. 3, pp. 477–488, 1997. eprint: https://doi.org/10.1080/002689797170220.

[147] E. J. Bylaska, K. Tsemekhman, S. B. Baden, J. H. Weare, and H. Jonsson, "Parallel implementation of -point pseudopotential plane-wave dft with exact exchange," *Journal of Computational Chemistry*, vol. 32, no. 1, pp. 54–69, 2011. eprint: https://onlinelibrary.wiley.com/doi/pdf/10.1002/jcc.21598.

[148] P. E. Blöchl, "Projector augmented-wave method," *Phys. Rev. B*, vol. 50, pp. 17 953–17 979, 24 1994.

[149] G. Kresse and D. Joubert, "From ultrasoft pseudopotentials to the projector augmented-wave method," *Phys. Rev. B*, vol. 59, pp. 1758–1775, 3 1999.

[150] J. P. Perdew, K. Burke, and M. Ernzerhof, "Generalized gradient approximation made simple," *Phys. Rev. Lett.*, vol. 77, pp. 3865–3868, 18 1996.

[151] M. Ernzerhof and G. E. Scuseria, "Assessment of the perdew–burke–ernzerhof exchange-correlation functional," *The Journal of Chemical Physics*, vol. 110, no. 11, pp. 5029–5036, 1999. eprint: https://doi.org/10.1063/1.478401.

[152] F Ercolessi and J. B Adams, "Interatomic potentials from first-principles calculations: The force-matching method," *Europhysics Letters (EPL)*, vol. 26, no. 8, pp. 583–588, 1994.

[153] S. K. Gray and J. S. Wright, "Classical trajectories for the h+h2 reaction on a spline-generated potential energy surface," *The Journal of Chemical Physics*, vol. 66, no. 7, pp. 2867–2873, 1977. eprint: https://doi.org/10.1063/1.434345.

[154] A. J. C. Varandas, F. B. Brown, C. A. Mead, D. G. Truhlar, and N. C. Blais, "A double many-body expansion of the two lowest-energy potential surfaces and nonadiabatic coupling for h3," *The Journal of Chemical Physics*, vol. 86, no. 11, pp. 6258–6269, 1987. eprint: https://doi.org/10.1063/1.452463.

[155] T.-S. Ho and H. Rabitz, "Reproducing kernel hilbert space interpolation methods as a paradigm of high dimensional model representations: Application to multidimensional potential energy surface construction," *The Journal of Chemical Physics*, vol. 119, no. 13, pp. 6433–6442, 2003. eprint: https://doi.org/10.1063/1.1603219.

[156] C. Crespos, M. A. Collins, E. Pijper, and G. J. Kroes, "Application of the modified shepard interpolation method to the determination of the potential energy surface for a molecule–surface reaction: H2+pt(111)," *The Journal of Chemical Physics*, vol. 120, no. 5, pp. 2392–2404, 2004. eprint: https://doi.org/10.1063/1.1637337.

[157] Z. Xie and J. M. Bowman, "Permutationally invariant polynomial basis for molecular energy surface fitting via monomial symmetrization," *Journal of Chemical Theory and Computation*, vol. 6, no. 1, pp. 26–34, 2010, PMID: 26614316. eprint: https://doi.org/10.1021/ct9004917.

[158] L. Li, J. C. Snyder, I. M. Pelaschier, J. Huang, U.-N. Niranjan, P. Duncan, M. Rupp, K.-R. Müller, and K. Burke, "Understanding machine-learned density functionals," *International Journal of Quantum Chemistry*, vol. 116, no. 11, pp. 819–833, 2016. eprint: https://onlinelibrary.wiley.com/doi/pdf/10.1002/qua.25040.

[159] J. C. Snyder, M. Rupp, K. Hansen, K.-R. Müller, and K. Burke, "Finding density functionals with machine learning," *Phys. Rev. Lett.*, vol. 108, p. 253 002, 25 2012.

[160] A. S. Christensen, F. A. Faber, and O. A. von Lilienfeld, "Operators in quantum machine learning: Response properties in chemical space," *The Journal of Chemical Physics*, vol. 150, no. 6, p. 064 105, 2019. eprint: https://doi.org/10.1063/1.5053562.

[161] A. Khorshidi and A. A. Peterson, "Amp: A modular approach to machine learning in atomistic simulations," *Computer Physics Communications*, vol. 207, pp. 310 –324, 2016.

[162] A. A. Peterson, R. Christensen, and A. Khorshidi, "Addressing uncertainty in atomistic machine learning," *Phys. Chem. Chem. Phys.*, vol. 19, pp. 10 978–10 985, 18 2017.

[163] S. Dick and M. Fernandez-Serra, "Learning from the density to correct total energy and forces in first principle simulations," *The Journal of Chemical Physics*, vol. 151, no. 14, p. 144 102, 2019. eprint: https://doi.org/10.1063/1.5114618.

[164] V. L. Deringer and G. Csányi, "Machine learning based interatomic potential for amorphous carbon," *Phys. Rev. B*, vol. 95, p. 094 203, 9 2017.

[165] T. D. Huan, R. Batra, J. Chapman, S. Krishnan, L. Chen, and R. Ramprasad, "A universal strategy for the creation of machine learning based atomistic force fields," *npj Comput. Mater.*, vol. 3, p. 37, 2017.

[166] J. Chapman, R. Batra, and R. Ramprasad, "Machine learning models for the prediction of energy, forces, and stresses for platinum," *Computational Materials Science*, vol. 174, p. 109 483, 2020.

[167] V. Botu, R. Batra, J. Chapman, and R. Ramprasad, "Machine learning force fields: Construction, validation, and outlook," *Jour. Phys. Chem. C*, vol. 121, pp. 511–522, 2017.

[168] T. D. Huan, R. Batra, J. Chapman, C. Kim, A. Chandrasekaran, and R. Ramprasad, "Iterative-learning strategy for the development of application-specific atomistic force fields," *The Journal of Physical Chemistry C*, vol. 0, no. ja, null, 0. eprint: https://doi.org/10.1021/acs.jpcc.9b04207.

[169] R. Batra, H. D. Tran, C. Kim, J. Chapman, L. Chen, A. Chandrasekaran, and R. Ramprasad, "General atomic neighborhood fingerprint for machine learning-based methods," *The Journal of Physical Chemistry C*, vol. 123, no. 25, pp. 15 859–15 866, 2019. eprint: https://doi.org/10.1021/acs.jpcc.9b03925.

[170] A. Chandrasekaran, D. Kamal, R. Batra, C. Kim, L. Chen, and R. Ramprasad, "Solving the electronic structure problem with machine learning," *npj Computational Materials*, vol. 5, no. 1, p. 22, 2019.

[171] ——, "Solving the electronic structure problem with machine learning," *npj Computational Materials*, vol. 5, no. 1, p. 22, 2019.

[172] V. Botu, J. Chapman, and R. Ramprasad, "A study of adatom ripening on an al (111) surface with machine learning force fields," *Comp. Mat. Sci.*, vol. 129, pp. 332–335, 2016.

[173] S. Wold, K. Esbensen, and P. Geladi, "Principal component analysis," *Chemometrics and Intelligent Laboratory Systems*, vol. 2, no. 1, pp. 37 –52, 1987, Proceedings of the Multivariate Statistical Workshop for Geologists and Geochemists.

[174] V. Vovk, "Kernel ridge regression," in *Empirical Inference: Festschrift in Honor of Vladimir N. Vapnik*, B. Schölkopf, Z. Luo, and V. Vovk, Eds. Berlin, Heidelberg: Springer Berlin Heidelberg, 2013, pp. 105–116, ISBN: 978-3-642-41136-6.

[175] M. H. Hassoun, *Fundamentals of Artificial Neural Networks*, 1st. Cambridge, MA, USA: MIT Press, 1995, ISBN: 026208239X.

[176] D. P. Kingma and J. Ba, *Adam: A method for stochastic optimization*, 2014. arXiv: 1412.6980 [cs.LG].

[177] S Plimpton, "Fast parallel algorithms for short-range molecular dynamics," *J. Compu. Phys.*, vol. 117, no. 1, pp. 1 –19, 1995.

[178] N. S. Martys and R. D. Mountain, "Velocity verlet algorithm for dissipative-particle-dynamics-based models of suspensions," *Phys. Rev. E*, vol. 59, pp. 3733–3736, 3 1999.

[179] J. V. Neumann, "Physical applications of the ergodic hypothesis," *Proceedings of the National Academy of Sciences of the United States of America*, vol. 18, no. 3, pp. 263–266, 1932, 16587674[pmid].

[180] S. Nosé, "A unified formulation of the constant temperature molecular dynamics methods," *The Journal of Chemical Physics*, vol. 81, no. 1, pp. 511–519, 1984. eprint: https://doi.org/10.1063/1.447334.

[181] D. J. Evans and B. L. Holian, "The nose–hoover thermostat," *The Journal of Chemical Physics*, vol. 83, no. 8, pp. 4069–4074, 1985. eprint: https://doi.org/10.1063/1.449071.

[182] Y. Mori and Y. Okamoto, "Generalized-ensemble algorithms for the isobaric–isothermal ensemble," *Journal of the Physical Society of Japan*, vol. 79, no. 7, p. 074 003, 2010. eprint: https://doi.org/10.1143/JPSJ.79.074003.

[183] M. F. Møller, "A scaled conjugate gradient algorithm for fast supervised learning," *Neural Networks*, vol. 6, no. 4, pp. 525 –533, 1993.

[184] H Jònsson, G Mills, and K. W. Jacobsen, "Nudged elastic band method for finding minimum energy paths of transitions," *Classical and Quantum Dynamics in Condensed Phase Simulations*, vol. 50, p. 385, 1998.

[185] H Jònsson and G. Henkelman, "Improved tangent estimate in the nudged elastic band method for finding minimum energy paths and saddle points," *J. Chem. Phys*, vol. 113, 2000.

[186] H Jònsson, G Henkelman, and B. Uberuaga, "A climbing image nudged elastic band method for finding saddle points and minimum energy paths," *J. Chem. Phys*, vol. 113, 2000.

[187] R. Johnson, A. Hultqvist, and S. Bent, "A brief review of atomic layer deposition: From fundamentals to applications," *Materials Today*, vol. 17, no. 5, pp. 236 –246, 2014.

[188] Z. Zhang and M. G. Lagally, "Atomistic processes in the early stages of thin-film growth," *Science*, vol. 276, no. 5311, pp. 377–383, 1997. eprint: http://science.sciencemag.org/content/276/5311/377.full.pdf.

[189] V. Recoules, P. Renaudin, J. Clérouin, P. Noiret, and G. Zérah, "Electrical conductivity of hot expanded aluminum: Experimental measurements and ab initio calculations," *Phys. Rev. E*, vol. 66, p. 056 412, 5 2002.

[190] J. Davis, "Corrosion of aluminum and aluminum alloys," *ASM International*, 1999.

[191] G. Scamans, N. Birbilis, and R. Buchheit, "Corrosion of aluminum and its alloys," in *Shreir's Corrosion*, T. Richardson, Ed., 1st ed. Netherlands: Elsevier, Dec. 2010, pp. 1974–2010, ISBN: 9870444527875.

[192] K. Klaiman, D. L. Ortega, and C. Garnache, "Consumer preferences and demand for packaging material and recyclability," *Resources, Conservation and Recycling*, vol. 115, pp. 1 –8, 2016.

[193] G. Liu and D. B. Müller, "Addressing sustainability in the aluminum industry: A critical review of life cycle assessments," *Journal of Cleaner Production*, vol. 35, pp. 108 –117, 2012.

[194] G Kresse and J Furthmüller, "Efficient iterative schemes for ab initio total energy calculations using a plane-wave basis set," *Phys. Rev. B*, vol. 54, 1996.

[195] G. Kresse and D. Joubert, "From ultrasoft pseudopotentials to the projector augmented wave method," *Phys. Rev. B*, vol. 59, 1999.

[196] J. P. Perdew, K. Burke, and Y Wang, "Generalized gradient approximation for the exchange-correlation hole of a many electron system," *Phys. Rev. B*, vol. 54, 1996.

[197] P. E Blöchl, "Projector augmented wave method," *Phys. Rev. B*, vol. 50, 1994.

[198] A Voter and S Chen, "Accurate interatomic potentials for ni, al, and ni3al," *Mater. Res. Soc.*, vol. 82, p. 175, 1987.

[199] X. Liu, F Ercolessi, and J. Adams, "Aluminium interatomic potential from density functional theory calculations with improved stacking fault energy," *Modell. Simul. Mater. Sci. Eng*, vol. 82, p. 175, 2004.

[200] R. Zope and Y Mishin, "Interatomic potentials for atomistic simulations of the ti-al system," *Phys. Rev. B*, vol. 68, 2003.

[201] G. Henkelman and H. Jònsson, "A dimer method for finding saddle points on high dimensional potential surfaces using only first derivatives," *J. Chem. Phys.*, vol. 111, pp. 7010–7022, 15 1999.

[202] ——, "Long time scale kinetic monte carlo simulations without lattice approximation and predefined event table," *J. Chem. Phys.*, vol. 115, pp. 9657–9666, 21 2001.

[203] J Wang, A Horsfield, P Lee, and P Brommer, "Heterogeneous nucleation of solid al from the melt by al3ti: Molecular dynamics simulations," *Phys. Rev. B*, vol. 82, 2010.

[204] E Levchenko, A Evteev, G Löwisch, I Belova, and G Murch, "Molecular dynamics simulation of alloying in a ti-coated al nanoparticle," *Intermetallics*, vol. 22, pp. 192,203, 20101.

[205] D Wales, "Energy landscapes: Calculating pathways and rates," *Int. Rev. in Phys. Chem.*, vol. 25, pp. 237–282, 2006.

[206] J Murdoch, "What is the rate-limiting step of a multistep reaction?" *Journal of Chem. Education*, vol. 58, pp. 32–36, 1 1981.

[207] J. Sun and S. Simon, "The melting behavior of aluminum nanoparticles," *Thermochimica Acta*, vol. 463, no. 1, pp. 32 –40, 2007, Chemical Thermodynamics and Thermal Analysis.

[208] R. M. Eastment and C. H. B. Mee, "Work function measurements on (100), (110) and (111) surfaces of aluminium," *Journal of Physics F: Metal Physics*, vol. 3, no. 9, pp. 1738–1745, 1973.

[209] P. Stoltze, J. K. Nørskov, and U. Landman, "Disordering and melting of aluminum surfaces," *Phys. Rev. Lett.*, vol. 61, pp. 440–443, 4 1988.

[210] L. Pedemonte, G. Bracco, A. Robin, and W. Heiland, "Residual order within the molten al(110) surface layer," *Phys. Rev. B*, vol. 65, p. 245 406, 24 2002.

[211] A. V. Fedorov, A. V. Shulgin, and S. A. Lavruk, "Description of melting of aluminum nanoparticles," *Combustion, Explosion, and Shock Waves*, vol. 52, no. 4, pp. 457–462, 2016.

[212] A. V. Fedorov and A. V. Shulgin, "Mathematical modeling of melting of nano-sized metal particles," *Combustion, Explosion, and Shock Waves*, vol. 47, no. 2, p. 147, 2011.

[213] A. Aguado and M. F. Jarrold, "Melting and freezing of metal clusters," *Annual Review of Physical Chemistry*, vol. 62, no. 1, pp. 151–172, 2011, PMID: 21128764. eprint: `https://doi.org/10.1146/annurev-physchem-032210-103454`.

[214] K. Tamaru, "In situ surface dynamics in heterogeneous catalysis," *Applied Catalysis A: General*, vol. 151, no. 1, pp. 167 –177, 1997, Transient Kinetics.

[215] H. Lüth, *Solid Surfaces, Interfaces and Thin Films; 5th ed.* Ser. Graduate Texts in Physics. Berlin, Heidelberg: Springer, 2010.

[216] I. V. Markov, *Crystal Growth for Beginners*, 3rd. WORLD SCIENTIFIC, 2017. eprint: https://www.worldscientific.com/doi/pdf/10.1142/10127.

[217] J. Lei and H. Ju, "Signal amplification using functional nanomaterials for biosensing," *Chem. Soc. Rev.*, vol. 41, pp. 2122–2134, 6 2012.

[218] G. Kellogg, T. Tsong, and P. Cowan, "Direct observation of surface diffusion and atomic interactions on metal surfaces," *Surface Science*, vol. 70, no. 1, pp. 485 – 519, 1978.

[219] G. L. Kellogg and P. J. Feibelman, "Surface self-diffusion on pt(001) by an atomic exchange mechanism," *Phys. Rev. Lett.*, vol. 64, pp. 3143–3146, 26 1990.

[220] M. C. Tringides, *Surface diffusion: Atomistic and collective processes*. Springer, Boston, MA, 1997.

[221] I. M. Ciobîcă, F. Frechard, R. A. van Santen, A. W. Kleyn, and J. Hafner, "A dft study of transition states for ch activation on the ru(0001) surface," *The Journal of Physical Chemistry B*, vol. 104, no. 14, pp. 3364–3369, 2000. eprint: https://doi.org/10.1021/jp9933141.

[222] L. Kristinsdóttir and E. Skúlason, "A systematic dft study of hydrogen diffusion on transition metal surfaces," *Surface Science*, vol. 606, no. 17, pp. 1400 –1404, 2012.

[223] G. Antczak and G. Ehrlich, "Jump processes in surface diffusion," *Surface Science Reports*, vol. 62, no. 2, pp. 39 –61, 2007.

[224] S. Valkealahti and M. Manninen, "Diffusion on aluminum-cluster surfaces and the cluster growth," *Phys. Rev. B*, vol. 57, pp. 15 533–15 540, 24 1998.

[225] P. Gravil and S. Holloway, "Exchange mechanisms for self-diffusion on aluminium surfaces," *Surface Science*, vol. 310, no. 1, pp. 267 –272, 1994.

[226] C. Liu, J. Cohen, J. Adams, and A. Voter, "Eam study of surface self-diffusion of single adatoms of fcc metals ni, cu, al, ag, au, pd, and pt," *Surface Science*, vol. 253, no. 1, pp. 334 –344, 1991.

[227] R. Stumpf and M. Scheffler, "Ab initio calculations of energies and self-diffusion on flat and stepped surfaces of al and their implications on crystal growth," *Phys. Rev. B*, vol. 53, pp. 4958–4973, 8 1996.

[228] G. Kellogg, "Field ion microscope studies of single-atom surface diffusion and cluster nucleation on metal surfaces," *Surf. Sci. Rep.*, vol. 21, no. 1, pp. 1 –88, 1994.

[229] B. D. Yu and M. Scheffler, "Physical origin of exchange diffusion on fcc(100) metal surfaces," *Phys. Rev. B*, vol. 56, R15569–R15572, 24 1997.

[230] P Feibelman, "Diffusion path for an al adatom on al(001)," *Phys. Rev. Lett.*, vol. 65, pp. 729–732, 6 1990.

[231] C. M. Chang and C. M. Wei, "Self-diffusion of adatoms and dimers on fcc (100) surfaces," *Chin. J. Phys.*, vol. 43, no. 1S, pp. 169–175, 2005.

[232] P Gravil and S Holloway, "Exchange mechanisms for self-diffusion on aluminum surfaces," *Surf. Sci.*, vol. 310, pp. 267–272, 1993.

[233] R Stumpf and M Scheffler, "Ab initio calculations of energies and self-diffusion on flat and stepped surfaces of al and their implications on crystal growth," *Phys. Rev. B*, vol. 53, pp. 4958–4973, 8 1996.

[234] G. Henkelman and H. Jònsson, "Multiple time scale simulations of metal crystal growth reveal the importance of multiatom surface processes," *Phys. Rev. Lett.*, vol. 90, pp. 259–263, 11 2003.

[235] O. Trushin, P. Salo, M. Alatalo, and T Ala-Nissila, "Atomic mechanisms of cluster diffusion on metal fcc(100) surfaces," *Surface Science*, vol. 482-485, pp. 365 –369, 2001.

[236] R. Stumpf and M. Scheffler, "Ab initio calculations of energies and self-diffusion on flat and stepped surfaces of al and their implications on crystal growth," *Phys. Rev. B*, vol. 53, pp. 4958–4973, 8 1996.

[237] C. Chang, C. Wei, and S. Chen, "Structural and dynamical behavior of al trimer on al(111) surface," *Surface Science*, vol. 465, no. 1, pp. 65 –75, 2000.

[238] C. M. Chang, C. M. Wei, and S. P. Chen, "Self-diffusion of small clusters on fcc metal (111) surfaces," *Phys. Rev. Lett.*, vol. 85, pp. 1044–1047, 5 2000.

[239] "Dimer binding energies on fcc(111) metal surfaces," *Surface Science*, vol. 539, no. 1, pp. L560 –L566, 2003.

[240] C. Busse, C. Engin, H. Hansen, U. Linke, T. Michely, and H. M. Urbassek, "Adatom formation and atomic layer growth on al(111) by ion bombardment: Experiments and molecular dynamics simulations," *Surface Science*, vol. 488, no. 3, pp. 346 – 366, 2001.

[241] F. Buatier de Mongeot, W. Zhu, A. Molle, R. Buzio, C. Boragno, U. Valbusa, E. G. Wang, and Z. Zhang, "Nanocrystal formation and faceting instability in al(110) homoepitaxy: True upward adatom diffusion at step edges and island corners," *Phys. Rev. Lett.*, vol. 91, p. 016 102, 1 2003.

[242] A. Sepúlveda-Escribano, F. Coloma, and F. Rodrıguez-Reinoso, "Platinum catalysts supported on carbon blacks with different surface chemical properties," *Applied Catalysis A: General*, vol. 173, no. 2, pp. 247 –257, 1998.

[243] A. Chen and P. Holt-Hindle, "Platinum-based nanostructured materials: Synthesis, properties, and applications," *Chemical Reviews*, vol. 110, no. 6, pp. 3767–3804, 2010, PMID: 20170127. eprint: https://doi.org/10.1021/cr9003902.

[244] S. Zhang, X.-Z. Yuan, J. N. C. Hin, H. Wang, K. A. Friedrich, and M. Schulze, "A review of platinum-based catalyst layer degradation in proton exchange membrane fuel cells," *Journal of Power Sources*, vol. 194, no. 2, pp. 588 –600, 2009.

[245] H. Yang, "Platinum-based electrocatalysts with core–shell nanostructures," *Angewandte Chemie International Edition*, vol. 50, no. 12, pp. 2674–2676, 2011. eprint: https://onlinelibrary.wiley.com/doi/pdf/10.1002/anie.201005868.

[246] A. Baiker, "Progress in asymmetric heterogeneous catalysis: Design of novel chirally modified platinum metal catalysts1communication presented at the first francqui colloquium, brussels, 19–20 february 1996.1," *Journal of Molecular Catalysis A: Chemical*, vol. 115, no. 3, pp. 473 –493, 1997.

[247] N. Tian, Z.-Y. Zhou, and S.-G. Sun, "Platinum metal catalysts of high-index surfaces: From single-crystal planes to electrochemically shape-controlled nanoparticles," *The Journal of Physical Chemistry C*, vol. 112, no. 50, pp. 19 801–19 817, 2008. eprint: https://doi.org/10.1021/jp804051e.

[248] T. Mallat and A. Baiker, "Oxidation of alcohols with molecular oxygen on platinum metal catalysts in aqueous solutions," *Catalysis Today*, vol. 19, no. 2, pp. 247 –283, 1994.

[249] C. J. O'Brien, C. M. Barr, P. M. Price, K. Hattar, and S. M. Foiles, "Grain boundary phase transformations in ptau and relevance to thermal stabilization of bulk nanocrystalline metals," *Jour. of Mat. Sci.*, vol. 53, pp. 2911–2927, 2018.

[250] X. W. Zhou, R. A. Johnson, and H. N. G. Wadley, "Misfit-energy-increasing dislocations in vapor-deposited cofeõnife multilayers," *Phys. Rev. B*, vol. 60, p. 144 113, 2004.

[251] S. M. Foiles, M. I. Baskes, and M. S Daw, "Embedded-atom-method functions for the fcc metals cu, ag, au, ni, pd, pt, and their alloys," *Phys. Rev. B*, vol. 59, p. 11 693, 1999.

[252] G. Grochola, S. P. Russo, and I. K. Snook, "On fitting a gold embedded atom method potential using the force matching method," *The Journal of Chemical Physics*, vol. 123, no. 20, p. 204 719, 2005. eprint: https://doi.org/10.1063/1.2124667.

[253] S. M. Rassoulinejad-Mousavi and Y. Zhang, "Interatomic potentials transferability for molecular simulations: A comparative study for platinum, gold and silver," *Scientific Reports*, vol. 8, p. 2424, 2018.

[254] G. Ho, M. T. Ong, K. J. Caspersen, and E. A. Carter, "Energetics and kinetics of vacancy diffusion and aggregation in shocked aluminium via orbital-free density functional theory," *Phys. Chem. Chem. Phys.*, vol. 9, pp. 4951–4966, 36 2007.

[255] A. Kuksin, G. Norman, V. Stegailov, A. Yanilkin, and P. Zhilyaev, "Dynamic fracture kinetics, influence of temperature and microstructure in the atomistic model of aluminum," *International Journal of Fracture*, vol. 162, no. 1, pp. 127–136, 2010.

[256] L. V. Zhigilei, Z. Lin, and D. S. Ivanov, "Atomistic modeling of short pulse laser ablation of metals: Connections between melting, spallation, and phase explosion," *The Journal of Physical Chemistry C*, vol. 113, no. 27, pp. 11 892–11 906, 2009. eprint: https://doi.org/10.1021/jp902294m.

[257] A. H. Larsen, J. J. Mortensen, J. Blomqvist, I. E. Castelli, R. Christensen, M. Dułak, J. Friis, M. N. Groves, B. Hammer, C. Hargus, E. D. Hermes, P. C. Jennings, P. B. Jensen, J. Kermode, J. R. Kitchin, E. L. Kolsbjerg, J. Kubal, K. Kaasbjerg, S. Lysgaard, J. B. Maronsson, T. Maxson, T. Olsen, L. Pastewka, A. Peterson, C. Rostgaard, J. Schiøtz, O. Schütt, M. Strange, K. S. Thygesen, T. Vegge, L. Vilhelmsen, M. Walter, Z. Zeng, and K. W. Jacobsen, "The atomic simulation environment—a python library for working with atoms," *Journal of Physics: Condensed Matter*, vol. 29, no. 27, p. 273 002, 2017.

[258] J. Byggmästar, A. Hamedani, K. Nordlund, and F. Djurabekova, "Machine-learning interatomic potential for radiation damage and defects in tungsten," *Phys. Rev. B*, vol. 100, p. 144 105, 14 2019.

[259] T. Sun, K. Umemoto, Z. Wu, J.-C. Zheng, and R. M. Wentzcovitch, "Lattice dynamics and thermal equation of state of platinum," *Phys. Rev. B*, vol. 78, p. 024 304, 2 2008.

[260] D. H. Chung and W. R. Buessem, "The voigt reuss hill approximation and elastic moduli of polycrystalline mgo, caf2, -zns, znse, and cdte," *Journal of Applied Physics*, vol. 38, no. 6, pp. 2535–2540, 1967. eprint: https://doi.org/10.1063/1.1709944.

[261] P. Hirel, "Atomsk: A tool for manipulating and converting atomic data files," *Computer Physics Communications*, vol. 197, pp. 212 –219, 2015.

[262] A. Tschöpe and R. Birringer, "Thermodynamics of nanocrystalline platinum," *Acta Metallurgica et Materialia*, vol. 41, no. 9, pp. 2791 –2796, 1993.

[263] J. Li, B. Lu, H. Zhou, C. Tian, Y. Xian, G. Hu, and R. Xia, "Molecular dynamics simulation of mechanical properties of nanocrystalline platinum: Grain-size and temperature effects," *Physics Letters A*, vol. 383, no. 16, pp. 1922 –1928, 2019.

[264] Y. Shibuta, K. Oguchi, T. Takaki, and M. Ohno, "Homogeneous nucleation and microstructure evolution in million-atom molecular dynamics simulation," *Scientific Reports*, vol. 5, no. 1, p. 13 534, 2015.

[265] F. Birch, "Elasticity and constitution of the earth's interior," *Journal of Geophysical Research (1896-1977)*, vol. 57, no. 2, pp. 227–286, 1952. eprint: https://agupubs.onlinelibrary.wiley.com/doi/pdf/10.1029/JZ057i002p00227.

[266] W.-J. Ding, J.-X. Yi, P. Chen, D.-L. Li, L.-M. Peng, and B.-Y. Tang, "Elastic properties and electronic structures of typical al–ce structures from first-principles calculations," *Solid State Sciences*, vol. 14, no. 5, pp. 555 –561, 2012.

[267] D. Alfe, *Comp. Phys. Comm.*, vol. 180, p. 2622, 2009.

[268] D. Schumacher, A. Seeger, and O. Harlen, "Vacancies, divacancies, and self-diffusion in platinum," *Phys. Stat. Sol.*, vol. 25, p. 359, 1968.

[269] G. L. Bacchella, E. Germagnoli, and S. Granata, "On the kinetics of quenched-in lattice vacancies in platinum," *J. App. Phys.*, vol. 30, 1959.

[270] W. Hertz and H. Peisl, "Volume and electrical resistivity change due to vacancies in platinum," *J. Phys. F: Metal Phys.*, vol. 5, p. 604, 1975.

[271] X. Zhang and G. Lu, "Electronic origin of void formation in fcc metals," *Phys. Rev. B*, vol. 77, p. 174 102, 2008.

[272] P. A. Korzhavyi, I. A. Abrikosov, and B. Johansson, "First-principles calculations of the vacancy formation energy in transition and noble metals," *Phys. Rev. B*, vol. 59, p. 11 693, 1999.

[273] V. K. La Mer, *Jour. Chem. Phys.*, vol. 1, p. 289, 1933.

[274] S. W. Benson, "Thermochemical kinetics: Methods for the estimation of thermochemical data and rate parameters, 2nd ed.," *Wiley, New York*, 1976.

[275] S. Collard and R. McLellan, "High-temperature elastic constants of platinum single crystals," *Acta Metallurgica et Materialia*, vol. 40, no. 4, pp. 699 –702, 1992.

[276] J. B. Adams, S. M. Foiles, and W. G. Wolfer, "Self-diffusion and impurity diffusion of fee metals using the five-frequency model and the embedded atom method," *Journal of Materials Research*, vol. 4, no. 1, 102–112, 1989.

[277] J. J. Mortensen, K. Kaasbjerg, S. L. Frederiksen, J. K. Nørskov, J. P. Sethna, and K. W. Jacobsen, "Bayesian error estimation in density-functional theory," *Phys. Rev. Lett.*, vol. 95, p. 216 401, 21 2005.

[278] A Stroppa and G Kresse, "The shortcomings of semi-local and hybrid functionals: What we can learn from surface science studies," *New Journal of Physics*, vol. 10, no. 6, p. 063 020, 2008.

[279] J. E. Angelo and M. I. Baskes, "Interfacial studies using the eam and meam," *Interface Science*, vol. 4, no. 1, pp. 47–63, 1997.

[280] BASKES, M. I., FOILES, S. M., and DAW, M. S., "Application of the embedded atom method to the fracture of interfaces," *J. Phys. Colloques*, vol. 49, pp. C5–483–C5–495, 1988.

[281] J. Tallon and A. Wolfenden, "Temperature dependence of the elastic constants of aluminum," *Journal of Physics and Chemistry of Solids*, vol. 40, no. 11, pp. 831 –837, 1979.

[282] S. Zhang, H. Li, S. Zhou, and T. Pan, "Estimation thermal expansion coefficient from lattice energy for inorganic crystals," *Japanese Journal of Applied Physics*, vol. 45, no. 11, pp. 8801–8804, 2006.

[283] A. Hunter, R. F. Zhang, and I. J. Beyerlein, "The core structure of dislocations and their relationship to the material -surface," *Journal of Applied Physics*, vol. 115, no. 13, p. 134 314, 2014. eprint: `https://doi.org/10.1063/1.4870462`.

[284] F. Zerilli and R. Armstrong, "The effect of dislocation drag on the stress-strain behavior of f.c.c. metals," *Acta Metallurgica et Materialia*, vol. 40, no. 8, pp. 1803 –1808, 1992.

[285] S. Mendelson, "Dislocation dissociations in hcp metals," *Journal of Applied Physics*, vol. 41, no. 5, pp. 1893–1910, 1970. eprint: https://doi.org/10.1063/1.1659139.

[286] H. V. Swygenhoven] and J. R. Weertman, "Deformation in nanocrystalline metals," *Materials Today*, vol. 9, no. 5, pp. 24 –31, 2006.

[287] Z. Jin, S. Dunham, H. Gleiter, H. Hahn, and P. Gumbsch, "A universal scaling of planar fault energy barriers in face-centered cubic metals," *Scripta Materialia*, vol. 64, no. 7, pp. 605 –608, 2011.

[288] A. Stukowski and K. Albe, "Extracting dislocations and non-dislocation crystal defects from atomistic simulation data," *Modelling and Simulation in Materials Science and Engineering*, vol. 18, no. 8, p. 085 001, 2010.

[289] G. Boisvert, L. J. Lewis, and M. Scheffler, "Island morphology and adatom self-diffusion on pt(111)," *Phys. Rev. B*, vol. 57, pp. 1881–1889, 3 1998.

[290] N. E. Singh-Miller and N. Marzari, "Surface energies, work functions, and surface relaxations of low-index metallic surfaces from first principles," *Physical Review B*, vol. 80, no. 23, 2009.

[291] N. Panagiotides and N. I. Papanicolaou, "Diffusion of platinum adatoms and dimers on pt(111) surface by molecular-dynamics simulation," *International Journal of Quantum Chemistry*, vol. 110, no. 1, pp. 202–209, 2010. eprint: https://onlinelibrary.wiley.com/doi/pdf/10.1002/qua.22045.

[292] M. Villarba and H. Jónsson, "Diffusion mechanisms relevant to metal crystal growth: Pt/pt(111)," *Surface Science*, vol. 317, no. 1, pp. 15 –36, 1994.

[293] D. Bassett and P. Webber, "Diffusion of single adatoms of platinum, iridium and gold on platinum surfaces," *Surface Science*, vol. 70, no. 1, pp. 520 –531, 1978.

[294] I. Matrane, M. Mazroui, and K. Sbiaai, "Diffusion and adsorption of dimers on reconstructed pt(110) surfaces: First principle and eam studies," *Chemical Physics*, vol. 502, pp. 96 –101, 2018.

[295] G. S. Rohrer, "Grain boundary energy anisotropy: A review," *Journal of Materials Science*, vol. 46, no. 18, pp. 5881–5895, 2011.

[296] A. D. Rollett, G. Gottstein, L. S. Shvindlerman, and D. A. Molodov, "Grain boundary mobility – a brief review," *Zeitschrift für Metallkunde*, vol. 95, no. 4, pp. 226–229, 2004.

[297] R. Gifkins, "Grain-boundary participation in high-temperature deformation: An historical review," *Materials Characterization*, vol. 32, no. 2, pp. 59 –77, 1994.

[298] L. Zhang, C. Lu, and K. Tieu, "A review on atomistic simulation of grain boundary behaviors in face-centered cubic metals," *Computational Materials Science*, vol. 118, pp. 180 –191, 2016.

[299] R. Balluffi, Y. Komem, and T. Schober, "Electron microscope studies of grain boundary dislocation behavior," *Surface Science*, vol. 31, pp. 68 –103, 1972.

[300] G. Reiss, J. Vancea, and H. Hoffmann, "Grain-boundary resistance in polycrystalline metals," *Phys. Rev. Lett.*, vol. 56, pp. 2100–2103, 19 1986.

[301] H. Zheng, X.-G. Li, R. Tran, C. Chen, M. Horton, D. Winston, K. A. Persson, and S. P. Ong, "Grain boundary properties of elemental metals," *Acta Materialia*, vol. 186, pp. 40 –49, 2020.

[302] J. Cheng, J. Luo, and K. Yang, "Aimsgb: An algorithm and open-source python library to generate periodic grain boundary structures," *Computational Materials Science*, vol. 155, pp. 92 –103, 2018.

[303] M. R. Sørensen, Y. Mishin, and A. F. Voter, "Diffusion mechanisms in cu grain boundaries," *Phys. Rev. B*, vol. 62, pp. 3658–3673, 6 2000.

[304] M. Tschopp, M. Horstemeyer, F. Gao, X. Sun, and M. Khaleel, "Energetic driving force for preferential binding of self-interstitial atoms to fe grain boundaries over vacancies," *Scripta Materialia*, vol. 64, no. 9, pp. 908 –911, 2011.

[305] M. Upmanyu, D. J. Srolovitz, L. S. Shvindlerman, and G. Gottstein, "Vacancy generation during grain boundary migration," *Interface Science*, vol. 6, no. 4, pp. 289–300, 1998.

[306] R. Rousseau and D. Marx, "Exploring the electronic structure of elemental lithium: From small molecules to nanoclusters, bulk metal, and surfaces," *Chemistry – A European Journal*, vol. 6, no. 16, pp. 2982–2993, 2000. eprint: `https://chemistry-europe.onlinelibrary.wiley.com/doi/pdf/10.1002/1521-3765%2820000818%296%3A16%3C2982%3A%3AAID-CHEM2982%3E3.0.CO%3B2-S`.

[307] I. Tamblyn, J.-Y. Raty, and S. A. Bonev, "Tetrahedral clustering in molten lithium under pressure," *Phys. Rev. Lett.*, vol. 101, p. 075 703, 7 2008.

[308] S. F. Elatresh, W. Cai, N. W. Ashcroft, R. Hoffmann, S. Deemyad, and S. A. Bonev, "Evidence from fermi surface analysis for the low-temperature structure of lithium," *Proceedings of the National Academy of Sciences*, vol. 114, no. 21, pp. 5389–5394, 2017. eprint: `https://www.pnas.org/content/114/21/5389.full.pdf`.

[309] F. A. Gorelli, S. F. Elatresh, C. L. Guillaume, M. Marqués, G. J. Ackland, M. Santoro, S. A. Bonev, and E. Gregoryanz, "Lattice dynamics of dense lithium," *Phys. Rev. Lett.*, vol. 108, p. 055 501, 5 2012.

[310] I. Tamblyn, J.-Y. Raty, and S. A. Bonev, "Clustering in dense molten lithium," in *APS March Meeting Abstracts*, ser. APS Meeting Abstracts, Mar. 2008, B13.005.

[311] M. Hanfland, K. Syassen, N. E. Christensen, and D. L. Novikov, "New high-pressure phases of lithium," *Nature*, vol. 408, no. 6809, pp. 174–178, 2000.

[312] C. L. Guillaume, E. Gregoryanz, O. Degtyareva, M. I. McMahon, M. Hanfland, S. Evans, M. Guthrie, S. V. Sinogeikin, and H.-K. Mao, "Cold melting and solid structures of dense lithium," *Nature Physics*, vol. 7, no. 3, pp. 211–214, 2011.

[313] A. M. Schaeffer, S. R. Temple, J. K. Bishop, and S. Deemyad, "High-pressure superconducting phase diagram of 6li: Isotope effects in dense lithium," *Proceedings of the National Academy of Sciences*, vol. 112, no. 1, pp. 60–64, 2015. eprint: `https://www.pnas.org/content/112/1/60.full.pdf`.

[314] D. K. Belashchenko and O. I. Ostrovskii, "Application of the embedded atom model to liquid metals: Liquid lithium," *High Temperature*, vol. 47, no. 2, pp. 211–218, 2009.

[315] R. M. Khusnutdinoff, B. N. Galimzyanov, and A. V. Mokshin, "Dynamics of liquid lithium atoms. pseudopotential and eam-type potentials," *Journal of Experimental and Theoretical Physics*, vol. 126, no. 1, pp. 83–89, 2018.

[316] J. Lv, Y. Wang, L. Zhu, and Y. Ma, "Predicted novel high-pressure phases of lithium," *Phys. Rev. Lett.*, vol. 106, p. 015 503, 1 2011.

[317] C. J. Pickard and R. J. Needs, "Dense low-coordination phases of lithium," *Phys. Rev. Lett.*, vol. 102, p. 146 401, 14 2009.

[318] J. Palmer, A. Llobet, S.-H. Yeon, J. Fischer, Y. Shi, Y. Gogotsi, and K. Gubbins, "Modeling the structural evolution of carbide-derived carbons using quenched molecular dynamics," *Carbon*, vol. 48, no. 4, pp. 1116 –1123, 2010.

[319] J. Sarnthein, A. Pasquarello, and R. Car, "Model of vitreous sio2 generated by an ab initio molecular-dynamics quench from the melt," *Phys. Rev. B*, vol. 52, pp. 12 690–12 695, 17 1995.

[320] M. Brack, "The physics of simple metal clusters: Self-consistent jellium model and semiclassical approaches," *Rev. Mod. Phys.*, vol. 65, pp. 677–732, 3 1993.

[321] M. S. Daw and M. I. Baskes, "Semiempirical, quantum mechanical calculation of hydrogen embrittlement in metals," *Phys. Rev. Lett.*, vol. 50, pp. 1285–1288, 17 1983.